Ethyl Cellulose Nanoparticles in Multiphase Systems: Foams, Emulsions, and Porous Media

by

Navid Bizmark

A thesis
presented to the University of Waterloo
in fulfillment of the
thesis requirement for the degree of
Doctor of Philosophy
in
Chemical Engineering (Water)

Waterloo, Ontario, Canada, 2017

Examining Committee Membership

The following served on the Examining Committee for this thesis. The decision of the Examining Committee is by majority vote.

External Examiner:
> Prof. Kishore Mohanty
> Petroleum and Geosystems Engineering, The University of Texas at Austin

Supervisor:
> Prof. Marios Ioannidis
> Chemical Engineering, University of Waterloo

Internal Members:
> Prof. Nasser Mohieddin Abukhdeir
> Chemical Engineering, University of Waterloo
> Prof. Boxin Zhao
> Chemical Engineering, University of Waterloo

Internal-external Member:
> Prof. Carolyn Ren
> Mechanical and Mechatronics Engineering, University of Waterloo

I hereby declare that I am the sole author of this thesis. This is a true copy of the thesis, including any required final revisions, as accepted by my examiners.

I understand that my thesis may be made electronically available to the public.

Abstract

Adsorption-mediated self-assembly of ethyl cellulose (EC) nanoparticles at fluid inter-faces, driven by reduction in interfacial energy, is shown to lead to stabilization of emulsions and foams. A multiscale approach is followed to address a number of fundamental and practical questions for application of EC nanoparticles in multiphase flows through porous media. At the nanoscale, the effects of pair interactions between EC nanoparticles sus-pended in water, between an EC nanoparticle and a fluid interface (oil-water or air-water), and between EC nanoparticles adsorbed at a fluid interface are studied by extended-DLVO computations and dynamic surface (interfacial) tension measurements with emphasis on

- the dependence of colloidal suspension stability on ionic strength

- the kinetics of nanoparticle adsorption at the air-water and alkane-water interfaces

- the nature and extent of coverage of fluid interfaces by nanoparticles

In the absence of salt, EC nanoparticle suspensions are stable at neutral pH as a result of electrostatic repulsion, but colloidal stability is lost by the addition of salt at or beyond a concentration of 0.05 M (the critical coagulation concentration or CCC). Regardless of ionic strength, however, hydrophobic attraction dominates the interactions between EC nanoparticles and fluid interfaces, resulting in barrier-less irreversible adsorption at both the air-water and alkane-water interfaces. Ionic strength is also found to have insignificant effect on the coverage of either kind of interface at steady-state, which approaches the jamming limit of 91% corresponding to a tight hexagonal packing for any value of the ionic strength in the range of 0 M to 0.1 M. Nonetheless, subtle effects of the ionic strength are observed on the rate of approach to steady state, during the later stages of adsorption, which is accelerated by the addition of salt in the case of the alkane-water interface, but apparently unaffected in the case of the air-water interface. Above the CCC, alkane-water and air-water interfaces behave similarly, in that the approach to steady state is decelerated as a result of increased surface blocking and competition for adsorbing species between coagulation in the bulk and attachment at the interface. These findings lead to new insights into the way in which EC nanoparticles stabilize emulsions and foams.

The extent to which EC nanoparticles may be used to stabilize so-called Pickering emul-sions is investigated as a function of phase volume ratio, ionic strength and nanoparticle concentration. Both oil-in-water (O/W) and water-in-oil (W/O) Pickering emulsions are observed, their stability is quantified and explained theoretically. The most stable O/W Pickering emulsion is obtained at an ionic strength slightly below the CCC with at least

70% volume fraction for the internal phase, an observation which opens the path for the utilization of EC nanoparticles as stabilizers of high internal phase Pickering emulsions (HIPPE). Such a HIPPE is shown to act as a template to fabricate a polymeric porous material made of EC. This material is demonstrated to selectively adsorb oil from the surface of water, suggesting potential applications in the field of oil-water separations.

In line with theoretical expectation, flow and transport tests in transparent glass micromodels demonstrate that EC nanoparticles in stable colloidal suspensions (i.e. below CCC) move through silica-based porous media as a conservative tracer (e.g. NaCl). The convection-dispersion equation adequately describes this process with transport parameter (dispersivity and dispersion coefficient) values which agree with established models. Above the CCC convection accelerates the coagulation of EC nanoparticles, resulting in very rapid clogging of the porous medium and effective filtration of the nanoparticles. Lastly, it is demonstrated that foam can be generated *in situ* during the co-injection of gas and EC nanoparticle suspensions in glass micromodels, suggesting the possibility to engineer new foam flooding technologies for the recovery of hydrocarbons from subsurface porous media.

Acknowledgements

Dedication

To my parents who have devoted their life to me
and
for their unstoppable love and support

&

To my sister, Nastaran, for her love and encouragement

Table of Contents

List of Tables

List of Figures

xviii

Nomenclature

Symbols

a	empirical constant in Eq. 2.4
A_{po}	surface area of particle exposed to oil
A_{pw}	surface area of particle exposed to water
b	empirical constant in Eq. 2.4
B_0	blocking function
C	molar concentration
C_0	initial molar concentration
Ca	capillary number
D	bulk diffusion coefficient of particles
d	particle diameter
D_{32}	mean volume-surface diameter
D_{AB}	bulk diffusion coefficient of particle A in the medium B
D_{cri}	critical distance between two fluid interfaces
D_h	dispersion coefficient
ΔE	adsorption energy
E_I	energy of the interface at state I
E_{II}	energy of the interface at state II
E_{aw}	energy of air-water interface
E_{pa}	energy of particle-air surface
E_{pw}	energy of particle-water surface
f	volume fraction
$g(\tau)$	autocorrelation function
h	separation distance (surface-to-surface)
H	mean curvature
H_2	contact line undulation
H_{121}	Hamaker constant for interacting EC nanoparticles (1) in water (2)

H_{132}	Hamaker constant for interacting EC nanoparticle (1) with oil (3) across water (2)
$I(t)$	light intensity fluctuations
j	adsorption flux
K_{132}	hydrophobic interaction energy constant between solid (1) and solid (2) in the medium (3)
k_a	adsorption constant
$\overline{k}_a$	dimensionless adsorption constant, $k_a/\pi r^2 N_A C_0 D$
k_B	Boltzmann constant (1.38×10^{-23} m^2 kg s^{-2} K^{-1})
k_{coag}	coagulation rate constant
k_{coag}^{fav}	coagulation rate constant under favorable conditions for coagulation (i.e., >CCC)
k_i	constant of adsorption at fluid interface
K_l	dimensionless parameter in Eqs. 2.17 and 2.19
k_s	constant of adsorption on solid matrix
L	length of porous medium
n	index
N_A	Avogadro's number (6.022×10^{23} mol^{-1})
N_b	number concentration of particles in the bulk
$N_{b,eff}$	number concentration of particles in the effluent
N_{b0}	initial number concentration of particles in the bulk
$\overline{N_b}$	dimensionless particle concentration, N_b/N_{b0}
N_i	number concentration of particles adsorbed at the fluid interface
n_p	number of pores
N_s	number concentration of particles adsorbed at the solid matrix surface
n_t	number of throats
P_c	capillary pressure
P_c^{dra}	drainage capillary pressure
P_c^{imb}	imbibition capillary pressure
P_{nw}	pressure of nonwetting phase
P_w	pressure of wetting phase
Q	volumetric flowrate
r	particle radius
R	curvature radius
r_c	average radius of contact line
R_i	rate of particles captured by the fluid interface
R_s	rate of particles captured by the solid matrix
S_{nw}	saturation of nonwetting phase
S_w	saturation of wetting phase
T	temperature
t	time

$\bar{t}$	dimensionless time, $D_h t / L^2$
U	superficial velocity
u_A / F_A	mobility of particle A
V	volume
v_p	pore velocity
V_p	volume of pore
V_t	volume of throat
W	colloidal stability ratio
w	width
w_p	width of pore
w_t	width of throat
x	distance
$\overline{x}$	dimensionless distance, x/L

Greek symbols

α_{ad}	probability of successful attachment to a collector
α_L	longitudinal dispersivity
γ	surface/interfacial tension
γ_0	surface/interfacial tension of the pristine interface
γ_∞	surface/interfacial tension at steady state
δ	depth of etching
δ_p	depth of etching for pore
δ_t	depth of etching for throats
ε_0	vacuum permittivity (8.85×10^{-12} F m^{-1})
ε_o	relative dielectric constant of oil (or air)
ε_r	relative dielectric constant of the solvent
ε_w	relative dielectric constant of water
η_0	single collector efficiency
θ	contact angle
Θ	surface/interface coverage
Θ_∞	surface/interface coverage at steady state
κ^{-1}	debye length
λ	wavelength
μ	dipole moment
μ_B	fluid viscosity
ψ	dimensionless parameter
ρ	mass concentration

ρ_0	initial mass concentration
ρ_p	particle density
σ_d	surface dipole moment density
σ_{po}	charge density on the particle surface exposed to oil
σ_{pw}	charge density on the particle surface exposed to water
τ	delay time
ϕ	detection angle
ϕ_b	adsorption barrier
φ	subtended angle between the diagonals of the respective quadrupoles and the line connecting the centers of the two particles adsorbed at interface
Φ^{p-p}	net particle-particle interaction energy
Φ_{d-d}^{O}	dipole-dipole interaction energy through oil (or air) between two particles adsorbed at a fluid interface
Φ_{d-d}^{W}	dipole-dipole interaction energy through water between two particles adsorbed at a fluid interface
Φ_{elec}^{O}	electrostatic interaction energy through oil (or air) between two particles adsorbed at a fluid interface
Φ_{elec}^{p-i}	electrostatic interaction energy between a fluid interface and a particle
Φ_{elec}^{p-p}	van der Waals interaction energy between two particles in the bulk
Φ_{elec}^{W}	electrostatic interaction energy through water between two particles adsorbed at a fluid interface
Φ_{H}^{p-p}	hydrophobic interaction energy between two particles in the bulk
Φ_{H}^{W}	hydrophobic interaction energy through water between two particles adsorbed at a fluid interface
Φ_{Qcap}	surface energy associated with the meniscus distortion
$\Delta\Phi_{Qcap}$	quadrupolar capillary attraction
Φ_{total}	the net interaction energy among adsorbed particles at the interface
Φ_{vdW}^{O}	van der Waals interaction energy through oil (or air) between two particles adsorbed at a fluid interface
Φ_{vdW}^{p-i}	van der Waals interaction energy between a fluid interface and a particle
Φ_{vdW}^{W}	van der Waals interaction energy through water between two particles adsorbed at a fluid interface
Φ_{vdW}^{p-p}	electrostatic interaction energy between two particles in the bulk
ξ	dimensionless parameter
Ψ_0	surface potential
Ψ_d	potential at the stern layer
Ψ_i	potential charge of the interface
Ψ_p	particle surface charge
Ψ_{pw}	particle surface charge exposed to water

ω	dimensionless parameter
Ω	dimensionless parameter
ζ-potential	zeta potential
Π	disjoining pressure

Abbrevatiations

1D	One Dimensional
2D	Two Dimensional
3D	Three Dimensional
ADSA	Axisymmetric Drop Shape Analysis
BC	Breakthrough Curve
CCC	Critical Coagulation Concentration
CCD	Charge Coupled Device
CDE	Convection-Dispersion Equation
DI	Deionized
DLA	Diffusion-Limited Aggregation
DLS	Dynamic Light Scattering
DLVO	Derjaguin, Landau, Verwey, and Overbeek
DST	Dynamic Surface Tension
EC	Ethyl Cellulose
EOR	Enhanced Oil Recovery
HIPE	High Internal Phase Emulsion
HIPPE	High Internal Phase Pickering Emulsion
HPLC	High-Performance Liquid Chromatography
IFT	Interfacial Tension
IPA	Isopropyl Alcohol
iso-C8	iso-octane
LED	Light-Emitting Diode
LRC	Inductance (L), Resistance (R), Capacitance (C)
LSD	Least Significant Difference
NAPL	non-Aqueous Phase Liquid
n-C10	n-decane
n-C12	n-dodecane
n-C16	n-hexadecane
O/W	Oil-in-Water
O/W/O	Oil-in-Water-in-Oil
OOIP	Original Oil-in-Place

Pe	Peclet Number
PSD	Pore Size Distribution
PV	Pore Volume
Re	Reynolds Number
RHS	Right-Hand Side
RLA	Reaction-Limited Aggregation
RSA	Random Sequential Adsorption
SEM	Scanning Electron Microscope
TEM	Transmission Electron Microscope
TGA	Thermogravimetry Analysis
W/O	Water-in-Oil
W/O/W	Water-in-Oil-in-Water

Chapter 1

Introduction

1.1 General overview

The role of foams and emulsions in everyday life is certainly significant: foodstuffs (e.g., dairy products, dressing sauces, whipped cream), pharmaceuticals and cosmetics (e.g., creams, shampoo, shaving foam), and paints are a few from a plethora of examples [24]. It is common knowledge that foam or emulsion cannot be generated without a surface active agent that adsorbs at the fluid interface (gas-liquid or liquid-liquid interfaces) and reduces the surface (interfacial) tension. While surfactants are typical foam and emulsion stabilizers, solid particles are a different class of surface active agents with the potential to stabilize emulsions and foams. The first evidence that small (submillimeter size) solid particles can adsorb at an interface (oil-water) and stabilize emulsions was found a century ago by Ramsden [141] and Pickering [135]. Since then, solid particle-stabilized emulsions are called "Pickering emulsions" − named after S. U. Pickering [135]. Pickering emulsions (or foams) can be easily distinguished from the ones stabilized by surfactants by their remarkable stability.

In recent years, nano-sized particles (nanoparticles) have also been successfully used to stabilize foams and emulsions, opening the door to improvements in many high-tech applications including, but not limited to, oil recovery [127, 155, 195], waterbody cleanup [41], groundwater remediation [134, 157], and fabrication of advanced functional materials [59, 124]. Most of these applications are complicated by the physics of transport of two or more immiscible fluids through porous media. Contrary to single-phase fluid flow in a porous medium which can be reliably described by Darcy's law [184], understanding of multiphase flow in porous media remains a challenge [65]. Movement of multiple fluid

phases in porous media is inextricably linked to the displacement of fluid-fluid interfaces under the combined action of viscous, capillary, and gravity forces. Direct dependence of the latter on surface (interfacial) tension and wettability implies that solutes (surfactants) and suspended nanoparticles with the ability to adsorb at surfaces and interfaces can have non-trivial effects on multiphase flow. While much research has been devoted to surfactants, the effects of nanoparticles on multiphase flow in porous media have only recently begun to receive attention. It becomes immediately obvious that the way nanoparticles affect (and are affected by) multiphase flow in porous media requires laboratory studies across a broad spectrum of length scales (see Figure 1.1) prior to field-scale deployment. Examples of such studies are given below:

single particle scale   **single interface scale**   **multiple interface scale**

~nm   µm-mm   cm-m

multiscale approach

particle-particle and particle-interface interactions and Interactions between particles adsorbed at the interface

adsorption kinetics, surface/interfacial tension, contact angle, extent and stability of np coverage

foam/emulsion stability, oil-water separation, transport in porous media,...

Figure 1.1: Multiscale approach followed to establish applications for ethyl cellulose nanoparticles in multiphase systems.

- At the nanoscale (single particle scale, ~nm), kinetic and thermodynamic considerations underpin the colloidal nanoparticle interactions responsible for the coagulation rate, the evolution of nanoparticle size distribution, and the adsorption to fluid interfaces or solid surfaces [69, 146, 165]. In this context, the Derjaguin-Landau-Verwey-Overbeek (DLVO) theory and its extensions are a solid basis on which to examine fundamental aspects of the colloidal interparticle interactions. Classic DLVO theory considers only electrostatic and van der Waals interactions [109], whereas other forces in the colloidal domain, including the hydrophobic [192], solvent-structure mediated, and acid-base [109] forces are accounted for in extensions of the DLVO theory. Many fundamental studies [19, 103, 152] have been recently conducted to measure the interparticle forces in the colloidal domain and to interpret these measurements using (extended-) DLVO theory.

- At the microscale (single interface scale, μm−mm), the rate of nanoparticle adsorption at fluid interfaces [16, 78, 125] or solid surfaces [2, 3], the rheological behavior of the colloidal suspensions [84], and the mechanism of stability of nanoparticle-stabilized foams and emulsions [23, 76] have been of considerable interest. Similar to surfactants, dynamic surface/interfacial tension measurements have been conducted as a promising method to characterize the adsorption of nanoparticles at fluid interfaces. It is, however, shown [16] that unlike surfactants, in most cases, nanoparticles adsorb at fluid interfaces irreversibly − suggesting a more favorable condition for stabilizing emulsions and foams.

- At the macroscale (multiple interface scale, cm−m), transparent microfluidic systems provide an ideal environment to study the transport of colloidal nanoparticles through a porous medium [56]. Moving forward from very precisely defined and ideal systems (microfluidic chips) to more realistic ones, researchers have used glass micromodels with (random) capillary networks [4, 104, 127, 182, 196]. Such systems help one to visualize [64, 183] multiphase flow patterns as fluids containing colloidal nanoparticles flow simultaneously through a porous medium and explain outcomes from microscopic (pore-scale) processes and mechanisms. Under controlled hydrodynamic conditions, the stability of oil-in-water (O/W), water-in-oil (W/O), and double emulsions (W/O/W or O/W/O) stabilized by nanoparticles can also be assessed [97, 111, 117, 128, 139, 147]. Specifically, the kinetics of nanoparticle-stabilized droplet (or bubble) coalescence and break up in a multiphase flow system has been studied [90, 121]. Studies of the transport of nanoparticle suspensions in capillary networks are strongly application-dependent and therefore, porous medium-specific. For controlling vascular drug delivery using gold nanoparticle-stabilized emulsions, for example, *in vivo* and clinical investigations are typically carried out [28, 55, 129], whereas for *in situ* water remediation or oil recovery, transport of iron nanoparticles or nanoparticle-stabilized CO_2 foams through rock samples or packed bed columns are conducted [42, 81, 119, 142, 168, 179].

1.2   Motivation

As already noted, multiphase flow in porous media is encountered in many applications, including oil production and soil/groundwater remediation. The importance of these two applications stems from their massive financial and environmental impacts. Considering the long-term significance of oil and gas as energy sources, the desire to improve the efficiency and minimize the environmental risks of hydrocarbon recovery continues to fuel

the research of multiphase flow in porous media. On the other hand, the need to remove from soil and groundwater harmful contaminants introduced by human industrial activity drives related research on multiphase flow.

In both aforementioned applications, the main goal is to displace a non-aqueous phase, often trapped in the form of blobs or ganglia within a complex network of pores in rock or soil, towards a producing well. Of various methods (thermomechanical, chemical, or microbial), the injection of foam (foam flooding) has proven particularly effective [61, 93, 95, 127, 159]. Apparently, foam, which is a dispersion of a large volume of gas in a small volume of liquid, can be generated with little mechanical energy in the presence of a surfactant; however, instability of the surfactant-stabilized foams in a subsurface medium remains a significant challenge for the foam flooding technique [46, 61]. The foam stability issue may be resolved by generating stable foams using solid nanoparticles [23, 76, 82]. The exceptional stability of these foams has been broadly attributed to the irreversible adsorption of nanoparticles at the gas-liquid interface. Very recently, super stable foams have been made from aqueous suspensions of ethyl cellulose (EC) nanoparticles which were also shown to adsorb at hexadecane-water interface [197]. EC is a non-biodegradable, non-toxic, and food-grade material produced from abundant bioresources such as trees or cotton. EC nanoparticles are hydrophobic and their aqueous suspensions are electrostatically stabilized, alleviating the need to introduce ligands. These properties make EC nanoparticle suspensions an ideal colloidal model system for fundamental studies in colloid and interface science and a potential candidate for green foam-flooding technologies. Recent foam flooding studies with nanoparticle-stabilized foams have demonstrated a significant improvement in displacement and recovery of non-aqueous blobs in comparison to flooding with surfactant-stabilized foams [119, 127, 155, 159, 195]. These promising results have not yet been accompanied by an understanding of displacement mechanisms, since the way nanoparticles assemble on gas-water and oil-water interfaces to stabilize foams and emulsions or modify the wettability of solid surfaces is still poorly understood. It is precisely these considerations that motivate the work reported herein.

1.3   Scope and thesis structure

This dissertation ultimately seeks to inform two novel engineering applications of ethyl cellulose (EC) nanoparticles: (i) fabrication of functional materials for oil-water separation and (ii) improvement of *in situ* foam flooding technology to recover oil from porous media. To this end, a number of fundamental and practical questions are posed and experiments are combined with theoretical models to answer them. Interparticle interactions

controlling the stability of aqueous EC nanoparticle colloids and the kinetics of adsorption-driven assembly of nanoparticles at fluid interfaces at different environmental conditions are studied. These studies provide an understanding of how EC nanoparticles assemble and interact at the interface and, consequently, how they stabilize foams and emulsions. The Pickering emulsions generated by EC nanoparticles are used as templates to fabricate functional porous materials for oil-water separation. Transport of EC nanoparticles under saturated and unsaturated flow in porous media is observed in glass micromodels and described using continuum models informed by microscale studies. Lastly, *in situ* foam generation and transport through a porous medium is studied in glass micromodels which permit the direct observation of displacement mechanisms, mobility control, and stability of EC nanoparticle-stabilized foams (and emulsions) in a multiphase flow system.

This dissertation comprises 8 chapters organized as follows:

- *Chapter 2* reviews the thermodynamic and kinetic theories in a colloidal domain as well as the mechanisms behind stabilization of emulsions or foams generated by nanoparticles. The current knowledge in transport of multiphase colloidal flow through a porous medium is presented in this chapter and the foam flooding technique is discussed.

- *Chapter 3* presents all the experimental methods employed in this project. This includes EC nanoparticle synthesis procedure, sample preparation protocols, and background on methods of instrumental analysis used.

- *Chapter 4* examines the interaction among EC nanoparticles in bulk aqueous suspension. In this chapter, the colloidal stability of EC nanoparticle suspensions is assessed qualitatively, quantitatively, and theoretically as a function of ionic strength.

- *Chapter 5* reports on the interaction between EC nanoparticles with different fluid interfaces (air-water or oil-water interfaces). The kinetics of EC nanoparticle adsorption to different fluid interfaces is quantitatively assessed as a function of nanoparticle concentration and ionic strength.

- *Chapter 6* presents Pickering emulsions stabilized exclusively by EC nanoparticles. Complete characterization on Pickering emulsions generated at different conditions (e.g., ionic strength, oil-to-water volume ratio, EC nanoparticle concentration) is reported in this chapter. The mechanism by which EC nanoparticles stabilize these Pickering emulsions is also discussed in the context of the findings reported in Chapters 4 and 5. Further in this chapter, a successful attempt to fabricate a hydrophobic

functional porous material using high internal phase Pickering emulsions generated by EC nanoparticles as a template is demonstrated. This novel material is shown to be effective in oil-water separation.

– *Chapter 7* contains pore-scale visualization studies using transparent glass micromodels. Transport of EC nanoparticles in a single phase (water) and a two-phase (gas-water) is presented along with continuum modelling.

– *Chapter 8* summarizes the main contributions of this PhD dissertation and provides recommendations for future work.

Chapter 2

Background and Literature Review

2.1 Ethyl cellulose (EC)

2.1.1 Chemistry and properties of EC

Ethyl cellulose is a common cellulose ether derived directly from cellulose − itself obtained from plants source, such as wood or cotton. Through etherification of cellulose, some of the hydroxyl groups (approximately 2.4 to 2.5 groups) on the repeating anhydroglucose unit are substituted by ethyl ether groups to obtain a hydrophobic molecule with the structure shown in Figure 2.1. This etherification process requires a strong solution of sodium hydroxide to convert cellulose into alkali cellulose. The alkali cellulose is then alkylated to produce ethyl cellulose [89].
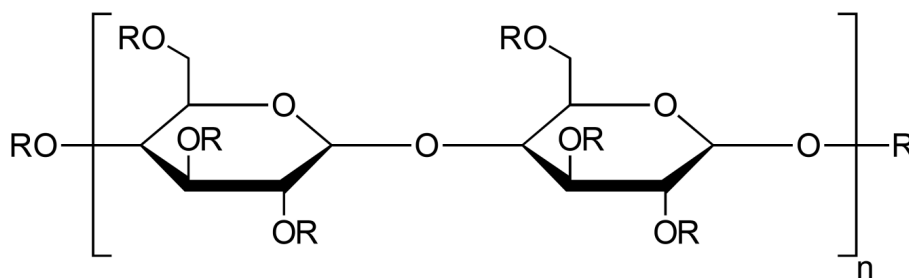
Figure 2.1: Molecular structure of ethyl cellulose. R can be either H or CH_2CH_3 representing hydroxyl or ethyl ether groups, respectively.

The degree of etherification (i.e., the ethoxy content representing the number of substituted hydroxyl groups) controls the properties of produced EC. For instance, EC is soluble in water at ethoxy content of 19% to 29% but it becomes water insoluble as the ethoxy content increases further [89]. Commercial EC products [48, 158] that usually have 47% to 48% ethoxy content (equivalent to etherification of 2.4 to 2.5 hydroxyl groups) are insoluble in water, but show significant solubility in both polar and nonpolar organic solvents. Such high ethoxy content makes EC a thermoplastic with a glass temperature of $\sim 130°C$ [34] providing useful properties that includes stability to heat and low flammability. Moreover, commercial EC is transparent to light with a wavelength of 280 nm to 400 nm. These properties together with nontoxicity, inertness to alkalies of all strengths and dilute acids, and biocompatibility make EC a preferred material for use in different applications ranging from pharmaceutical [32, 52, 137] and food preparation [38, 122] and oil recovery [74, 105].

2.1.2 EC nanoparticle synthesis

Antisolvent, co-precipitation, emulsification solvent evaporation, solvent-displacement, or nanoprecipitation are different terms referring all to a facile, inexpensive, fast, and reproducible approach to synthesize nanoparticles. In this method [137, 176, 178], the material of interest, which is usually a polymer, is dissolved into a solvent (aqueous or non-aqueous). By adding this solution abruptly to another solution that may contain a stabilizer, usually a surfactant (see Section 2.2 for more details), nano-sized particles of the desired material form immediately. If no stabilizer is desired, then pure aqueous phase is used. To successfully synthesize nanoparticles following this method, the two liquid phases must be miscible and the material of interest should necessarily be insoluble in the second solution.

This approach which will be called "antisolvent method" in this dissertation has been widely used to synthesize EC nanoparticles. Non-aqueous solvents such as acetone [82, 133], isopropyl alcohol (IPA) [15, 16], ethyl acetate [181, 190] and various stabilizers (surfactants) including sodium dodecyl sulfate (SDS), polysorbate 20, Polyoxyethylene (23) lauryl ether (Brij 35), Polyvinyl alcohol (PVA), or cetyltrimethylammonium bromide (CTAB) [181, 190] have been used to synthesize surfactant-stabilized EC nanoparticles. Very recently, EC nanoparticles have been also successfully synthesized in surfactant-free media and were shown to be electrostatically stabilized in an aqueous phase [15, 16, 82]. The negative surface charge on the bare EC nanoparticles originates from the hydroxyl or ethyl ether groups in the structure of an EC molecule. Long-term stability of aqueous suspensions of EC nanoparticles is the consequence of forces and interactions in the colloidal domain which are discussed in detail in the following section.

2.2 Forces and interactions in a colloidal domain

The coagulation of nanoparticles in the bulk and their adsorption-driven assembly at fluid interfaces are respectively controlled by nanoparticle-nanoparticle and nanoparticle-interface interactions. Even though the origin of all forces that play significant roles in the colloidal domain is still not completely understood [45], these forces can be simply identified as attractive or repulsive. Predominantly attractive interactions promote nanoparticle coagulation in the bulk or adsorption at fluid interfaces, whereas predominantly repulsive interactions pose energetic barriers to such processes. The attractive forces comprising London dispersion, Keesom, and Debye forces are known collectively as van der Waals interactions. Since such interactions between two spherical colloids are proportional to h^{-6} (h is the separation distance between two interacting bodies), the range of van der Waals interactions is very short [166]. Long range attraction has nevertheless been observed between colloidal particles possessing hydrophobic surfaces [79]. Even after several decades of research [114], a clear understanding of the origin of this type of interparticle interaction, hereafter referred to as "hydrophobic interaction", does not exist. It is generally believed that water molecules need to rearrange (reduction in entropy) to accept insoluble "hydrophobic" species that tend to stay close to each other to minimize the contact with water molecules (increase in enthalpy). Therefore, hydrophobic interaction must be attractive in an aqueous phase in order to provide an entropy-enthalpy balance in terms of Gibbs free energy, as required of a thermodynamically stable condition [166].

Repulsive forces in the colloidal domain have diverse origin. The first type of repulsive force, shown in Figure 2.2(a), arises from the interaction of nanoparticles carrying the same surface charge. In colloidal suspensions, the charged particles would attract an equivalent
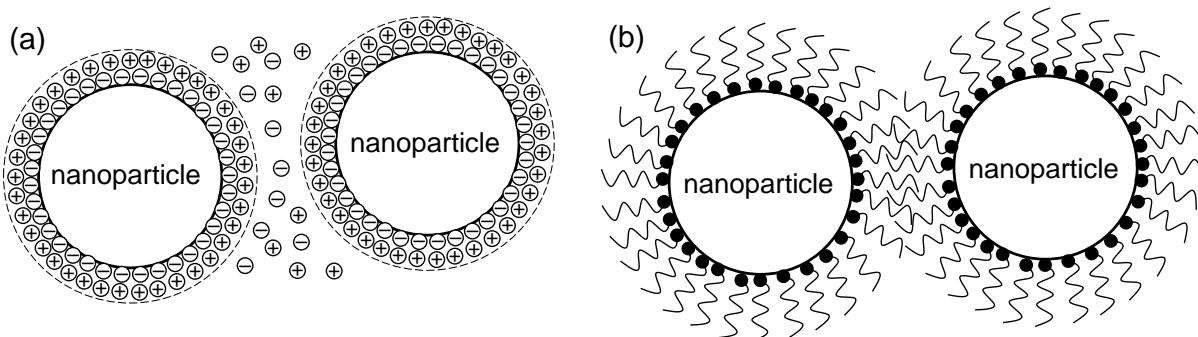
Figure 2.2: (a) Electrostatic (b) Steric repulsive forces between two nanoparticles.

9

amount of counterions inducing an electrically neutral double layer (shown by a dashed circle in Figure 2.2(a)).

Moving far enough from the charged surface, the electrical potential decreases from an initial value (i.e., surface potential) to zero. The potential at three locations is of interest: I. at the particle surface (Ψ_0), II. at the compact layer of strongly adsorbed counterions (known as the Stern layer, Ψ_d), and III. at a distance from the surface equal to the Debye length (κ^{-1}), the distance beyond which electrical charges are effectively screened (where the potential is known as the ζ-(zeta) potential) [123]. These potentials are shown in Figure 2.3. By changing the pH or by adding salt to a colloidal suspension, the double layer thickness (and Debye length) shrinks and as a result the repulsion between two like-charge nanoparticles is weakened leading possibly to coagulation.
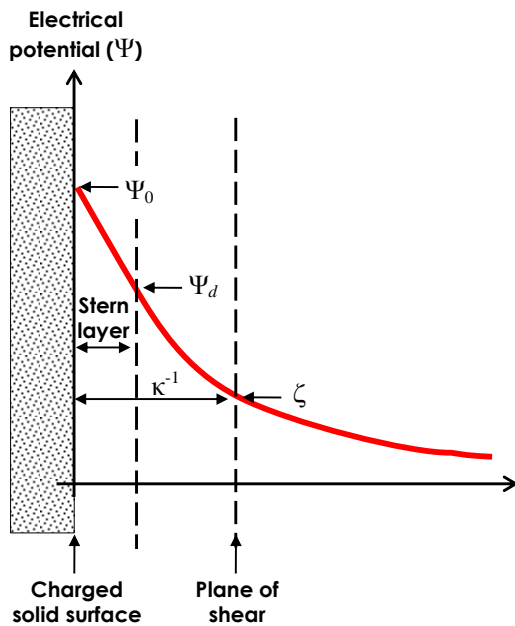
Figure 2.3: Structure of a double layer and the corresponding potentials.

The other type of repulsive force shown in Figure 2.2(b) is steric in nature and is present for colloidal particles coated by polymer molecules or surfactants. This repulsive interaction is basically due to entropic factors [166]. In a "good" solvent, the polymer chains attached on the particle surface extend out to reach the maximum of entropy. When two polymer-coated particles approach one another, the polymer chains lose their configurational entropy

resulting in "steric" repulsion [166]. Therefore, the chain length of coating agents controls the effectiveness of steric repulsion. The total interaction potential, which is the sum of all attractive and repulsive forces, dictates the stability of a colloidal suspension in the bulk and determines energy barriers associated with the adsorption of nanoparticles at the interface. One of the most reliable and well-developed theories quantitatively addressing the pair interactions is the DLVO theory and its extended form is reviewed in the next section.

2.2.1 (extended-) DLVO theory

The classic DLVO theory, named after B. V. Derjaguin, L. Landau, E. J. W. Verwey, and J. Th. G. Overbeek, was developed to quantify the pair interactions in the colloidal domain. It is assumed in this theory that the total interaction energy in a colloidal suspension is the summation of attractive van der Waals forces and repulsive electrostatic (or double-layer) force. The former depends on the nature of the particles and the medium, whereas the latter has its origin in double layer overlap of two approaching like charge particles [45].

For interactions between two colloidal particles of identical radius (r) and composition, the van der Waals interaction energy (Φ_{vdW}^{p-p}) is given by [45]

$$\Phi_{vdW}^{p-p} = -\frac{H_{121}}{12}\frac{r}{h} \tag{2.1}$$

where h is the separation distance (surface-to-surface) between two colloidal particles, and H_{121} is the Hamaker constant for the two interacting particles (noted as 1) in the liquid medium (noted as 2). The negative sign in Eq. 2.1 denotes attractive interaction. The electrostatic repulsive energy (Φ_{elec}^{p-p}), between two colloidal particles with the same size and particle surface charge (Ψ_p), can be found from the following equation [45]

$$\Phi_{elec}^{p-p} = 2\pi\varepsilon_0\varepsilon_r r\Psi_p^2\left\{\ln\left[\frac{1+\exp(-\kappa h)}{1-\exp(-\kappa h)}\right] + \ln[1+\exp(-2\kappa h)]\right\} \tag{2.2}$$

where ε_0 (= 8.854×10^{-12} C^{2}J^{-1}m^{-1}) is the vacuum permittivity, ε_r is the relative permittivity of the solvent ($\varepsilon_r = 78.5$ for water at 25 °C), and κ is the inverse Debye length. Particle surface potential is commonly approximated by the values of ζ-potential [45]. Traditionally, the van der Waals and electrostatic forces have been known collectively as the DLVO forces, whereas other forces mentioned in Section 2.2 are referred to as "non-DLVO" forces. Consideration of these forces is necessary because classical DLVO theory cannot

always describe the behavior of colloidal systems. The system of interest in this dissertation is the aqueous colloidal suspension of hydrophobic, ligand-free EC nanoparticles. Thus, among the non-DLVO forces previously mentioned, only the hydrophobic attractive interaction is likely to be present and, for this reason, reviewed here.

The physical origin of hydrophobic attraction is hotly debated and a theoretical basis for the computation of the hydrophobic interaction energy (Φ_H) has not been established yet. Rather, experimental measurements of attractive forces between two hydrophobic surfaces have been modeled empirically using an expression similar to the one used for van der Waals interactions [192]

$$\Phi_H = -\frac{K_{132}r}{h} \tag{2.3}$$

where K_{132} is the hydrophobic interaction energy constant between solid 1 and solid 2 in the medium 3. Yoon *et al.* [192] have correlated K_{132} with surrogates of surface hydrophobicity, namely with the contact angles of water on each of the two interacting hydrophobic solid surfaces *via*

$$\log K_{132} = a\left(\frac{\cos\theta_1 + \cos\theta_2}{2}\right) + b \tag{2.4}$$

where θ_1 and θ_2 are the contact angle of water droplet on solid 1 and solid 2, respectively, and a and b are empirical constants. Eq. 2.4 reduces to $\log K_{132} = a\cos\theta_1 + b$ when the interacting surfaces are of the same kind, which is the case for bulk colloidal stability studies.

The colloidal stability of EC nanoparticles is controlled by all previously discussed interparticle interactions. On one hand, the attractive energies vary with the inverse of particle separation distance (see Eq. 2.1 and Eq. 2.3). On the other hand, the repulsive energy varies as a decaying exponential function of the separation distance (see Eq. 2.2). Therefore, one can expect that the total interaction energy (i.e., the summation of attractive and repulsive energies) may have local minimum/maximum values. Figure 2.4(a) shows a typical total DLVO interparticle interaction, as well as attractive and repulsive forces between two colloidal particles as a function of particle separation distance. The maximum in the DLVO total interaction curve represents the barrier to particle coagulation imposed by electrostatic repulsion. If this energy barrier is much larger than the energy associated with thermal fluctuations (i.e., $\sim k_B T$), then particles will not coagulate and instead remain in a "kinetically stable" condition [80, 166]. By tuning the ionic strength (electrolyte concentration) or pH, we can weaken the electrostatic repulsive force and make the energy barrier against coagulation smaller. At a critical ionic strength, known as critical coagulation concentration (CCC), the energy barrier opposing coagulation just disappears, see Figure 2.4 (b), and the colloidal suspension becomes unstable. More precisely, this unstable state is
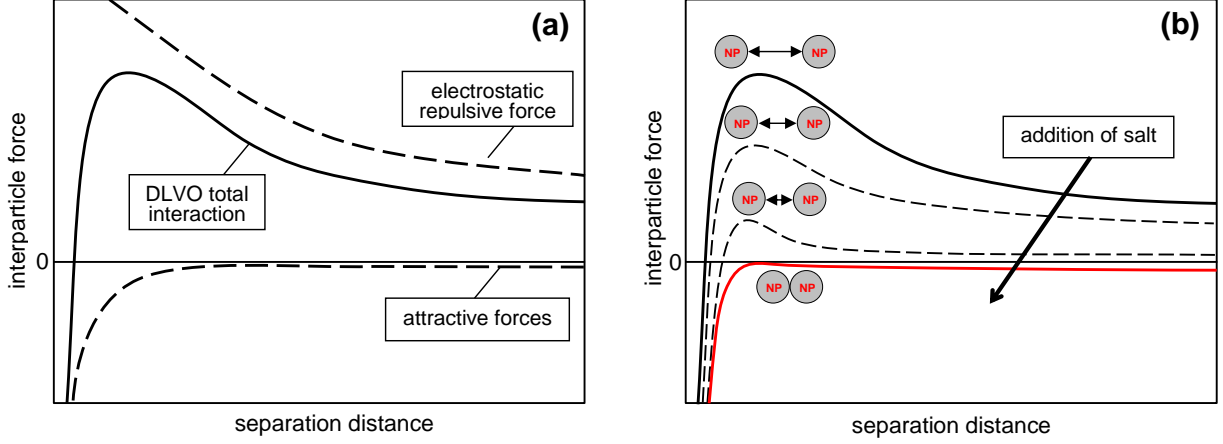
Figure 2.4: (a) Typical trends of attractive and repulsive forces between two colloidal particles and the total DLVO interaction (i.e., the summation of attractive and repulsive forces). (b) The effect of electrolyte concentration on the total interparticle interactions.

achieved not only when there is no energy barrier against coagulation, but when the total interparticle force becomes attractive at all separation distances [105]. These criteria are later used to find the CCC theoretically for NaCl in a colloidal EC nanoparticle system.

The same pair interactions exist between EC nanoparticles and fluid interfaces. Attractive van der Waals and repulsive electrostatic energies, Φ_{vdW}^{p-i} and Φ_{elec}^{p-i}, respectively, can be computed from the following equations [45]

$$\Phi_{vdW}^{p-i} = -\frac{H_{132}}{6}\frac{r}{h} \tag{2.5}$$

$$\Phi_{elec}^{p-i} = \pi\varepsilon_0\varepsilon_r r\left\{2\Psi_p\Psi_i\ln\left[\frac{1+\exp(-\kappa h)}{1-\exp(-\kappa h)}\right] + \left(\Psi_p^2+\Psi_i^2\right)\ln[1+\exp(-2\kappa h)]\right\} \tag{2.6}$$

where H_{132} is Hamaker constant for particle (1) interacting with air or oil (2) across water (3) and Ψ_i is the potential charge of the fluid interface. The hydrophobic energy between a colloidal nanoparticle and a fluid interface can be computed from Eq. 2.3. In order to obtain K_{132} from Eq. 2.4, θ_1 is found from the contact angle of water on solid 1 (nanoparticle) and θ_2 is taken to be 180° for fluid interfaces (considered perfectly hydrophobic) [148, 192]. Similar to particle-particle interaction analysis, one can compute the DLVO total interaction to predict the energy associated with the adsorption of colloidal particles at a fluid interface.

13

Once colloidal particles adsorb at the interface, the pair interactions among these particles control the ultimate surface coverage. It is proposed that if electrostatically charged particles adsorb at a nonpolar oil-water interface, they may carry "residual charges" on their surface exposed to oil, resulting in a long-range electrostatic repulsion through oil between the adsorbed particles. For colloidal EC nanoparticles studied in this work, classical DLVO interactions (i.e., van der Waals attraction and electrostatic repulsion), as well as attractive hydrophobic and repulsive dipole-dipole interactions are all effective. Dipole-dipole interactions originate from polar surface groups of hydroxyl and ethyl ether (diethyl ether) in the structure of EC molecule. Capillary force is another attractive force that has been considered in other studies [71, 96, 112], but due to the small size of EC nanoparticles it has a negligible contribution for the net interactions at the interface and is hereafter ignored (see Appendix C for more details). The aforementioned pair interactions among adsorbed nanoparticles are considered only through each phase and cross-phase interactions are excluded [112]. In this case, Eqs. 2.1 to 2.3 are not valid since the adsorbed particles are sitting between two phases. The fraction of nanoparticle at the interface exposed to either phase is controlled by the contact angle (θ). Contact angle is the key parameter to characterize and understand the behaviour of a particle adsorbed at interface and thus, the effective pair interactions must be a function of θ. Table 2.1 reports the equations proposed in the literature to compute the pair interactions between two adsorbed particles at an oil-water interface. These equations can be also applied to air-water interface.

Table 2.1: Equations to compute energies for effective interactions among adsorbed particles at interface.

interaction	medium	equation	reference
electrostatic	oil	$\Phi_{elec}^{O} = \frac{(A_{po}\sigma_{po})^2}{8\pi r \varepsilon_0 \varepsilon_r} \left\{ \frac{1}{(1+h/2r)^2} - \frac{1+h/2r}{(3+cos\theta)^2+(2+h/r)^2} \right\}$	[5, 71, 72]
dipole-dipole	oil	$\Phi_{d-d}^{O} = \frac{(\pi\sigma_d r^2 sin^2\theta)^2}{32\pi\varepsilon_0\varepsilon_o(r+h/2)^3}$	[71]
	water	$\Phi_{d-d}^{W} = \frac{(A_{pw}\sigma_{pw})^2}{16\pi\varepsilon_0\varepsilon_w^2\kappa^2(r+h/2)^3}$	

In Table 2.1, A_{po} is the surface area of particle exposed to oil, σ_{po} is the charge density on the particle surface exposed to oil, σ_d the surface dipole moment density, ε_o is relative dielectric constant of oil, A_{pw} is the surface area of particle exposed to water, and σ_{pw} is the charge density on the particle surface exposed to water. In the absence of exact equations to compute electrostatic and hydrophobic energies through water, or energies for attractive van der Waals interactions through water and oil as a function of contact angle, the Derjaguin approximation [112] is invoked in order to determine the interactions

of adsorbed nanoparticles at a fluid interface. To this end, the applicable equations can be obtained by integrating flat meniscus approximations with respect to contact angle only. This approach, which to this author's knowledge has not been reported previously in the literature, is detailed in Appendix A. Pair interaction studies and DLVO calculations provide a fundamental understanding of colloidal nanoparticle interactions with fluid interfaces, with other nanoparticles in suspension or among nanoparticles adsorbed at a fluid interface. These investigations, however, are not sufficient to probe dynamic changes in properties in the bulk or at the interface. Interactions of nanoparticles in the bulk and at fluid interfaces have kinetic aspects which are discussed in the following section.

2.3   Kinetics of coagulation and adsorption

2.3.1   Nanoparticle diffusivity in the bulk

Brownian motion is associated with the diffusion of colloidal nanoparticles in the bulk of the suspension. According to the hydrodynamic theory and using the Nernst-Einstein equation, the diffusivity of a colloidal particle (A) in the liquid (B) can be expressed as follows [13]

$$D_{AB} = k_B T \frac{u_A}{F_A} \tag{2.7}$$

where D_{AB} is the bulk diffusion coefficient of colloidal particles, k_B is the Boltzmann constant, and T is the temperature. u_A/F_A, known as the "mobility" of particle A in liquid B, is attained at steady-state conditions, where particle A executes Brownian motion as a result of force F_A. If the fluid has no tendency to slip at the surface of the particle (no-slip condition), then the mobility of the colloidal particle (u_A/F_A) in creeping flow $(Re \ll 1)$ can be computed from Stoke's law as follows

$$\frac{u_A}{F_A} = \frac{1}{6\pi\mu_B r} \tag{2.8}$$

where μ_B is the fluid viscosity. Substituting the above equation into Eq. 2.7 results in

$$D_{AB} = \frac{k_B T}{6\pi\mu_B r} \tag{2.9}$$

Eq. 2.9 is known as the Stokes-Einstein equation and has been reliably used to estimate the bulk diffusivity of spherical particles which are large relative to the size of solvent molecules in a dilute particle suspension. Diffusion of nanoparticles in the bulk along with the net pair interactions discussed earlier controls the kinetics of particle coagulation as described in detail below.

2.3.2   Particle coagulation rate

The coagulation of colloidal nanoparticles can be quantitatively predicted by the extended-DLVO theory if one considers the pair interactions in the bulk as explained in Section 2.2.1. Two limiting regimes are distinguishable in a coagulation process: diffusion-limited aggregation (DLA), and reaction-limited aggregation (RLA). DLA occurs when there is no repulsive interaction between nanocolloids and all the collisions result in coagulation (a "fast" coagulation condition). RLA represents the regime where, because of repulsive interparticle interactions, only a fraction of the collisions result in coagulation (a "slow" coagulation condition) [7, 69, 102]. These two fundamentally different regimes can be distinguished by defining a stability ratio (W) which has the value of unity for DLA and a value ranging from 1 to infinity for RLA. It is more practical to compute $1/W$, or inverse stability ratio, which for the RLA regime varies between zero and unity ($1/W = 0$ represents no coagulation and $1/W = 1$ represents a fast coagulation condition). $1/W$ is determined by normalizing the coagulation rate constant at any ionic strength (k_{coag}) to the one (k_{coag}^{fav}) at which the ionic strength is equal to or greater than the CCC (conditions favorable for coagulation) [7, 27, 69, 146]. The former is controlled by the net balance of attractive and repulsive interactions (i.e., $\Phi^{p-p} = \Phi_{vdW}^{p-p} + \Phi_H^{p-p} + \Phi_{elec}^{p-p}$ in the colloidal suspension of EC nanoparticles), but the latter is due only to attractive interactions (van der Waals and hydrophobic, $\Phi_{vdW}^{p-p} + \Phi_H^{p-p}$). Thus, $1/W$ can be estimated theoretically from [27, 69, 88, 150]

$$\frac{1}{W} = \frac{k_{coag}}{k_{coag}^{fav}} = \frac{\int_0^\infty \frac{\beta(h)}{(2r+h)^2} \exp\left(\frac{\Phi^{p-p}(h)}{k_B T}\right) dh}{\int_0^\infty \frac{\beta(h)}{(2r+h)^2} \exp\left(\frac{[\Phi_{vdW}^{p-p}(h)+\Phi_H^{p-p}(h)]}{k_B T}\right) dh} \tag{2.10}$$

where $\beta(h)$ is the hydrodynamic correction factor approximated from [27, 69, 88, 150]

$$\beta(h) \cong \frac{6(h/r)^2 + 13(h/r) + 2}{6(h/r)^2 + 4(h/r)} \tag{2.11}$$

In Eq. 2.10, the pair interactions between two nanoparticles can be computed from Eqs. 2.1 to 2.3 as discussed in Section 2.2.1. By computing and plotting $1/W$ at different values of pH or ionic strength, one can distinguish the RLA and DLA regimes and find the condition at which a stable colloidal suspension first becomes unstable.

2.3.3   Adsorption kinetics

Adsorption and self-assembly of nanoparticles at fluid interfaces is thermodynamically favored because it always results in a reduction of the free energy of the system. The magnitude of the adsorption energy is fundamental to the description of the adsorption process.

When the adsorption energy is small, of the order of a few $k_B T$, thermal fluctuations can supply the energy required to expel adsorbed particles from the interface back into the bulk and adsorption is in that case reversible. The adsorption process is effectively irreversible if a major energy barrier to desorption exists, which is the case when the adsorption energy greatly exceeds the energy that can be supplied by thermal fluctuations.

Three approaches exist for estimating the energy associated with the adsorption of colloidal particles at fluid interfaces. The first one, schematically depicted in Figure 2.5, is due to Pieranski [136] who conducted a fundamental investigation of the change in free energy associated with the placement of a single spherical particle, initially suspended in the bulk, to the fluid-fluid interface. It was shown that in the absence of line tension effects, the adsorption energy (ΔE) can be found from [17, 136]:

$$|\Delta E| = \gamma_0 \pi r^2 (1 \pm cos\theta)^2 \tag{2.12}$$

where γ_0 denotes the pristine surface (interfacial) tension and θ is the contact angle of a single particle at the interface measured through the aqueous phase. Depending on whether $\theta > 90°$ or $\theta < 90°$, the positive or negative sign, respectively, applies in Eq. 2.12. ΔE is always negative, indicating that the adsorption of particles at an interface always results in reduction of the free energy of the system. Eq. 2.12 also shows that the adsorption energy is proportional to the square of particle radius. For systems containing colloidal nanoparticles, the size can be reliably measured using dynamic light scattering (DLS) techniques (see Section 3.1.1), but finding the contact angle of a single nanoparticle at the interface is a challenge [193], posing a serious limitation on the predictive ability of Eq. 2.12.

In an alternative and more convenient approach, the adsorption energy is estimated from thermodynamic considerations [14, 40]. Here, the adsorption energy is derived from the Gibbs free energy of an interface which is fully covered by the nanoparticles.

$$|\Delta E| = \frac{\gamma_0 - \gamma_\infty}{\Theta_\infty} \pi r^2 \tag{2.13}$$

where γ_∞ and Θ_∞ are the surface (interfacial) tension and fractional coverage of the interface at steady state, respectively. Similar to Eq. 2.12, Eq. 2.13 shows that the adsorption energy is proportional to the square of particle radius. Assuming the greatest possible value for Θ_∞ (i.e., 0.91 obtained for a hexagonal close-packing pattern [14]), one can readily estimate the adsorption energy of nanoparticles using Eq. 2.13 from knowledge of the nanoparticle size and steady-state surface (interfacial) tension of the nanoparticle-laden interface. The estimate obtained is, of course, subject to the validity of the assumption

17
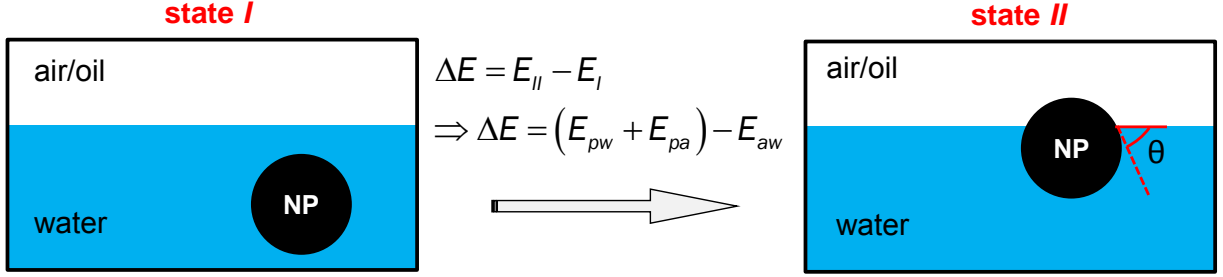
Figure 2.5: Estimation of adsorption considering the energies associated with the placement of a single nanoparticle from the bulk to the interface. E_I, and E_{II} are the energy of the interface at state I and state II, respectively. E_{pw}, E_{pa}, and E_{aw} are the energy of particle-water interface, particle-air interface, and missing air-water interface, respectively.

made about the coverage of the interface at steady state. In fact, ascertaining the value of Θ_∞ for nanoparticles at different fluid interfaces and under different environmental conditions is important not only for estimating the adsorption energy *via* Eq. 2.13, but also for understanding the mechanism behind the stabilization of Pickering emulsions and foams. This will be further explored in this thesis.

In a completely different approach [14, 16], free of the aforementioned assumption regarding the magnitude of Θ_∞, the adsorption energy of EC nanoparticles at the air-water interface is estimated from the interpretation of dynamic surface tension (DST) at the early stage of adsorption ($t \to 0$). Very recently, this approach has been successfully applied also to core-shell iron nanoparticles [125] at the n-decane-water interface. The dynamic adsorption of colloidal particles at a fluid-fluid interface is assumed to be exclusively controlled by Fickian diffusion from the bulk of the suspension to the interface. In the absence of a barrier to adsorption, the interface behaves as a perfect sink and therefore from a material balance for the adsorbed particles at the interface, one readily obtains [14, 16]

$$\Theta = 2\pi r^2 N_A C_0 \sqrt{\frac{Dt}{\pi}} \tag{2.14}$$

where Θ is the fraction of the area of the interface occupied by the particles (surface coverage), C_0 is the molar bulk concentration of particles, and N_A is Avogadro's number. Assuming quasi-steady state conditions, Eq. 2.13 can be taken to be a relationship between surface coverage and surface (interfacial) tension at any time, as follows [14]

$$|\Delta E| = \frac{\gamma_0 - \gamma}{\Theta} \pi r^2 \tag{2.15}$$

18

Eliminating Θ between Eq. 2.14 and Eq. 2.15, one gets [14, 16]

$$\gamma = \gamma_0 - 2N_A|\Delta E|C_0\sqrt{\frac{Dt}{\pi}} \tag{2.16}$$

The early-time DST or IFT data can be analyzed in terms of Eq. 2.16. To this end, the diffusion coefficient is appropriately given by the Stokes-Einstein equation (Eq. 2.9). Then, the adsorption energy, ΔE, is computed from the slope of linear regression of early-time DST or IFT data against $\sqrt{t}$. It is shown [16] that in the majority of cases, the adsorption of nanoparticles at fluid interfaces (including the adsorption of EC nanoparticles at the air-water interface) is irreversible. No dynamic equilibrium between adsorption and desorption is established under such conditions. Instead, a steady state is reached corresponding to maximum coverage of the interface by nanoparticles. The maximum coverage of the fluid interfaces can be determined a priori from an extended-DLVO model applied to the adsorbed nanoparticles, but could also be estimated *via* interpretation of DST or IFT data corresponding to the later stages ($t \to \infty$) of nanoparticle adsorption as explained next.

During the course of adsorption, as the interface approaches maximum coverage, the presence of already adsorbed particles hinders particle attachment to the interface. This effect, which is essentially steric in nature, makes the adsorption flux smaller than what Fick's law predicts. In essence, a particle that arrives at the subsurface by diffusion from the bulk of the suspension is not immediately adsorbed, but is delayed meandering in the vicinity of the interface until an uncovered portion of the interface becomes available for adsorption. A quantitative account of this phenomenon is given by the so-called blocking function ($B_0(\Theta)$). For monodispersed non-interacting spherical particles and in the context of random sequential adsorption (RSA) theory, the blocking function is approximated as $B_0(\Theta) \cong 2.32(1 - \Theta/\Theta_\infty)^3$ [2]. This expression describes simulation results for RSA of particles on solid surfaces, for which Θ_∞ is known to be ca. 0.547 for non-interacting hard spheres. In what follows, this functional form is assumed to be generally valid, albeit with Θ_∞ treated as a parameter allowed to assume different values for adsorption of colloidal nanoparticles at fluid interfaces, where Θ_∞ can potentially reach the jamming limit of 0.91. It is reasonable to expect achievement of such high values of interfacial coverage to be limited by the rate of particle rearrangement at the interface. From a material balance for the adsorbed particles at a fluid interface during the late stages of adsorption, one gets [14, 16]

$$\Theta = \Theta_\infty - \frac{K_l}{\sqrt{(\pi r^2 N_A C_0)^2 Dt}} \tag{2.17}$$

where $K_l = \Theta_\infty\sqrt{\Theta_\infty/4.64\overline{k}_a}$. The parameter $\overline{k}_a$ is the dimensionless adsorption constant

defined as follows [14, 16]

$$\overline{k}_a \equiv \frac{k_a}{\pi r^2 N_A C_0 D} \tag{2.18}$$

Following previous arguments, Θ can be eliminated between Eq. 2.17 and Eq. 2.15 resulting in [14, 16]

$$\gamma = \gamma_\infty + \frac{K_l |\Delta E|}{(\pi r^2)^2 N_A C_0} \sqrt{\frac{1}{Dt}} \tag{2.19}$$

Eq. 2.19 shows that the surface (interfacial) tension varies linearly with $\sqrt{1/t}$ during the late stages of an irreversible adsorption process. Interpretation of late-time DST or IFT data using Eq. 2.19 gives complementary insight into the parameters controlling the interfacial self-assembly of particles, the maximum coverage of particles at the interface, the barrier properties of the assembly, and the rate of particle attachment.

2.4 Stabilization of foams and emulsions by nanoparticles

More than a century ago, Pickering successfully stabilized emulsions using colloidal solid particles [135]. Pickering emulsions have unique properties which make them easily distinguishable from the ones stabilized by surfactants (common emulsifiers). Of such properties, remarkable emulsion stability is the most important one. Solid particles have shown to be great foam stabilizers as well [10, 59, 82]. Improved stabilization of emulsions and foams by particles, as compared to surfactants, is at least in part owed to the irreversible nature of particle adsorption at fluid interfaces. As discussed earlier, when the energy released during the course of adsorption ($|\Delta E|$) is of the order of thermal fluctuations ($k_B T$), the adsorption becomes reversible, whereas it is irreversible otherwise. $|\Delta E|$ for surfactants is always $\sim k_B T$ [33], whereas for solid particles the threshold to observe reversible adsorption is conservatively estimated to not exceed *ca.* 50 $k_B T$ [16]. For most colloidal particle systems, $|\Delta E|$ far exceeds this threshold resulting in irreversible adsorption to the interface. While this increases the likelihood of generating a stable emulsion, the mechanism of stabilization of emulsions by solid particles involves additional factors and is still an open issue despite numerous studies on this subject.

In general, the stabilization of fluid interfaces hinges on preventing the bubbles (in foams) or blobs (in emulsions) from coalescing [17]. In both nanoparticle-stabilized foams and emulsions, two main phenomena control the coalescence of gas bubbles or blobs leading

to foam collapse or emulsion break down, respectively [23, 169]. One is drainage of the liquid in the intermediate film under the action of gravity and capillary forces, eventually resulting in the rupture of the intermediate film. In Pickering emulsions, depending on the density of dispersed phase relative to that for continuous phase, the net action of gravity and capillary forces pushes the blobs to move to the top (creaming) or to the bottom (sedimentation). The other phenomenon, known as coarsening, concerns transport of gas from small bubbles to large ones caused by local differences in capillary pressure [23]. Coarsening in Pickering emulsions, which is also known as Oswald ripening, happens due to finite mutual solubility of the liquid phases and results in the disappearance of smaller blobs and the enlargement of larger ones [169].

It has been observed that the stability of nanoparticle-stabilized foams or emulsions depends strongly on environmental conditions, such as pH and salinity [10, 82, 170, 171]. Conditions which do not favor the stability of colloidal nanoparticles in the bulk (i.e., conditions promoting coagulation), result in the generation of more stable foams or emulsions. On the contrary, when there is no tendency for particles to coagulate, less stable foams or emulsions are obtained. Emulsion stability has been correlated with the hydrophobicity of colloidal particles (of which contact angle is a surrogate measure) which depends on environmental conditions [10]. Elsewhere [59], the stability of foams and emulsions has been related to the irreversibility of nanoparticle adsorption at fluid interfaces. As discussed in the previous section, the irreversibility of an adsorption process can be characterized by the adsorption energy ($|\Delta E|$). For a given particle size, one might expect optimal emulsion stability for the largest $|\Delta E|$, which corresponds to a contact angle of $90°$ (see Eq. 2.12). However, as experimentally shown recently [36], no stable emulsion can be generated when $\theta \cong 90°$. Clearly, the irreversibility of (nano)particle adsorption at fluid interfaces is only one of several factors underpinning the exceptional stability of nanoparticle stabilized-foams and emulsions.

Shortly after introducing Pickering emulsions for the first time, attempts were made to understand the formation and stabilization of these emulsions. Briggs [18] concluded from his experiments that *"It is absolutely necessary that the finely divided solids form a suitable film at the interface between the two liquids which are to be emulsified. If the finely divided solid forms a stable suspension in one of the liquids, it may be necessary to add a weak flocculating agent before a satisfactory emulsion can be produced; but a powerful flocculating agent will usually prevent emulsification."* The first statement in Briggs' conclusions refers to one possible mechanism, known as steric mechanism, to obtain stable Pickering emulsions. As shown in Figure 2.6(a), in the steric mechanism of stabilization, the interface is usually covered close enough to its maximal jamming limit (i.e., $\Theta_\infty \cong 91\%$) by irreversibly adsorbed particles (see Eq. 2.13). This high coverage is attainable only if a

short-range small barrier exists among the adsorbed particles [143]. When the film between two particle-covered drops drains out, at least a bilayer of particles (a multilayer can also form depending on the conditions) hinders the coalescence of drops keeping the generated emulsion stable.
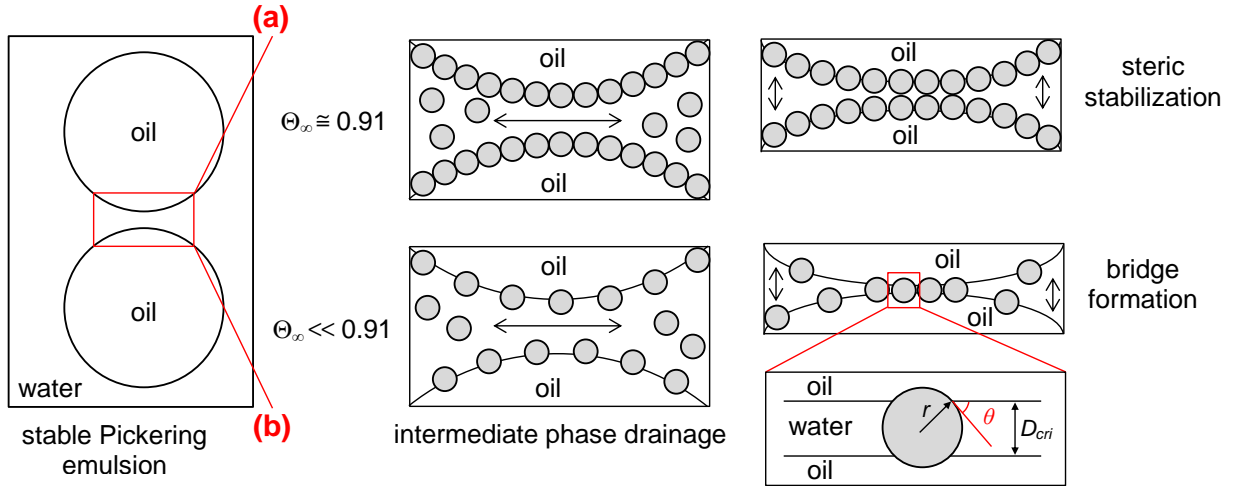
Figure 2.6: Mechanisms to obtain stable Pickering emulsions while the oil-water interface is (a) fully or (b) partially covered by the solid particles. These mechanisms are also valid for gas bubbles in nanoparticle-stabilized foam.

In a different situation, shown in Figure 2.6(b), stable Pickering emulsions are generated while the oil-water interface is initially covered by the particles much less than its maximal limit [50, 144, 180]. The mechanism behind the stabilization of such emulsions is proposed [180] and experimentally shown for a few cases [51, 73] to be the formation of a single layer of particles that is shared at the interface of two emulsion drops, or so-called bridge (see Figure 2.6(b)). When two emulsion drops barely covered by particles collide with each other, some particles might "spontaneously" adsorb at the interface of both drops forming the bridge. This could happen when the effect of bending energy, which determines the curvature of the interface, is negligible [91]. With this assumption, the bridging particles keep the two interfaces separated at a critical distance of $D_{cri} = 2r\cos\theta$ (see Figure 2.6(b)) [91]. At the theoretical limit of $\theta = 90°$, bridging particles cannot prevent the coalescence of two interfaces and therefore an unstable emulsion is obtained. This has been also experimentally observed with surface-modified latex particles with $\theta = 90°$ at hexadecane-water interface at a controlled pH [36]. In general, for a scenario shown in Figure 2.6(b), bridge

22

formation is effective in emulsion stabilization only if $\theta < 90°$, otherwise drop coalescence takes place. To obtain a stable emulsion, the estimated D_{cri} for a given emulsion must also be larger than another critical distance below which a net attractive force is experienced between two emulsion drops. This critical distance can be obtained by summing up all the effective attractive and repulsive interactions *via* (extended-)DLVO theory. Quantitative analysis on such interactions, however, has not been provided in the literature. In both situations (full and partial interface coverage), direct experimental observations have been reported when micron-size particles were used as the emulsifier [73, 130]. For stable Pickering emulsions generated by nanoparticles, elucidation of the operative stabilization mechanism must rely on indirect observations and interpretations, but similar stabilization mechanisms are expected to apply [70].

The second part of Briggs' conclusions highlights the conditions leading to the steric stabilization mechanism. When the emulsifier is charged nanoparticles, a "flocculating agent" alters the ionic strength and therefore the interactions among the adsorbed nanoparticles at the oil-water (or gas-water) interface. This controls the ultimate surface coverage (Θ_∞) − the main parameter which, as discussed earlier, selects the mechanism behind Pickering emulsion stabilization. Tuning the ionic strength also influences the interactions among nanoparticles in the bulk, as well as between the adsorbing nanoparticles and the oil-water interface. The former controls the colloidal stability and the latter the adsorption flux to the interface. The interplay among these dynamic process influences the formation and stabilization of Pickering emulsions. Even though some explanations [11, 183] are provided to link these kinetics to the Pickering colloidal stability, a thorough discussion is still required to understand the effect of flocculating agent on the Pickering emulsion formation and stabilization. Emulsions and foams are dispersions of immiscible fluid phases the transport of which within porous media for different applications requires consideration of additional physical processes as discussed in the following section.

2.5 Multiphase transport in porous media

2.5.1 Wettability and capillary pressure

The preference of a solid surface for one of two immiscible fluid phases in contact with is determined by the contact angle and is generally referred to as wettability. The phase through which the contact angle is less (more) than 90° is customarily known as the wetting (nonwetting) phase (see Figure 2.7(a)). From a mechanical equilibrium statement for a
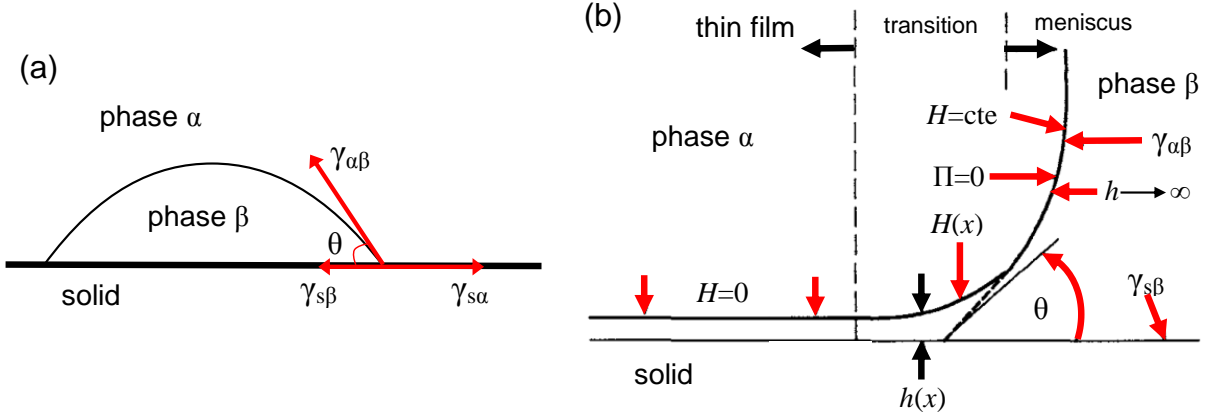
Figure 2.7: Wettability of a solid surface: phaseβ wets the solid. (a) Mechanical forces applied on the three-phase contact line and (b) microscopic schematic of a fluid interface ($\alpha\beta$) in contact with a solid surface [67].

system shown in Figure 2.7(a), Young's equation is derived for contact angle as follows [166]

$$\cos\theta = \frac{\gamma_{s\alpha} - \gamma_{s\beta}}{\gamma_{\alpha\beta}} \tag{2.20}$$

where $\gamma_{s\alpha}$, $\gamma_{s\beta}$, and $\gamma_{\alpha\beta}$ are interfacial energy (tension) of solid-phaseα (nonwetting), solid-phaseβ (wetting), and phaseα-phaseβ (fluid interface), respectively. The equilibrium state reported in Young's equation (Eq. 2.20) is in fact a balance, from a microscopic point of view, among forces interacting between the solid surface and fluid interface separated by a distance h. Due to the net action of these forces per unit area, known as disjoining pressure ($\Pi(h)$), a macroscopic contact angle is emerges [67]. If $\Pi(h) > 0$ (total repulsion), a zero contact angle is expected, otherwise ($\Pi(h) < 0$) a finite contact angle can be computed from [118]

$$\cos\theta = 1 + \frac{\int_0^{P_c} h d\Pi(h)}{\gamma_{\alpha\beta}} \tag{2.21}$$

The lower limit in the integral term in Eq. 2.21 represents long separation distances ($h \to \infty$), shown in Figure 2.7(b) at which $\Pi = 0$ and the upper limit (P_c) is the capillary (or Laplace) pressure that can be obtained from the augmented Young-Laplace equation [67]

$$P_c = 2\gamma_{nw/w}H + \Pi = \gamma\nabla \cdot \vec{n} + \Pi \tag{2.22}$$

where H is the mean curvature and $\vec{n}$ is the unit normal to the interface. At a distance where curvature disappears ($H = 0$, e.g., the thin film shown in Figure 2.7(b)), $P_c = \Pi$. In

the absence of hydrostatic gradients, the mean curvature H of static air-water or oil-water interfaces is spatially uniform and $P_{nw} - P_w = P_c$. It should be born in mind that Eq. 2.22 is a differential equation valid locally at each point on the interface. The shape of a fluid interface in contact with a solid phase (and therefore H) is a solution to Eq. 2.22, subject to a boundary condition at the three-phase contact given by the contact angle. For instance, for a synclastic interface where the centers of radii of curvature are on the same side relative to the interface (see Figure 2.8(a)), H is necessarily positive with a value of $(1/R_1 + 1/R_2)$ and thus, $P_c = P_{nw} - P_w > 0$. However, as shown in Figure 2.8(b), for anticlastic interfaces where the centers of radii of curvature are on the opposite sides of the interface, $H = (1/R_1 - 1/R_2)$ which can result in $P_c < 0$. Inside straight circular capillaries of radius R shown in Figure 2.7(c), the Eq. 2.22 has the following solution [93]:

$$P_c = \frac{2\gamma\cos\theta}{R} \tag{2.23}$$

where θ is the contact angle between the fluid interface and the solid surface measured through the wetting phase. As previously discussed, adsorption of colloidal particles modifies both the interfacial tension and the wettability and therefore influences both capillary pressure and dynamic displacement of one fluid phase by another in porous media. The
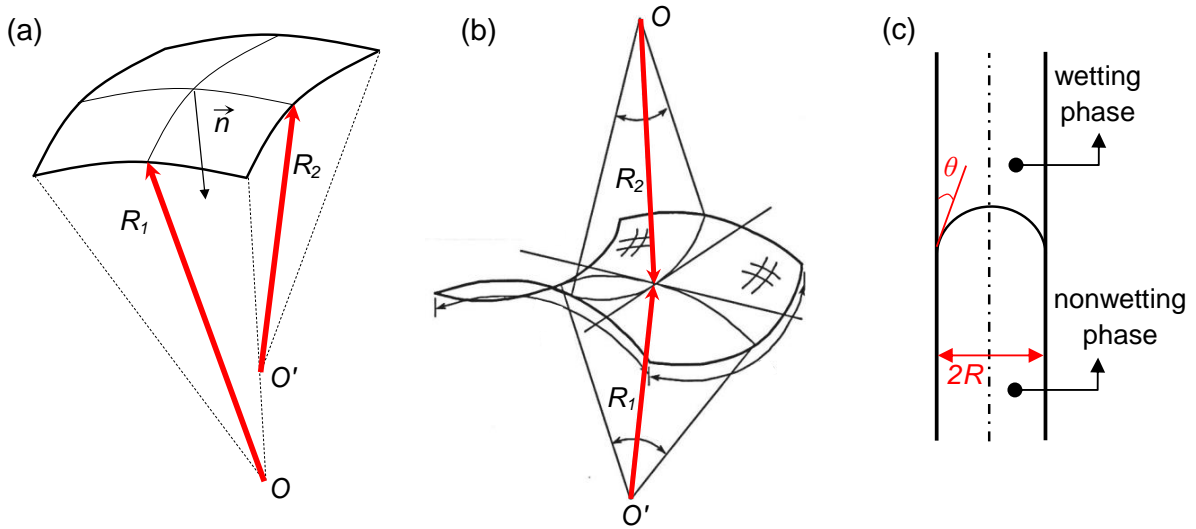
Figure 2.8: A 3D surface element of (a) a synclastic interface and (b) an anticlastic interface. (c) Two immiscible phases in a straight circular capillary tube. (b) is reprinted with permission from [153], Copyright© 1999 Taylor and Francis Group LLC Books, a division of Informa plc.

25

latter is also affected by the viscous forces at play within both fluid phases and their relative magnitude in comparison to capillary forces as explained next.

2.5.2   Immiscible displacement

Displacement of a wetting phase by a nonwetting phase in a porous medium is known as drainage, whereas the reverse (displacement of a nonwetting phase by a wetting one) is called imbibition [93], both collectively referred to as immiscible displacements. During immiscible displacement of one fluid by another within a permeable medium, the displacing fluid is known as the "invader" (the wetting phase in imbibition or the nonwetting phase in drainage) and the one which is displaced is known as the "defender" (the wetting phase in drainage the nonwetting phase in imbibition). This flow process is controlled by the physical properties of the fluids, namely viscosity, density, and surface(interfacial) tension, as well as by the saturation of the defender and its distribution within the porous medium [131]. The saturation of nonwetting and wetting phases in a porous medium, S_{nw} and S_w, respectively, are defined as the void volume occupied by the phase of interest divided by the total void volume. It is then obvious that in a two-phase flow system (oil-water or gas-water) $S_{nw} = 1 - S_w$. P_c (i.e., $P_{nw} - P_w$) is found to be a function of S_w during the course of imbibition or drainage. This functional dependence is however not unique since interfacial configurations between wetting and nonwetting phases during drainage are different from those obtained during imbibition [60, 100]. Therefore, a permanent capillary pressure hysteresis is observed (see Figure 2.9) over a broad range of S_w. The observed hysteresis can be only in part attributed to hysteresis of the contact angle. During the imbibition of water into a water-wet rock, snap-off of oil threads in pore throats and bypassing of oil-filled pores as water advances first through pore wall asperities, lead to gradual disconnection and eventual entrapment of some of the oil within the porous medium in the form of ganglia occupying one or more pores [131].

As discussed earlier, the driving forces at play in displacing the defender within a (horizontal) porous sample with a long length compared to the mean pore or grain size are capillary and viscous forces. A measure of the relative significance of these forces is the dimensionless parameter known as the capillary number, defined as $C \equiv \mu U/\gamma$. μ and U are the viscosity and the superficial velocity of invader, respectively [131]. Depending on the viscosity ratio ($\kappa \equiv \mu_2/\mu_1$, subscript "1" refers to the invader and subscript "2" refers to defender), the transient flow regime during the course of defender displacement corresponds to one of the followings [131]

 – Free imbibition
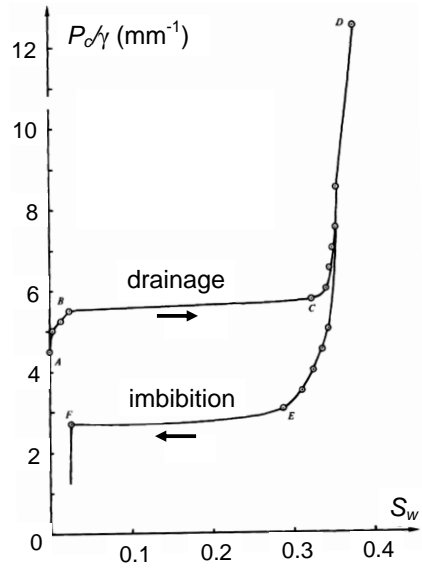
Figure 2.9: Capillary pressure curve during the drainage and imbibition in a porous medium. Reprinted with permission from [100], Copyright© 2006 Cambridge University Press.

- Imbibition with constant influx

- Quasistatic imbibition

- Dynamic invasion with constant influx and favorable/unfavorable κ

- Dynamic invasion with constant pressure drop favorable/unfavorable κ

The favorable or unfavorable κ refers to the cases where $\kappa < 1$ or $\kappa > 1$, respectively. If $\kappa < 1$ (favorable), the invader smoothly advances through the permeable medium. However, if $\kappa > 1$ (unfavorable), the invader front is unstable at sufficiently high capillary numbers forming "fingers" [131]. In the free imbibition mode, the invader is a wetting fluid invading the porous medium with a finite but not constant flow rate. Therefore, in this flow mode the capillary number is not constant (and could, in fact, at times be large) except for the cases in which the fluids have similar viscosities. For imbibition with constant influx, the capillary number is nearly constant and it is vanishingly small for quasi-static imbibition − a displacement mode characterized by very small flow rates (only one pore at a time) and modeled quite well by invasion percolation [131]. An illustration (from

27

simulations) of flow patterns during the drainage of wetting phase at constant volumetric flow rate of invader and at room temperature is shown in Figure 2.10.

Figure 2.10(a) shows the evolution of the flow pattern with the capillary number when a less viscous fluid is injected. At low capillary numbers ($\log C = -5.7$ or -6.7), the pattern is characterized by viscous fingering, whereas at much lower capillary numbers ($\log C = -9.7$ or -10.7), a different pattern, known as capillary fingering, is observed. In the second series (Figure 2.10(b)), a more viscous fluid is injected. A continuous transition between the two different aforementioned patterns is observed: unstable displacement (capillary fingering) at very low flow rates (small capillary numbers) and stable displacement (viscous fingering) at high flow rate (large capillary numbers). The third series (Figure 2.10(c)) shows the transition between viscous fingering to stable displacement by increasing the viscosity ratio at a constant capillary number ($\log C = 0$).

In the case of fingering flow patterns, the invader seeks a shortcut to bypass the less permeable regions in a porous sample [61, 131]. This significantly reduces the swept volume in the porous structure resulting in a large amount of residual nonwetting phase in the form of ganglia. The dynamics of ganglion displacement, which is the focus of EOR techniques, are briefly reviewed next.

2.5.3 Dynamic displacement of ganglia

Ganglia are formed as an end-product in a flooded porous medium as shown in Figure 2.11. These trapped nonwetting blobs cannot be effectively displaced unless the capillary number becomes quite large (ca. $\sim 10^{-4}$) [131]. During the dynamic displacement, a ganglion tries to move in many directions simultaneously which causes it to break down to smaller ones (dynamic breakup) — a common phenomenon especially in random porous media. In order to understand this problem, ganglia are distinguished by their volume and simply grouped as mobilized and stranded ones [132]. There are different scenarios for the population of these two groups [131, 132]: (i) mobilized ganglia might get stranded, (ii) mobilized ganglia may break into smaller ones or coalesce with other mobilized or stranded ones, (iii) stranded ganglia could be mobilized by the collision of moving ones. These scenarios highlight two competing dynamics. As a result of dynamic breakup of large ganglia, many stranded small ganglia are formed. However, due to collision-coalescence dynamics, large ganglia are also formed that tend to move downstream. Apparently, this competition highly depends on the probability of ganglia coalescence — a process that can be affected by the adsorption of nanoparticles at fluid interfaces. If the coalescence is less likely, then the dynamics of ganglia break up predominate. In such a case, initially trapped blobs tend
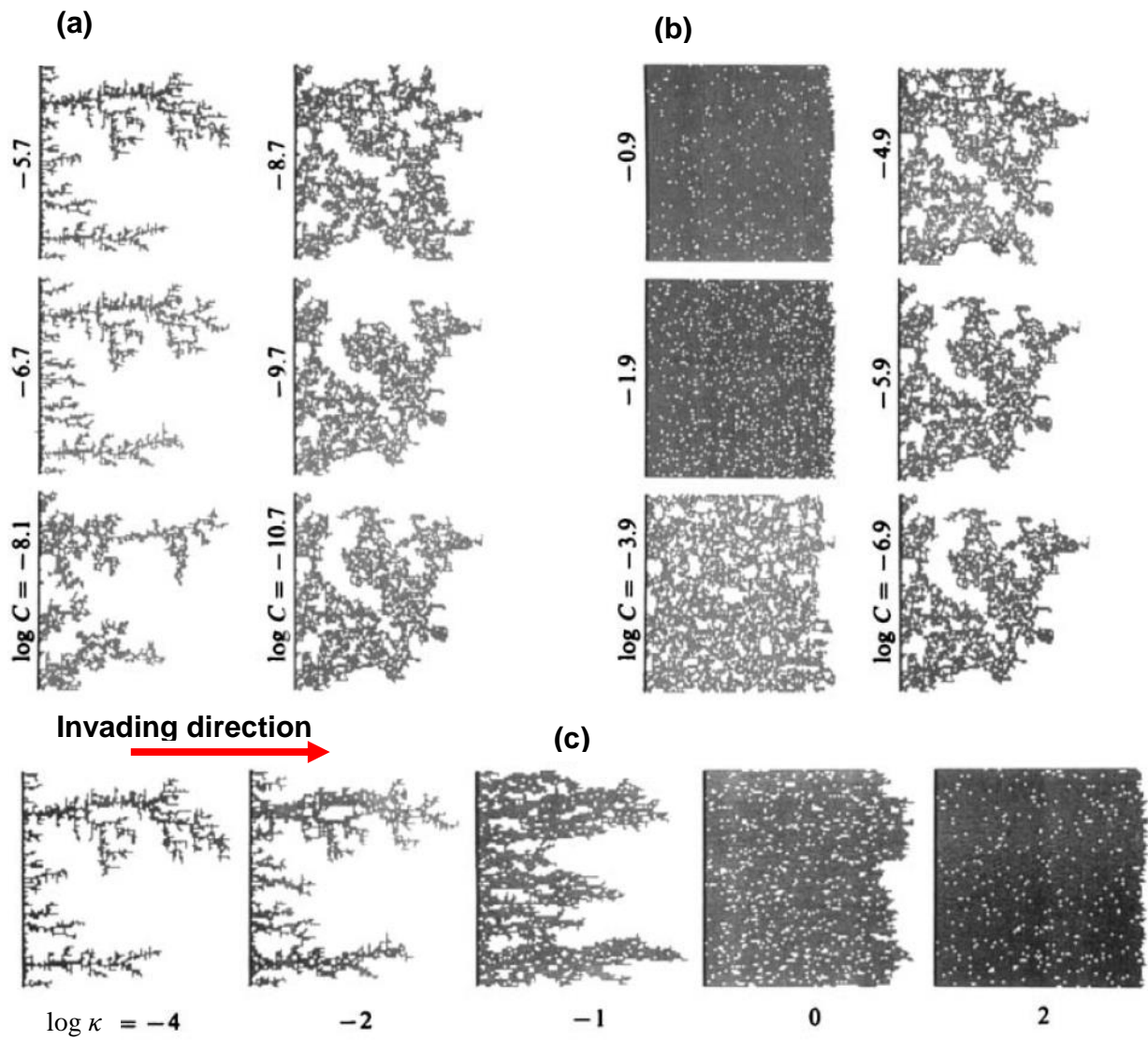
Figure 2.10: Simulations at various viscosity ratios (κ) and capillary numbers (C): (a) $\log\kappa = -4.7$, (b) $\log\kappa = 1.9$, and (c) $\log C = 0$. Reprinted with permission from [99], Copyright© 2006 Cambridge University Press.
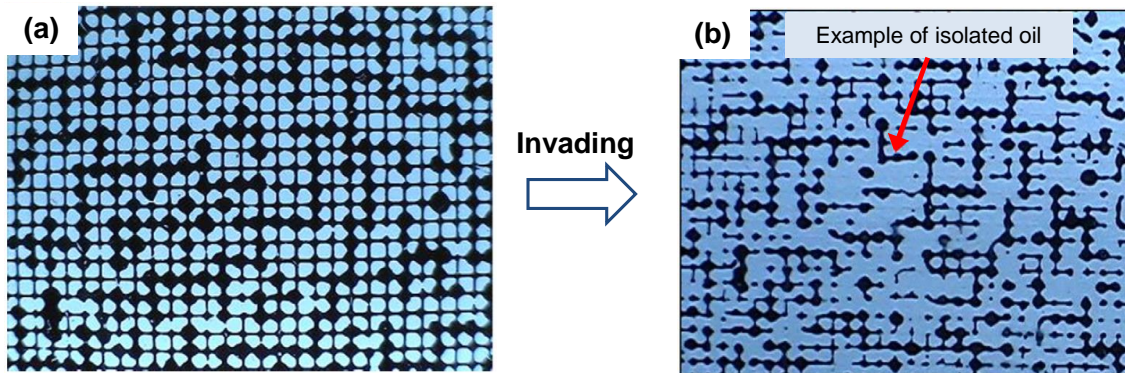
Figure 2.11: A glass micromodel (a) saturated with nonwetting defending fluid (i.e., oil) (b) after invading with wetting invading fluid (i.e., water). Reprinted with permission from [39], Copyright© 2012 Elsevier.

to break down into smaller ones − a process which makes the mobilization of ganglia (oil recovery) harder. However, if the probability of coalescence is high, the moving ganglia may reconnect forming a bank of nonwetting phase. Therefore, oil recovery or NAPL displacement would be a lot more feasible in this condition.

2.5.4 Nanoparticles for ganglion displacement in porous media

2.5.4.1 Nanoparticle flooding

Many water-flooded oil reservoirs might still contain 50% to 75% of the original oil in place (OOIP) in the form of ganglia [49]. Such ganglia might also be seen in regions where limited amount of NAPL has been introduced to groundwater and trapped within the subsurface [75]. As discussed previously, non-aqueous phases in this form can be displaced only if the capillary number becomes sufficiently large. This could happen if the interfacial tension decreases substantially following the addition of a surfactant. Surfactant flooding was therefore one of the suggested techniques to improve oil recovery or, generally, make trapped non-aqueous ganglia movable. However, the following issues with the use of surfactants are still outstanding [93]:

- Surfactant flooding is limited to light-oil reservoirs with moderate to high permeability which are rare in the world.

- Surfactants degrade at deep reservoirs due to high pressure and temperature.

- Surfactant flooding is very sensitive to high brine salinity − a common condition in oil reservoirs.

Such challenges led researchers to mix surfactant solutions with polymers [66] or use them to stabilize foams, flooding with which was shown to improve sweep efficiency [49, 61, 95].

Alternative to surfactants, nanoparticles have been used recently to modify the oil-water interfacial tension or the solid matrix wettability, and eventually mobilize trapped non-aqueous ganglia and improve oil recovery. Fairly recently [108], graphene-based amphiphilic Janus nanosheets suspended in water were used to extract up to $\sim 15\%$ of residual oil from sandstone rock cores already flooded with brine. Similarly, brined-flooded Berea sandstone core plugs were flooded with aqueous suspension of silica nanoparticles and $\sim 6\%$ more oil was recovered. The displacement mechanism and the factors resulting in such oil recovery improvements are still not well clear. However, rock and environmental properties, chemistry of nanoparticles, and nanoparticle concentration are undoubtedly relevant factors in improving ganglion displacement and oil recovery. The structural disjoining pressure mechanism [29, 195] is one of the proposed mechanisms through which a ganglion could be detached from a solid surface and be displaced (see Figure 2.12). Very briefly, nanoparticles,
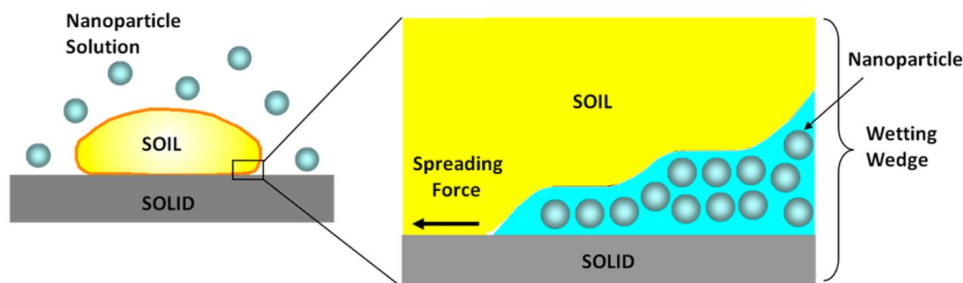
Figure 2.12: The structural disjoining pressure mechanism during the detachment of an oil blob from a solid surface. Reprinted with permission from [195], Copyright© 2015 American Chemical Society.

suspended in water, tend to rearrange themselves in the confined region close to the three-phase contact line an arrangement promoted by entropic gain. This arrangement results in a gradient in disjoining pressure, of osmotic type, within the thin film (see Figure 2.7(b) and 2.12) which makes the surrounding fluid to move into the wedge and eventually detach the oil drop (i.e., a ganglion) [29]. A more efficient method for ganglion displacement in porous media is suggested by foam flooding which is the subject of next section.

2.5.4.2   Nanoparticle-stabilized foam flooding

Immiscible displacement of residual oil by injecting gas into the reservoir is a viable oil recovery technique. Among gases commonly used in industry, carbon dioxide (CO_2) has one the highest solubility in water and oil. Due to this property, dissolved CO_2 reduces the oil viscosity resulting in a better mobility of residual oil. CO_2 may also reduce the oil density and the oil-water IFT all of which improving the oil recovery [95]. However, these effects do not suffice to efficiently recover oil, as the mobility of gas phase is still too high and poor sweep efficiency is often observed. This issue could be solved by generating CO_2 foam which has higher viscosity than gaseous CO_2 [127]. Due to the higher viscosity, foams are potentially suitable for improving the displacement efficiency by restricting flow of injected fluids in more permeable zones [61]. CO_2 foam was initially generated using surfactants, and as expected, an increase in oil recovery was observed in the laboratory. However, harsh environmental conditions in a reservoir such as high temperature and pressure as well as high salinity, have hindered the wide application and development of surfactant-stabilized CO_2 foams for EOR [119, 189].

Recently, nanoparticles have been used to stabilize foams to improve oil recovery [159, 160]. The most important advantage of using nanoparticles instead of surfactants to stabilize foams is the long-term foam stability in high temperature and high salinity conditions. Also, nanoparticles potentially have better CO_2 solvation capacity [44]. Figure 2.13 (a) and (b) compares a flooded porous medium by nitrogen foam stabilized by a common surfactant, sodium dodecyl sulfate (SDS), and a mixture of SiO_2 nanoparticles and SDS surfactant [167]. Qualitatively, shown in Figure 2.13 (a) and (b), the enhanced viscoelasticity of foam together with the reduced oil/water IFT facilitated the displacement of more residual oil blobs from the pore wall and dead end pores (better sweep efficiency). It was found by image analysis that the oil saturation (S_{nw}) after SDS-stabilized foam flooding was about 23.2%, while S_{nw} was 6.1% after SiO_2/SDS-stabilized foam flooding − a ∼17% more oil recovery. Due to the adsorption of SiO_2 nanoparticles to the gas-water interface, SiO_2/SDS-stabilized foams were more stable than that for SDS-stabilized foams. The bubbles reduced the mobility of gas phase and improved the swept volume (as expected due to the high viscosity of foam) and thus, gas channeling was avoided. At a larger scale, flooding with SiO_2/SDS-stabilized foam homogeneous and heterogeneous sand-packs resulted in recovering ∼25% more oil than that after flooding with SDS-stabilized foams [167]. Two cross-flows in a heterogeneous permeable medium, shown in Figure 2.14, appeared to be the main mechanism behind which foam swept the entire medium to its maximum, especially in the case of nanoparticle-stabilized foam flooding, resulting in improved oil recovery [160]. The first cross-flow is a diversion for foam flow from the higher

permeable medium to the lower one, as shown in Figure 2.14(a), resulting in the second cross-flow, Figure 2.14(b), where oil flow is pushed out from the lower permeable medium to the higher one making oil to move out easier from the porous medium. This behaviour during the course of foam flooding has a significant impact on EOR practices to recover oil from low permeable regions.
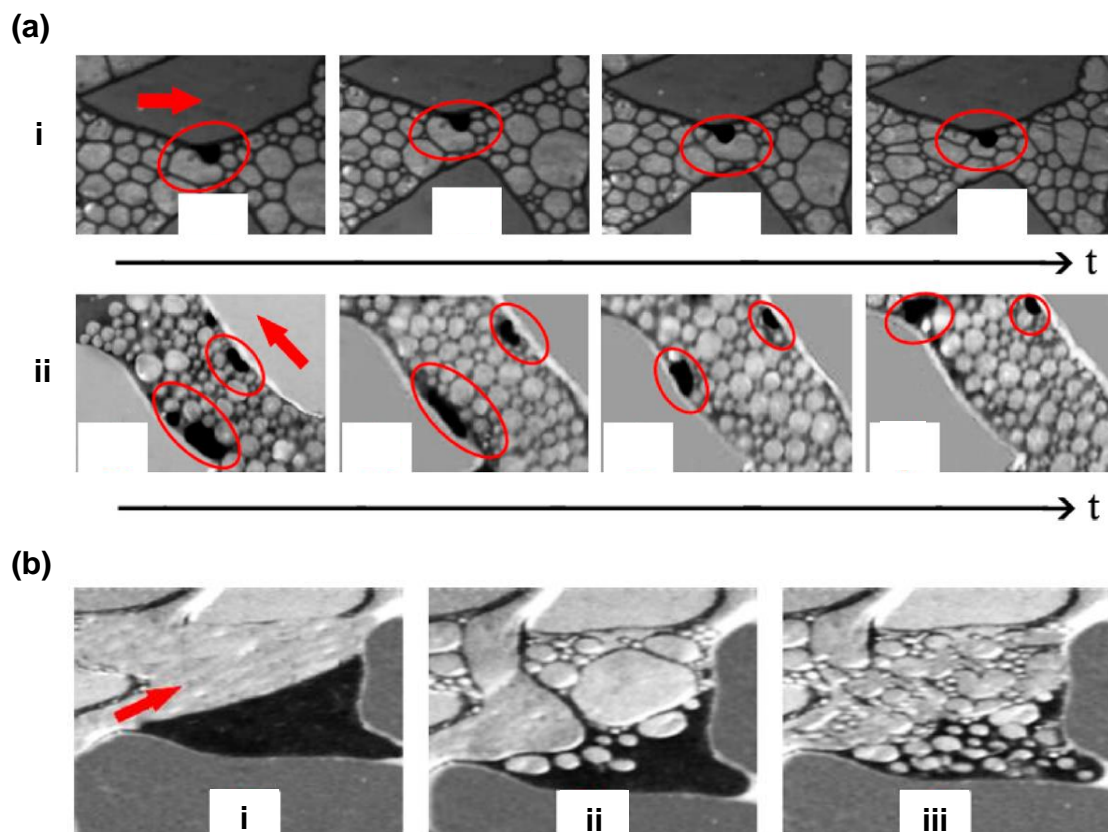
Figure 2.13: (a) Flow behaviour for (i) SDS-stabilized foam and (ii) SiO_2/SDS-stabilized foam over time in a micromodel. (b) Trapped non-aqueous phase blob in a dead-end pore swept by different displacing fluids (i) brine (ii) SDS-stabilized foam, and (iii) SiO_2/SDS-stabilized foam. Red arrow in each series of pictures shows the flow direction. Reprinted with permission from [167], Copyright© 2014 American Chemical Society.

The delivery of a gas phase to subsurface has been recently studied using a novel approach in which a gas phase develops *in situ* as water supersaturated in CO_2 is injected
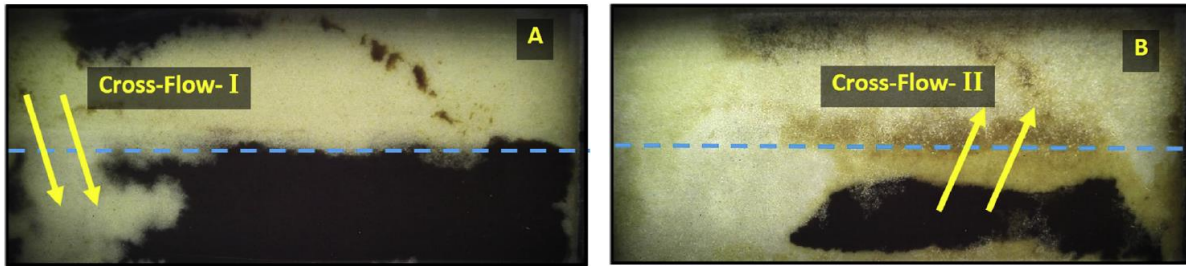
Figure 2.14: A heterogeneous medium with a high permeable region on the top (separated by a dashed line) and a low permeable region on the bottom. (a) shows the cross flow for foam and (b) shows that for oil. Reprinted with permission from [160], Copyright© 2017 Elsevier.

[43]. In this approach, departure from thermodynamic equilibrium results in the growth of gas bubbles at nucleation sites on the solid surface. Following a continued injection of supersaturated water, the gas phase grows by mass transfer from the liquid phase resulting in immiscible displacement. Eventually, under the action of capillary and buoyancy forces, the gas bubbles form gas clusters. The gas clusters grow initially in more permeable regions. Thus, the gas saturation in these regions increases and the effective permeability to the injected water decreases. As a result, the injected water is diverted to less permeable zones where gas exsolution also takes place. It is reasonable to expect that, by generating gas bubbles *in situ* in the presence of a foam stabilizing agent (e.g., nanoparticles), foam might be generated *in situ*.

2.5.5 Transport modelling of nanoparticles in porous media

Transport of nanoparticles through porous media can be assessed by conducting well-controlled laboratory experiments using glass micromodels. The colloidal suspension of nanoparticles is introduced to a micromodel under controlled conditions (i.e., fluid velocity, concentration of nanoparticles, pH, and salinity) and the effluent is analyzed over time to obtain the outlet concentration. The porous medium could be initially fully- or partially-saturated in the invading fluid that contains colloidal nanoparticles. In what follows, a continuum model is presented to study the transport of nanoparticles through a fully- or partially-saturated porous medium allowing for the possibility of irreversible adsorption of nanoparticles on collector surfaces that can be solid matrix or fluid-fluid interfaces.

As shown in Figure 2.15, one dimensional (1D) transport of colloidal nanoparticles through a homogeneous saturated porous medium is a function of travelled distance (x)

and time (t) subject to deposition on the solid matrix (i.e., collector). Assuming no consumption or production for nanoparticles in the porous medium and neglecting the changes in superficial velocity, one obtains a mass balance on the nanoparticles as follows [174, 175, 191]

$$\frac{\partial N_b}{\partial t} = D_h \frac{\partial^2 N_b}{\partial x^2} - v_p \frac{\partial N_b}{\partial x} - R_s \tag{2.24}$$

where N_b is the number concentration of nanoparticles in the bulk, D_h is the hydrodynamic dispersion coefficient, and v_p is fluid pore velocity which is assumed to be equal to colloidal particle velocity as well. The average pore velocity has been computed elsewhere [83] as a function of the superficial fluid velocity, the porosity of the medium, the colloidal particle radius, and the average pore size. Nonetheless, v_p can alternatively be computed from $v_p = QL/PV$ with the knowledge of injected volumetric flowrate (Q), pore volume (PV), and the length of porous medium (L, 1D transportation). R_s in Eq. 2.24 represents the volumetric rate of colloidal particle removal from the bulk *via* capture by the solid matrix. Eq. 2.24 is generally known as the convection-dispersion equation (CDE), or as the advection-dispersion equation (ADE) in filtration theory [191]. The first term on the
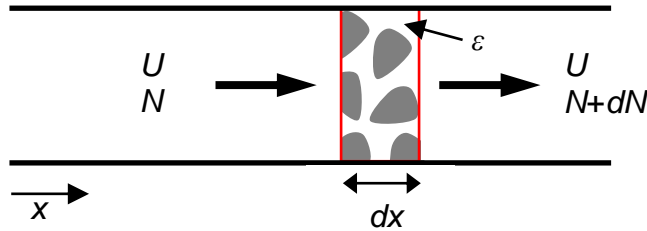
Figure 2.15: A section of a porous medium used for mass balance.

right-hand side (RHS) of Eq. 2.24 represents colloidal dispersion along the porous medium.

Once the colloidal particles (suspended in an aqueous phase) are introduced to a porous medium that is unsaturated due to the presence of gas bubbles (or nonaqueous blobs) within the structure of medium, particle-interface interactions, described in Section 2.2, might cause attachment of colloidal particles to the gas-liquid (or liquid-liquid) interface. Therefore, like the solid matrix, fluid interfaces can also act as a collector for colloidal particles. This changes the governing transport equation given in Eq. 2.24 into the following one under the assumption of constant water saturation [31]

$$\frac{\partial N_b}{\partial t} = D_h \frac{\partial^2 N_b}{\partial x^2} - v_p \frac{\partial N_b}{\partial x} - R_s - R_i \tag{2.25}$$

where R_i is the rate of colloidal particle adsorption at the fluid interfaces per bulk volume. particle-interface interactions and the energy released during the course of colloidal particle adsorption on the collector surfaces (solid matrix and fluid interface) control the reversibility of adsorption. Assuming an irreversible adsorption on both solid matrix and fluid interface, one finds R_s and R_i as follows [2, 16, 31]

$$R_s = (a_0)_s \frac{dN_s}{dt} = \frac{(a_0)_s}{\pi r^2} \frac{d\Theta_s}{dt} \tag{2.26}$$

$$R_i = (a_0)_i \frac{dN_i}{dt} = \frac{(a_0)_i}{\pi r^2} \frac{d\Theta_i}{dt} \tag{2.27}$$

N_s and N_i are the number of adsorbed particles per area of solid surface and per area of fluid interface, respectively, and where $(a_0)_s$ and $(a_0)_i$ are the surface area and interfacial area, respectively. The latter is reported in terms of water saturation as $(a_0)_i = c_1(1-S_w)^{c_2}$ [156] and references therein, where c_1 and c_2 are empirical constants. The rate of change in the coverage can be obtained from

$$\frac{d\Theta_s}{dt} = k_s \pi r^2 N_b B_s(\Theta_s) \tag{2.28}$$

$$\frac{d\Theta_i}{dt} = k_i \pi r^2 N_b B_i(\Theta_i) \tag{2.29}$$

where k_s and k_i are the adsorption constant of colloidal particles on the solid matrix and fluid interface, respectively, and B_s and B_i are blocking function effective on solid matrix and fluid interface, respectively. Depending on the corresponding coverage for the solid matrix (Θ_s) or for the interface (Θ_i), an appropriate blocking function may be obtained from consideration of Langmuir or RSA adsorption theories: $B^{Lang}(\Theta) = (1-\Theta/\Theta_\infty)$ and $B^{RSA}(\Theta) \cong 2.32(1-\Theta/\Theta_\infty)^3$ for a spherical colloidal particle system [2, 3]. Eqs. 2.26 and 2.27 represent the kinetics of single-layer adsorption on a clean collector surface. In colloid filtration theory, under conditions of fluid flow in a porous medium, the adsorption rate of colloidal nanoparticles on a collector surface, and therefore k_s or k_i, is proportional to the single-collector efficiency (η_0) and the probability of successful attachment of nanoparticle to the collector upon collision (α_{ad}) [174, 191], the latter varying between zero (no adsorption) and unity (adsorption, any collision between nanoparticle and the collector necessarily results in attachment). Despite a number of theoretical approaches [175, 191] aimed at predicting η_0, estimating this parameter is generally a difficult challenge that remains the subject of continuing research [101, 126, 174].

Under conditions of instability of a colloidal suspension, suspended particles may attach themselves to the ones already adsorbed on the surface of a collector. This could result in

multilayer adsorption of colloidal nanoparticles that adds one more kinetic term to both R_s and R_i. There have been only a few studies [87, 92] addressing processes including multilayer deposition on the surface of collectors in a flowing system involving a porous medium. Eq. 2.25 is coupled with Eqs. 2.26 and 2.27 to make a system of nonlinear partial differential equations which for suitable boundary and initial conditions constitute a model of transport of colloidal nanoparticles through an unsaturated porous medium [31, 62, 98]. The same approach can be followed to couple Eq. 2.24 with Eq. 2.26 assuming $S_w = 1$ to obtain the concentration profile of colloidal particles through a saturated porous medium [83, 87, 92]. Using both Langmuir and RSA theories, Kuhnen et al. [92] have computed the breakthrough curves for the concentration of hematite colloidal particles transported through packed quartz sand columns. The maximum coverage (Θ_∞) of solid matrix was then obtained by fitting to experimental data at different ionic strengths. Using an RSA model, provided more accurate results and it was found that the surface of collector (i.e., quartz sands) was covered close to its theoretical jamming limit when ionic strength is below CCC. This represents a single layer adsorption of colloidal particles. At or beyond CCC, however, a value of $\sim 200\%$ was obtained for Θ_∞ implying a multilayer attachment of colloidal particles to the surface of collector.

2.6 Summary

Fundamental concepts required to successfully develop an environmentally friendly approach to improve oil recovery or to displace NAPL from subsurface are reviewed in this chapter. The material of interest is nanoparticles of ethyl cellulose (EC). The chemical properties of EC nanoparticles that include the chemical bonds and structure of EC as well as approaches to synthesize nanoparticle form of EC are reviewed in the beginning of this chapter. From a nanosize perspective, the effective interactions in a colloidal domain between two nanoparticles suspending in the bulk of aqueous phase, between a nanoparticle and a fluid interface (air-water or oil-water interfaces), and between two nanoparticles adsorbed at the fluid interface are reviewed. Emphasis is placed on theoretical and experimental studies contributing to the current understanding of factors controlling the colloidal stability in bulk, the kinetics of adsorption-driven interfacial assembly, the extent of interfacial coverage, and the control of wettability. These findings serve as a basis for effective deployment of nanoparticles in stabilizing foams and emulsions as well as fabricating porous materials. Furthermore, in a larger scale, emphasis is placed on pore-scale observation of fluid interface movement in transparent micromodels and on parameters governing immiscible displacement in porous media at the pore and pore network scales,

namely the capillary pressure, the wettability, the capillary number, and the viscosity ratio. Finally, from a continuum perspective, the equations governing transport of colloidal nanoparticles through a porous medium are reviewed.

Chapter 3

Experimental Methods

3.1   Ethyl cellulose (EC) nanoparticle synthesis

An anti-solvent synthesis procedure, reported earlier [14, 16], was followed to synthesize EC nanoparticles in an aqueous phase. Briefly, commercial EC (Sigma-Aldrich, product code: 247499-100G) was dissolved in isopropyl alcohol (IPA) HPLC grade (Caledon, product code: 8601-7) at a concentration of 10.7 g L^{-1} while the solution was under stirring at $\sim$400 rpm and heating to $\sim$ 75°C on a magnetic stirrer hot plate for $\sim$30 min. By adding abruptly an equal volume of ultra-pure deionized (DI) water to the solution of EC-in-IPA, EC nanoparticles nucleated resulting in a turbid suspension. IPA was removed by heating to the boiling point of the water-IPA mixture. Heating continued until at least 50% of the initial volume evaporated and the mass concentration of EC nanoparticles in the final suspension was obtained accordingly. This highly stable aqueous suspension of EC nanoparticles was diluted to the desired concentrations by adding ultra-pure DI water. The synthesized EC nanoparticles obtained from this approach were observed by transmission electron microscopy (TEM) to be fairly spherical [14, 16, 82]. Conversion from mass concentration (ρ) to molar concentration (C) of EC nanoparticles was done using the following equation:

$$C = \frac{\rho}{\frac{4}{3}\pi r^3 \rho_p N_A} \tag{3.1}$$

where r is the radius of EC nanoparticles, ρ_p is the density of EC (1140 g L^{-1} reported by the manufacturer), and N_A is the Avogadro's number.

3.1.1 Size distribution and ζ-potential measurements

The hydrodynamic diameter of EC nanoparticles in the aqueous suspensions was determined using dynamic light scattering (DLS). DLS is an optical method which measures the evolution with time intensity of the light scattered by colloidal particles. Due to the Brownian motion of colloidal particles in the bulk, the scattered light intensity fluctuates over time ($I(t)$). Fluctuation in the intensity is fast for small particles since they move rapidly in the bulk; however, for large particles moving slowly within the solution (see Eq. 2.9), $I(t)$ fluctuates slower. Analyzing the scattered light intensity fluctuations in terms of an autocorrelation function, one can find how quickly the intensity changes on average with time. In fact, the autocorrelation function shows the delay time τ over which the intensity of scattered light becomes identical to that in the initial time. A normalized autocorrelation function is defined as follows [138]:

$$g(\tau) = \frac{\langle I(t)I(t+\tau)\rangle}{\langle I(t)\rangle^2} \tag{3.2}$$

According to Eq. 3.2, the normalized light intensity decays faster (shorter delay time) for small particles and slower (longer delay time) for large particles, reflecting how fast particles diffuse in the bulk. For a monodisperse colloidal solution $g(\tau)$ can be expressed as follows

$$g(\tau) = 1 + \beta\exp\big(-2D\mu^2\tau\big) \tag{3.3}$$

where β is the signal amplitude of the autocorrelation function, D is the translational diffusion coefficient, $\mu = 4\pi\sin(\phi/2)/\lambda$ in which ϕ is the detection angle with respect to the direction of the incident beam and λ is the wavelength of light in a given solvent [138]. Translating the measured light intensity fluctuations ($I(t)$) to normalized light intensity $g(\tau)$ using Eq. 3.2, one can determine the bulk diffusion coefficient of colloidal particles, D, by fitting Eq. 3.3 to the already calculated values of $g(\tau)$. By assuming a spherical shape for colloidal particles and using the computed diffusion coefficient, the hydrodynamic radius of particles is then easily estimated from the Stokes-Einstein theory of diffusion (see Eq. 2.9). DLS is an easy-to-operate and a fast-response technique for measuring the size of colloidal particles suspended in aqueous phases. Conducting particle size measurements over time, one can ascertain the particle coagulation and estimate the coagulation rate.

In this work, the hydrodynamic diameter of EC nanoparticles was measured using a Malvern Zetasizer Nano ZS 90 assuming a refractive index of 1.59 for EC [16, 82]. The number-based mean hydrodynamic diameter for EC nanoparticles was obtained at different levels of EC nanoparticle concentration and ionic strength. The significance of these

two factors on colloidal stability was statistically assessed following a factorial design approach. Since EC nanoparticles are negatively charged, tuning ionic strength alters their ζ-potential and therefore the colloidal stability (qualitatively observed). To theoretically assess the colloidal stability, the ζ-potential of EC nanoparticles at different ionic strength was measured with the same instrument used for nanoparticle sizing.

3.1.2 Surface (interfacial) tension measurements

As discussed in section 2.3, dynamic surface tension (DST) or interfacial tension (IFT) measurements reveal information on the adsorption of nanoparticles at fluid interfaces. A pendant drop tensiometer and its software (VCA 2500 XE, AST Products, Billerica, MA) were used in this work to determine the DST or IFT between colloidal EC nanoparticle suspensions and air-water or oil-water interfaces, respectively. This was done by axisymmetric drop shape analysis (ADSA) of the profile of a pendant drop where the surface (interfacial) tension is computed by fitting the Young-Laplace equation to the entire profile of the pendant drop. ADSA is a fast, common, and reliable technique that has been used in many other studies to measure dynamic surface (interfacial) tension of nanoparticle suspensions [16, 40, 47, 78]. A typical ADSA of the profile of a pendant drop containing EC nanoparticles surrounded by air or oil (n-decane) is shown in Figure 3.1 (a) and (b), respectively. The difference in the shape of pendant drop in air from that in oil originates
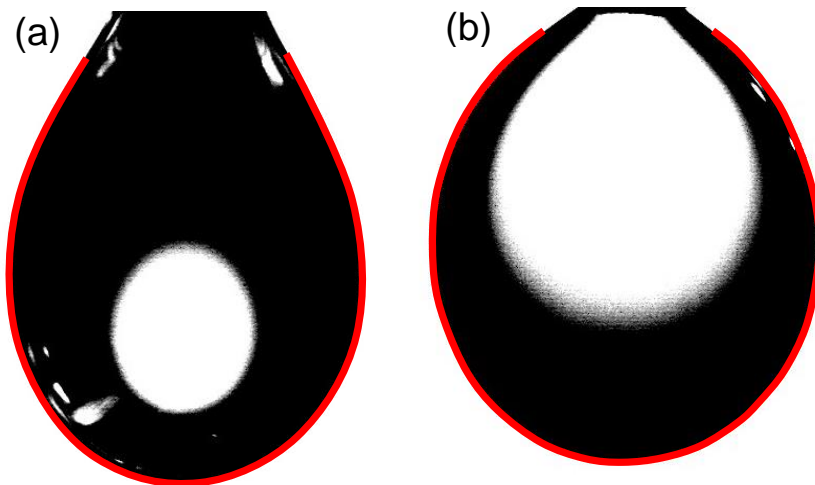
Figure 3.1: Fitting Laplace equation on the entire profile of an aqueous droplet containing EC nanoparticles surrounded by (a) air and (b) n-decane.

from a balance between two forces acting oppositely: gravity and surface (interfacial) tension. The former tends to elongate the drop, whereas the latter tends to keep the shape of the drop closer to spherical to minimize the interfacial area.

Figure 3.2 shows the schematic of computerized pendant drop instrument used in this study. For DST measurements, a drop of EC nanoparticle suspension with a preset volume
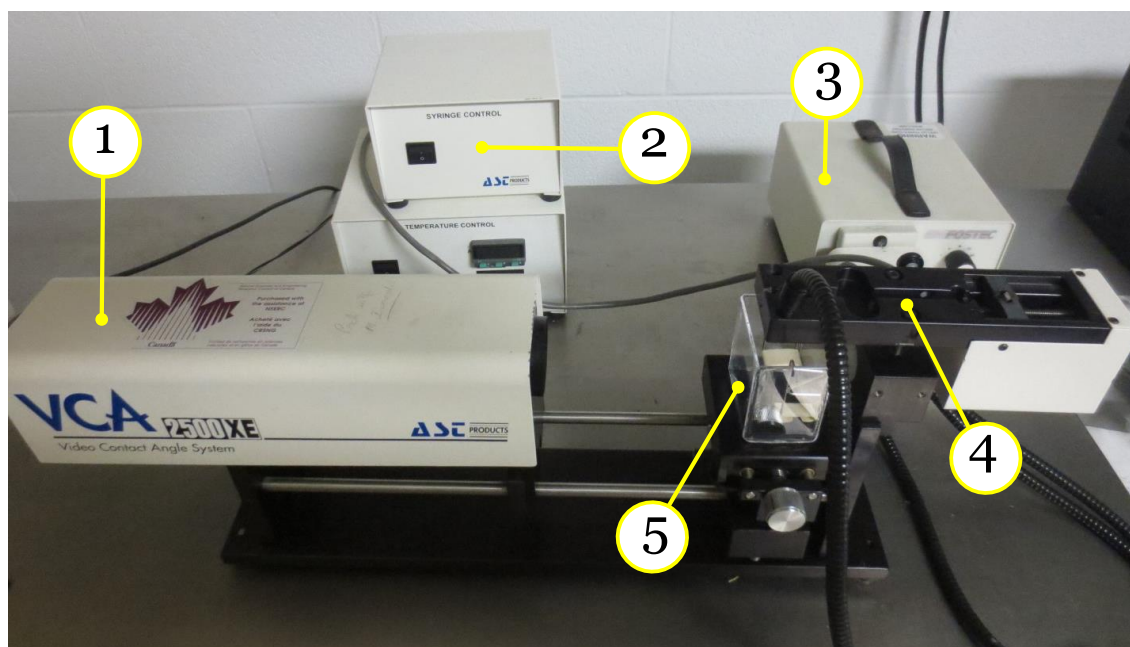
Figure 3.2: The pendant drop tensiometer: (1) high-speed CCD camera, (2) syringe controller, (3) light source, (4) micro syringe holder, and (5) glass cuvette. The high-speed CCD camera and syringe controller are both controlled by a computer.

of 8 to 12 μL, depending on nanoparticle concentration, was dispensed inside a cuvette covered with Parafilm to minimize evaporation. The high-speed CCD camera was programmed at a frame rate of $\sim$ 10 images s^{-1} to capture fast changes in DST (during the first two minutes after the formation of pendant drop). Separately, at longer times (more than couple of hours), a slower frame rate of $\sim$ 6 images min^{-1} was set to capture the images of pendant drop. A similar procedure was followed to measure the dynamic IFT between colloidal EC nanoparticle suspensions and different oil-water interfaces, except that the preset volume of pendant drop was 10 to 14 μL, depending on the EC nanoparticle concentration. The oils of interest for dynamic IFT measurements were four different

alkanes: iso-octane (J. T. Baker), n-decane (Sigma-Aldrich), n-dodecane (Matheson, Coleman, and Bell), and n-hexadecane (Sigma-Aldrich). These oils were purified, prior to any IFT measurements, by stirring with 2 wt.% Florisil$^{\circledR}$ (Sigma-Aldrich) at a speed of 450 rpm for more than half a day followed by centrifuging at 7000 rpm for 20 min [187]. The IFT of each purified oil was measured at 298 K and compared to those reported in the literature. Each set of DST or IFT measurements was repeated at least three times and the dynamics of adsorption process was analyzed using the recent asymptotic models discussed earlier in Section 2.3.3, Eq. 2.16 and Eq. 2.19 for early- and late-time data. The significance of two factors, i.e., EC concentration and ionic strength, on the interfacial properties (steady state surface (interfacial) tension, ultimate interfacial coverage, and adsorption energy) was statistically analyzed using a factorial design approach.

3.1.3 Contact angle measurements

With the same instrument used for tensiometry, the contact angle of EC nanoparticles at the air-water and oil-water interfaces was measured. The former was determined by measuring the contact angle of water drops (of varying ionic strength) on glass slides spin-coated with a solution of 4 wt.% EC in ethanol at a speed of 2000 rpm for 25 s. The contact angle of EC nanoparticles at the oil-water interface was determined using two different approaches, as shown in Figure 3.3. In both approaches, the EC film was in contact with water first and then oil was introduced − reflecting the real situation where EC nanoparticles are dispersed in water (initially wetted by water). As shown in Figure 3.3(a), a drop of ultra-pure deionized (DI) water was placed on an EC-coated glass slide. The slide was then moved to a glass cuvette filled with purified oil. Given enough time for equilibration (typically one hour), the contact angle was measured. In the other approach shown in Figure 3.3(b), oil drops on EC-coated Teflon slide (coated as the glass slides) was measured against water. To this end, oil drops were introduced to the already immersed EC coated Teflon slide in ultra-pure DI water using an inverse dispensing apparatus (the dispensing liquid, oil, had a lower density than that for the surrounding liquid, water). By these two approaches, a contact angle hysteresis was measured.

3.2 Pickering emulsion generation

A mechanical mixer (Banrant mixer series 10) equipped with a three-bladed stainless steel paddle was used to generate Pickering emulsions. For a given oil, the effects of the following
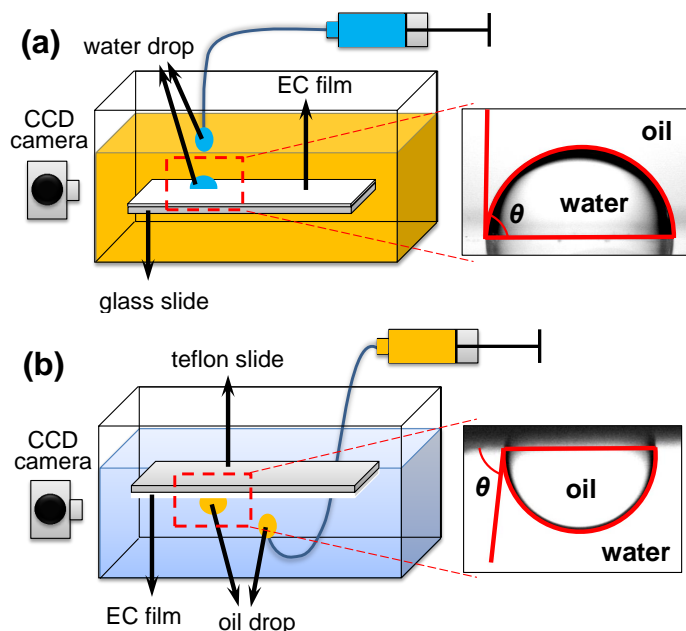
Figure 3.3: (a) Direct and (b) reverse dispensing apparatus for measuring contact angle.

five factors on the formation and stability of generated emulsions were investigated: oil-to-water volume ratio, ionic strength, EC nanoparticle concentration, mixing time, and mixing speed. Immediately after stopping the mixing, the generated emulsion was transferred to a graduated cylindrical container (a 60 mL syringe) and changes in the volume of emulsion were recorded for 24 h. The effects of mixing time and mixing speed on emulsion stability were studied and the optimum conditions for which the most stable emulsion was obtained were consequently determined. Mixing time and speed were kept constant at their optimum values to assess the effects of oil-to-water volume ratio, ionic strength, and EC nanoparticle concentration on the stability of generated Pickering emulsions. For some assessments, Pickering emulsions were generated by handshaking a 15 mL vial for 2 min that contained aqueous EC nanoparticle suspension and oil at the desired oil-to-water volume ratio, ionic strength, EC nanoparticle concentration.

3.2.1 Electrical resistivity measurements

The type of generated Pickering emulsions (oil-in-water, O/W, or water-in-oil, W/O) was determined from electrical resistivity measurements. In a liquid phase, cations and anions

44

carry the electric current. This ability is controlled by parameters such as ion concentration, ion valence, and temperature. An aqueous phase is less conductive (offering greater resistance to current transport) at low levels of ionic strength and more conductive at high ionic strength. In organic nonpolar liquids, however, where no mineral salt can be dissolved, electrical resistivity is high due to lack of free ions to carry electric current. There is a significant difference between the resistivity of purified hydrocarbons ($O(10^{12}$ Ω cm)) and ultra-pure DI water ($O(10^7$ Ω cm)) [161, 162]. This difference becomes even more significant in the presence of dissolved salt in water. An LCR meter (Quadtech, model 1920) was used to determine the order of magnitude of the resistivity of purified oil, ultra-pure DI water, and generated Pickering emulsions. In this approach, an alternating electrical current was applied to electrodes immersed in a liquid phase and from readings of the corresponding voltage, the electrical resistivity was computed. The apparatus to conduct resistivity measurements in this work is shown in Figure 3.4. These measurements
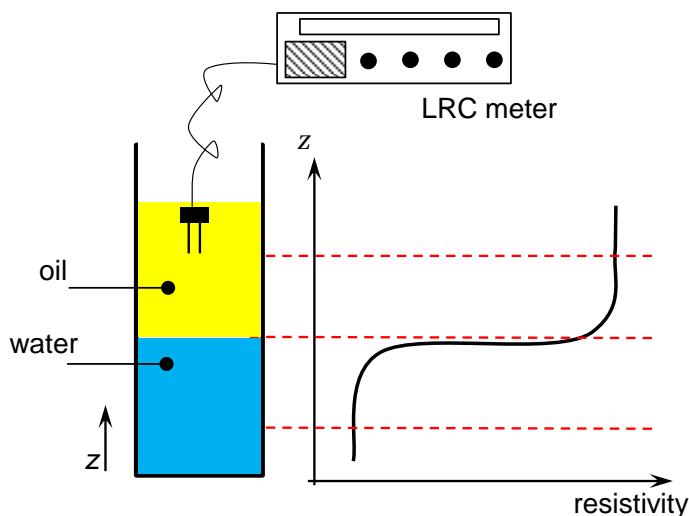
Figure 3.4: A typical output of electrical resistivity measurements.

are required to capture any possible phase inversion due to changes in emulsification conditions. Resistivity of an emulsion is closer to that for the continuous phase. If the electrical resistivity is closer to that for oil, the emulsion must be W/O, whereas if it is closer to the electrical resistivity of water, the emulsion must be O/W.

45

3.2.2 Microscopy: optical and scanning electron microscope

A Zeiss Axiovert 200 optical microscope was employed to observe the effects of oil-to-water volume ratio, ionic strength, and EC nanoparticle concentration on the size distribution of dispersed phase in the generated Pickering emulsions. To this end, a few drops of a Pickering emulsions generated by handshaking were placed on a microscope glass slide and images were taken from the drops. Pickering emulsions generated at different conditions were dried in an oven over two days at a temperature of $\sim 90°$C. The porous materials fabricated from this drying procedure were analyzed using a Quanta 250 FEG scanning electron microscope (SEM).

3.3 Transport studies

3.3.1 Glass micromodel characterization

The pore volume (PV) is a key characteristic of a glass micromodel that is controlled during the course of fabrication. The ratio between the depth of etching (δ) and width of pores bodies (w_p) or pore throats (w_t) varies between 1:2 to 1:20 [26]. Due to this ratio, in a micromodel with a uniform pattern (see Figure 3.7), the pore bodies and pore throats are assumed to have an oblate spheroid shape, shown in Figure 3.5, with a volume of $V = \frac{4}{3}\pi w^2 \delta$.
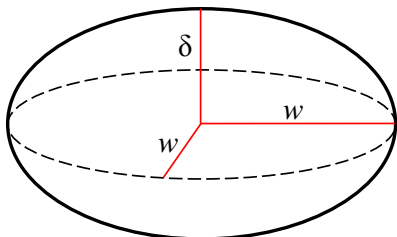
Figure 3.5: An oblate spheroid.

w_p and w_t for pore bodies and pore throats, respectively, can be obtained from images taken randomly from different sections of the glass micromodel. This has been done by running an open-source image analysis code [140] using MATLAB$^{\textregistered}$ (see Section D.1 in Appendix D). To this end, a black (pores) and white (solid matrix) image of the porous media with a given resolution in micron per pixel was used as the input to the PSD analysis

code. An "Image Segmenter" tool was used to isolate the pore bodies from pore throats and then the width of selected areas was determined from the pixels in that area. The pore size distribution (PSD) of pore bodies and pore throats was obtained by repeating the image analysis on pictures taken from different sections of glass micromodel from which the mean value for w for pores and throats was computed. Moreover, from this approach, the total number of pore bodies and pore throats was estimated.

The depth of individual pore bodies (δ_p) and pore throats (δ_t) was determined from capillary pressure measurements during the course of imbibition and drainage, respectively. In imbibition (displacement of non-wetting phase by the wetting phase), the wetting phase preferentially fills smaller radii first due to the smaller capillary pressure differences [25, 131]. Therefore, larger radii that are representative of pore bodies control the imbibition process and consequently imbibition capillary pressure (P_c^{imb}). In drainage (displacement of wetting phase by the non-wetting phase), the opposite occurs such that the smaller radii (i.e., throats) control the flow movement as well as the drainage capillary pressure (P_c^{dra}) [25]. The setup shown in Figure 3.6 was used to conduct the imbibition and drainage tests. The glass micromodel of interest was initially saturated with water
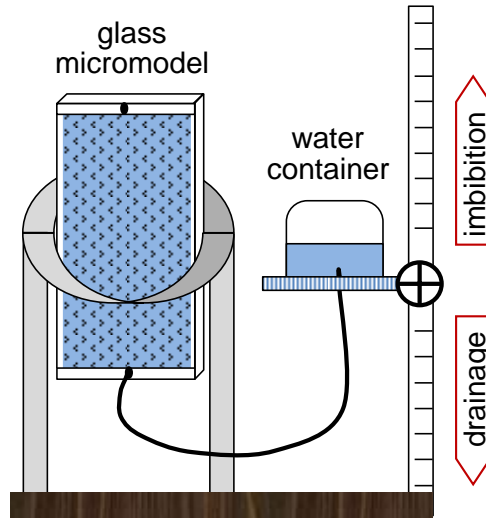
Figure 3.6: Setup for drainage and imbibition tests.

(i.e., wetting phase) and then vertically connected from one end to an elevated water container while the other end of micromodel was open to atmosphere. By lowering the water container incrementally, at a certain elevation air (non-wetting phase) started to enter the micromodel. Following equilibrium at each increment, the drainage capillary pressure is

equivalent to the hydrostatic pressure which is the height difference between the stable air-water interface (water front) in the micromodel and the water level in the connected water container. Once the whole micromodel was almost completely drained, the beaker was raised incrementally to cause imbibition. As for the drainage process, the hydrostatic pressure was measured at each increment to find the imbibition capillary pressure (P_c^{imb}). The capillary pressures measured from imbibition tests along with findings for w_p were used to calculate δ_p from the following equation [100]

$$P_c^{imb} = 2\gamma_{air-water}\left(\frac{1}{w_p} + \frac{1}{\delta_p}\right) \tag{3.4}$$

In Eq. 3.4, it is assumed that wettability is perfect. P_c^{dra}, obtained from drainage tests, was normalized as $P_c^* = P_c^{dra}\delta_t/\gamma_{air-water}$. Therefore, it is shown that for perfect wettability condition, we have [77]

$$P_c^* = \frac{8(\xi^2 + 1)\tan^{-1}\left(\frac{2\xi}{\xi^2-1}\right)}{(\xi^2 + 1)^2\tan^{-1}\left(\frac{2\xi}{\xi^2-1}\right) - 2\xi(\xi^2 + 1)} \qquad \text{if} \quad \xi \leq 1 \tag{3.5}$$

$$P_c^* = \frac{4\cos\chi}{(\xi^2 + 1)(\cos\chi - \cos\Omega)} \qquad \text{if} \quad \xi > 1 \tag{3.6}$$

where $\xi = w_t/\delta_t$ and $\Omega = \cos^{-1}[(\xi^2 - 1)/(\xi^2 + 1)]$. In Eq. 3.6, χ is the solution of the following equation [77]

$$(\cos\chi - \cos\Omega)^2\left[\frac{\pi}{2} - \chi + \sin\chi\cos\chi\right] + \cos\chi(\cos\chi - \cos\Omega)\left[2\chi - \sin\chi\cos\chi\right] - \cos^2\chi(\chi - \sin\chi\cos\Omega) = 0 \tag{3.7}$$

With the knowledge of dimensions for w_p, w_t, δ_p, and δ_t, an oblate spheroid shape was assumed for individual pore bodies and pore throats, as explained earlier, and the corresponding volumes were calculated. Finally, the total PV was obtained by summing all of the individual pore body and pore throat volumes in the given micromodel. Eqs. 3.4 to 3.7 are developed for glass micormodels with pore or throat in a form of vesica piscis (different from oblate spheroid). This, however, still provides reliable estimates for PV with acceptable accuracy.

3.3.2 Transport in glass micromodels

Transport of EC nanoparticles through a glass micromodel was studied using the setup shown in Figure 3.7. Complete saturation by water ($S_w = 1$) of the glass micromodel
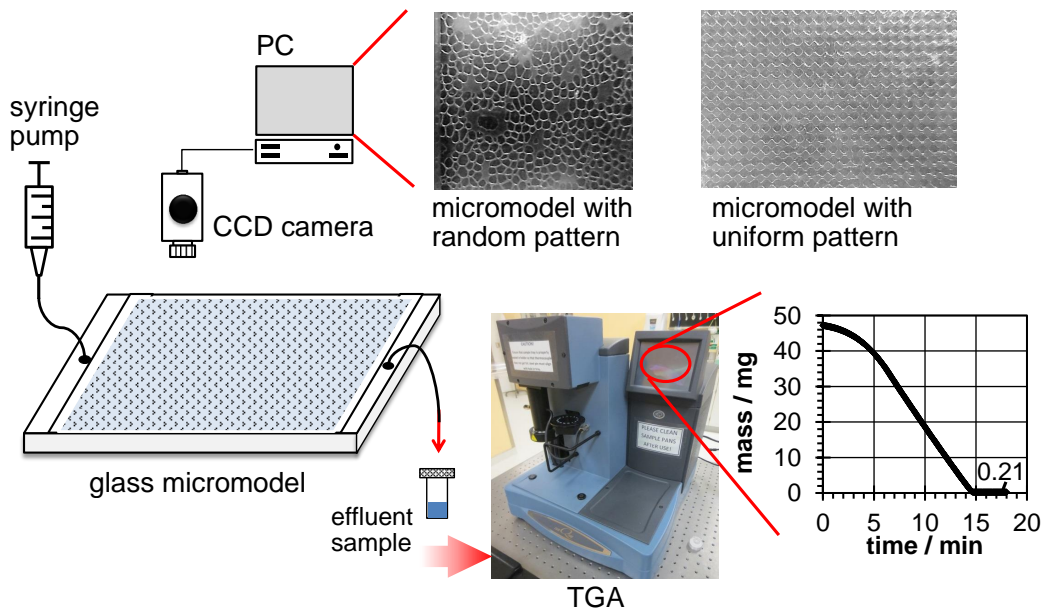
Figure 3.7: The setup used to study transport of multiphase flow in glass micromodels. Two types of micromodels used in this work (with a random or uniform pattern) are shown.

of interest was obtained by injecting CO_2 to a dried micromodel for at least 5 min followed by injection of an aqueous solution at the desired ionic strength similar to that for EC nanoparticle suspension. Following this approach [156], one could obtain $S_w = 1$ because any trapped gas bubble is of CO_2 which eventually disappeared due to relative high solubility of CO_2 in water.

As shown in Figure 3.7, using a syringe pump (NE-1000, New Era Pump System Inc.), the colloidal suspension of EC nanoparticles at the desired ionic strength was injected to the saturated or unsaturated medium with different flow rates. To determine the concentration breakthrough curves for EC nanoparticles, approximately $80\mu L$ (6 drops) was collected from the effluent and 3 droplets were discharged between each sample collection. Time was recorded for the duration of each sample collection as well as for the entire run. The samples were then analyzed using thermogravimetric analysis (TGA Q500, TA Instrument) to obtain the mass of EC in the collected sample. In TGA, the sample is placed in a chamber where a continuous mass measurement is conducted while the temperature of chamber changes according to a preset mode. In this study, samples of $50\mu L$ were pipetted onto a previously tared TGA pad and then loaded to the device. The temperature raised to 95°C at a rate of 10°C min^{-1} and maintained at 95°C for 10 minutes to completely

49

vaporize water. TGA outputted a real time graph of weight percent as a function of time, as shown in Figure 3.7. The small plateau at the end of heating period confirmed complete vaporization of water, and thus, the reading for this value showed the final weight for both EC nanoparticle and salt (NaCl). With the knowledge of mass for salt in each sample (salt concentration did not change during the course of EC nanoparticle injection), a measure for the mass of EC and thus the concentration of EC nanoparticles in the effluent was made. The breakthrough curve for EC concentration was compared with that obtained for a conservative tracer (i.e., NaCl). This was conducted following the same procedure explained earlier except that the salt solution was introduced to an ultra-pure-saturated medium at $S_w = 1$.

By co-injecting EC nanoparticle suspension and gas, *in situ* foam generation and transport in micromodel was successfully monitored with a microscope-assisted QICAM CCD camera (QImaging co.). This provided a pore-scale microscopy which was required to observe how EC nanoparticles influence the immiscible displacement of phases in porous media. Moreover, any possible pore clogging at ionic strengths larger than the CCC was captured using this imaging technique. The imaging setup shown in Figure 3.7 was used to compute the water saturation as well.

Chapter 4

Ethyl Cellulose Nanoparticles in Aqueous Phase

4.1 Introduction

Primary characterization of the synthesized EC nanoparticles in water is reported elsewhere [16, 82]. Here, dynamic light scattering (DLS) complemented by ζ-potential measurements are employed to investigate the effect of ionic strength on the colloidal stability of aqueous EC nanoparticle suspensions. The critical coagulation concentration (CCC) for NaCl is established experimentally by following a rigorous factorial design approach. The results are successfully compared with theoretical predictions obtained from an extended-DLVO model of particle-particle interactions. Effective screening of electrostatic repulsion results in nanoparticle flocculation at salt concentrations above the CCC. This provides important quantitative information while the rate of EC nanoparticle coagulation in bulk completes with the kinetics of irreversible adsorption of EC nanoparticles at fluid interfaces.

The results presented in this chapter have been published in the following paper:

N. Bizmark and M. A. Ioannidis. Effects of ionic strength on the colloidal stability and interfacial assembly of hydrophobic ethyl cellulose nanoparticles. *Langmuir*, 31(34): 9282-9289, 2015.

4.2 Colloidal stability of EC nanoparticles: Experimental approach

Colloidal EC nanoparticles are synthesized following the procedure reported in Section 3.1. It is shown in Figure 4.1 that the colloidal suspension of EC nanoparticles was stable for a long time (*ca.* months) at the ionic strength of 0.025 M (or smaller), independent to the EC nanoparticle concentration. However, the colloidal stability of the nanoparticles is completely lost at ionic strengths equal to 0.05 M or greater through a relatively fast coagulation process − a few minutes to a few days depending on the initial EC nanoparticle concentration and the ionic strength.
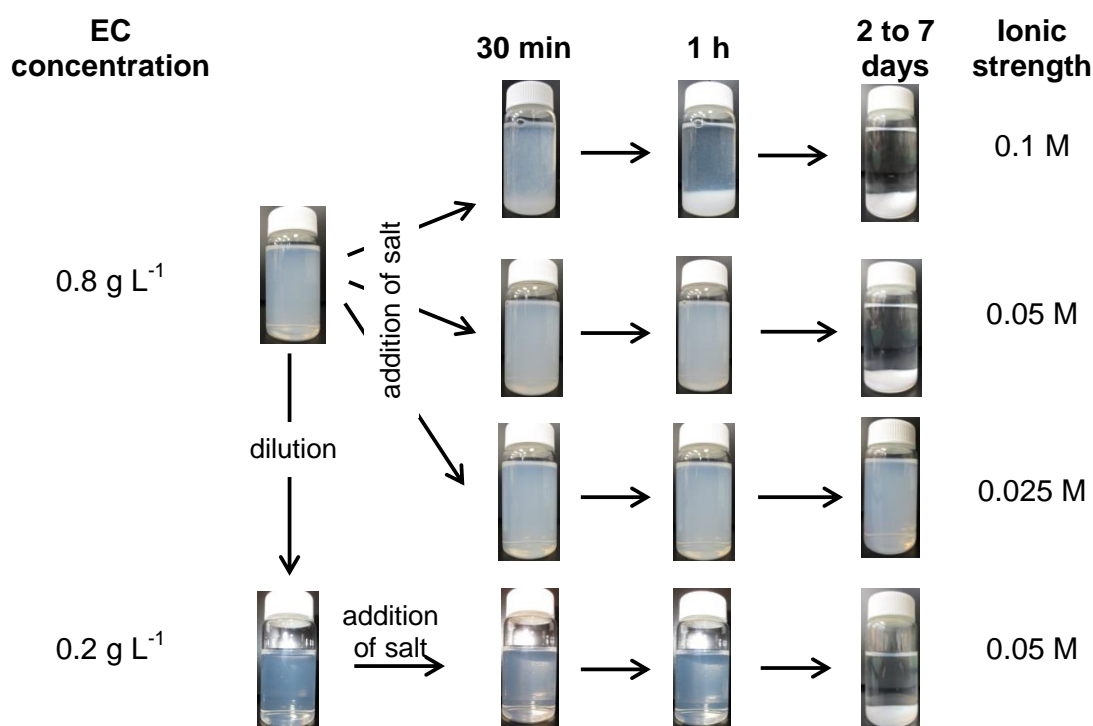
Figure 4.1: The effect of ionic strength on the colloidal stability of EC nanoparticles over time. Reprinted with permission from [15], Copyright© 2015 American Chemical Society.

52

The colloidal stability of EC nanoparticles is shown to be due to strong electrostatic (double-layer) repulsive force among the nanoparticles originating from a negative surface charge [16, 82]. This negative charge seems to be attributed to the assembly of hydroxyl ions (OH^-), provided by water molecules, at the surface of EC nanoparticles − a generic phenomenon that is hypothesized to occur on any hydrophobic surface or fluid interface (oil-water or air-water) [82]. As discussed earlier, tuning the ionic strength is expected to screen the electrostatic repulsive force, and therefore, to make the colloidal EC nanoparticles unstable. Evidently (see Figure 4.2), the increase of Na^+ ions in the colloidal EC nanoparticle suspension diminishes the magnitude of ζ-potential from an initial value of 59.08±1.76 mV, in the absence of the ion, to 15.00±0.48 mV at the ionic strength of 0.1 M. The plateau of the ζ-potential for ionic strengths of equal to or larger than 0.05 M,
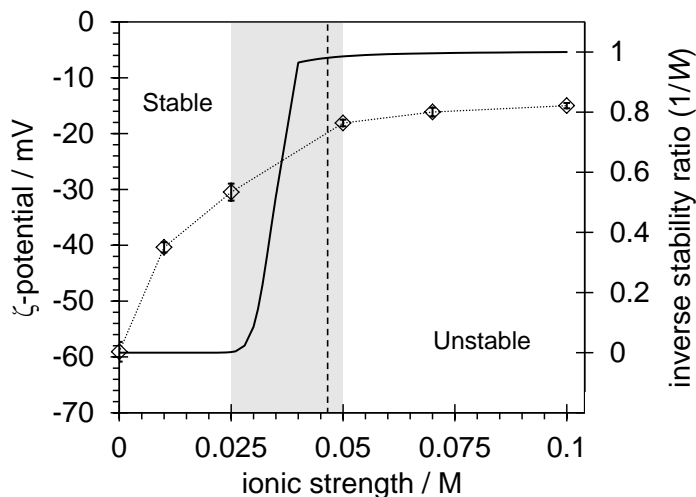
Figure 4.2: ζ-potential measurements for aqueous suspensions of EC nanoparticles at neutral pH as a function of ionic strength due to the addition of NaCl. The grey area delineates a range in which loss of colloidal stability takes place and the dashed vertical line shows the theoretical threshold ionic strength (i.e., 0.0431 M) beyond which stability is lost. The solid line shows the theoretical prediction of inverse stability ratio (see Section 4.3). Reprinted with permission from [15], Copyright© 2015 American Chemical Society.

shown in Figure 4.2, is confirmed by statistical analysis − no significant difference of the corresponding ζ-potential values was observed with 95% confidence (see Table B.1 in Appendix B). As a rule of thumb, colloidal suspensions are unstable if the absolute value of ζ-potential is smaller than 30 mV [149]. Thus, in agreement with the qualitative and quan-

Table 4.1: Factorial statistical analysis of EC nanoparticle radius (after about 2h) at different levels of ionic strength and EC nanoparticle concentration. It is assumed that each set of measurements has the same variance and the conclusions are based on 95% confidence interpretation.

ρ (g L^{-1})	compared pair	$t_{obs.}$	$T_{crt.}$ (from t-distribution table)	conclusion
	0.01 M vs. 0.025 M	2.19	2.78	1
0.2	0.01 M vs. 0.05 M	9.33	2.78	2
	0.025 M vs. 0.05 M	14.34	2.78	2
	0.01 M vs. 0.025 M	0.83	2.78	1
0.5	0.01 M vs. 0.05 M	2.93	2.78	2
	0.025 M vs. 0.05 M	2.90	2.78	2
	0.01 M vs. 0.025 M	3.11	2.57	2
0.8	0.01 M vs. 0.05 M	7.21	2.78	2
	0.025 M vs. 0.05 M	7.05	2.57	2

Note: Conclusion 1 ($t_{obs.} < T_{crt.}$) indicates no significant difference between the nanoparticle size and Conclusion 2 ($t_{obs.} > T_{crt.}$) represents otherwise.

titative results, one expects that the colloidal solution of EC nanoparticles be unstable at the ionic strength of 0.05 M or greater. The range of ionic strength within which stability of EC nanoparticle suspensions is lost due to the addition of salt is shown in Figure 4.2.

These qualitative observations are further examined quantitatively by measuring the nanoparticle size over time. The mean hydrodynamic radius of EC nanoparticles at five levels of ionic strengths (0 M, 0.01 M, 0.025 M, 0.05 M, and 0.1 M) are determined by DLS over two hours with four time intervals, with at least three replicates. The number-based average radii are shown in Figure 4.3. An average time-invariant radius of 43.96±4.92 nm is measured for colloidal EC nanoparticles at ionic strengths smaller than 0.05 M − a measurement which compares very well with the average radius in the absence of salt (i.e., 45.1±3.56 nm) [16]. However, due to flocculation, the mean radius of the nanoparticles increases at ionic strength of 0.05 M, becoming quite large at ionic strength of 0.1 M. These observations are statistically analyzed using a multi-comparison approach yielding the results reported in Table 4.1. It is demonstrated that no significant difference exists between the nanoparticle size after 2 hours at ionic strengths smaller than 0.05 M, as opposed to significant differences detected at $I = 0.05$ M or greater. This strong quantitative evidence confirms the earlier qualitative observations (see Figure 4.1). It is concluded that the CCC lies between 0.025 M and 0.05 M NaCl.
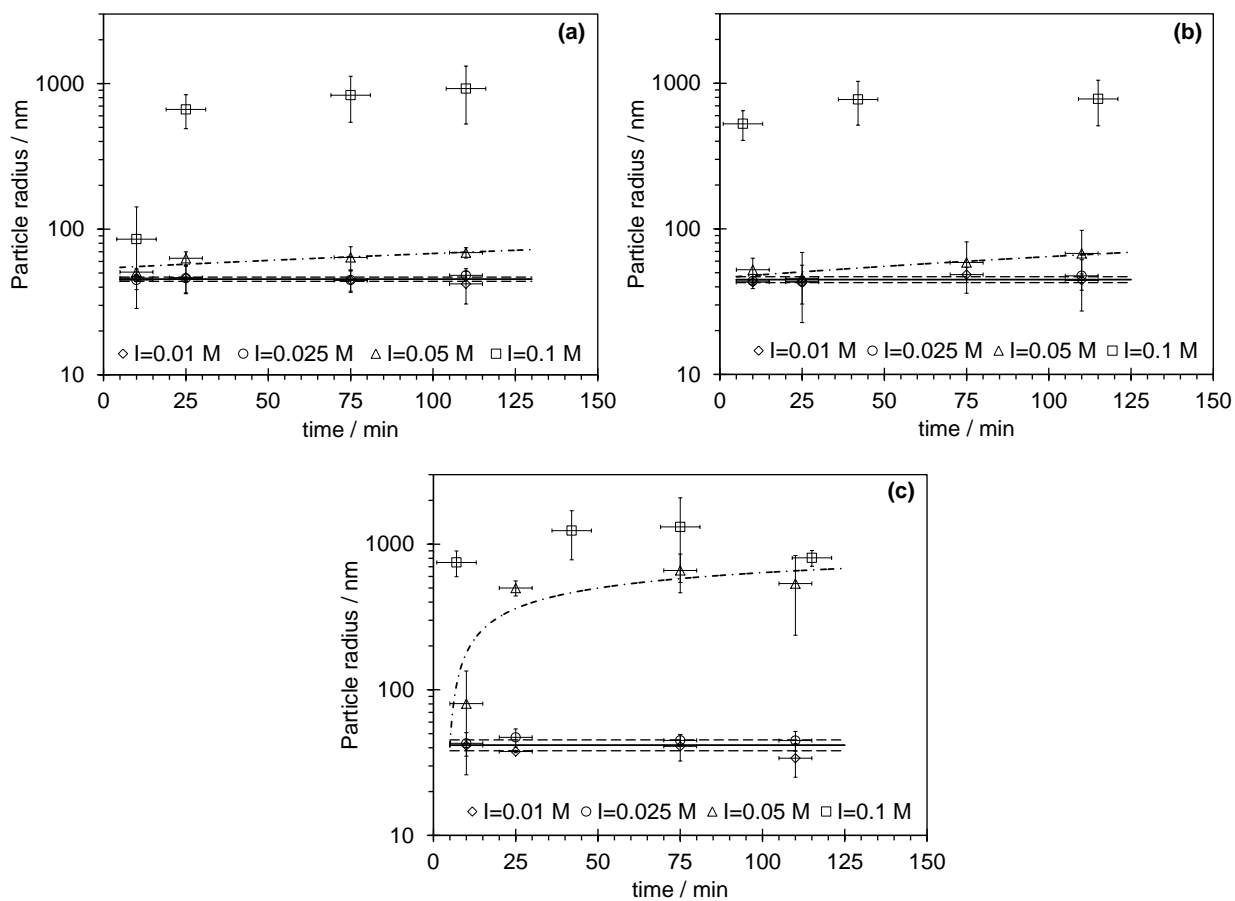
Figure 4.3: Changes in the hydrodynamic radius of EC nanoparticles over two hours at various ionic strengths and at EC nanoparticle concentration of (a) 0.2 g L^{-1}, (b) 0.5 g L^{-1}, and (c) 0.8 g L^{-1}. The solid line shows the average hydrodynamic radius with 95% confidence interval (dashed lines) and the dotted-dashed lines serve as a guide to the eye. Reprinted with permission from [15], Copyright© 2015 American Chemical Society.

4.3 Colloidal stability of EC nanoparticles: Theoretical approach

Extended-DLVO model that accounts for van der Waals, electrostatic, and hydrophobic interactions ($\Phi^{p-p} = \Phi_{vdW}^{p-p} + \Phi_{elec}^{p-p} + \Phi_{H}^{p-p}$, see Section 2.2.1) successfully predicts the limit of colloidal stability of EC nanoparticles at neutral pH and in the absence of salt [16]. By following the same approach, the total interaction energy between two EC nanoparticles of the same size given the ζ-potential at each level of ionic strength is computed and plotted in Figure 4.4. Apparently, an energy barrier in excess of 100 k_BT is estimated at the origin of long-term stability of EC nanoparticle suspensions when salt is not present (the hydrophobic attraction between EC nanoparticles is predicted to be too small). The addition of salt to the EC colloidal suspension weakens the electrostatic repulsive force, causing significant reduction of this barrier. At an ionic strength of 0.025 M, the barrier drops off to a value 10 k_BT, which is apparently just enough to prevent nanoparticle from flocculation. At ionic strengths of 0.05 M or greater, however, the predicted total interaction potential is shown to become completely attractive, favoring flocculation in agreement with assessments of colloidal stability made previously in Section 4.2. It is worth to mention that contact angle measurements at three levels of the ionic strength (0 M, 0.025 M, and 0.1 M), reported in Table B.2 in Appendix B, show no significant effect which, in the context of the extended-DLVO model employed, implies that hydrophobic interactions among EC nanoparticles are not influenced by ionic strength. Different criteria for determining the CCC from the total interaction potential have been discussed recently by Lin et al. [106]. These authors argue that the CCC is most accurately identified with the smallest value of ionic strength for which the total interaction force (as opposed to the total interaction potential) and its first derivative with respect to the separation distance (h) remain both non-positive. Using these criteria and our experimental data for ζ-potential, an estimate of the CCC from the extended-DLVO model is 0.0431 M (see Figure 4.4), in excellent agreement with experimental observations.

A transition from stable to unstable colloidal suspension takes place for ionic strengths greater than 0.025 M and smaller than 0.05 M, as indicated in Figure 4.2. This transition is reflected very well in the inverse stability ratio, $1/W$, as explained in details in Section 2.3.2. For EC nanoparticles suspended in water, $1/W$ is calculated from Eq. 2.10 and plotted in Figure 4.2. As explained in Section 2.3.2 and according to Eq. 2.10, $1/W$ varies between the values of zero and unity which correspond to two limiting regimes during the course of coagulation process: reaction-limited aggregation (RLA) for $1/W < 1$ and diffusion-limited aggregation (DLA) for $1/W = 1$ [7, 27, 69, 146]. For EC nanoparticles,
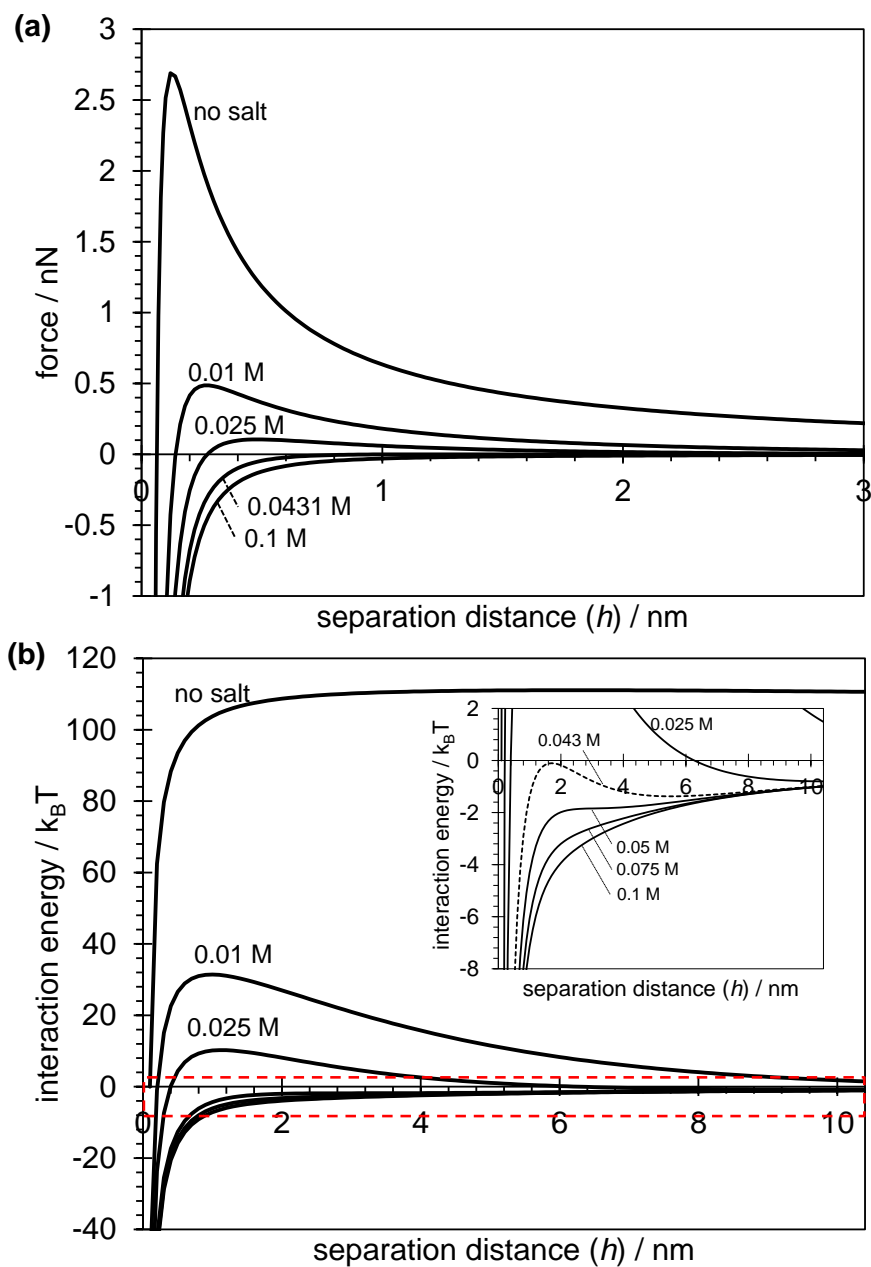
Figure 4.4: (a) Total interaction force and (b) total interaction energy between two EC nanoparticles of the same size ($r = 43.96 \pm 4.92$ nm) which is computed from extended-DLVO theory at various ionic strengths. At ionic strength of 0.0431 M the coagulation criteria (i.e., $F{=}0$ and $dF/dh{=}0$) are satisfied. The inset in (b) magnifies the dashed area. Reprinted with permission from [15], Copyright© 2015 American Chemical Society.

in the RLA regime, coagulation is kinetically limited due to electrostatic repulsion, with the effect that only a small number of collisions result in attachment (a slow coagulation condition). In the DLA regime, on the other hand, all EC nanoparticle collisions result in attachment and the rate of coagulation is limited only by diffusion (a fast coagulation condition). The RLA and DLA regimes can be easily distinguished on Figure 4.2 and the transition between the two regimes agrees with previous assessments of colloidal stability.

4.4 Summary

Aqueous colloidal suspensions of ethyl cellulose (EC) nanoparticles have shown remarkable stability for months. This colloidal stability has been attributed to the electrostatic repulsive interaction between each two EC nanoparticles. Through a systematic approach, the stability of EC nanocolloids is examined as a function of the ionic strength of the suspension. The changes in nanoparticle size are quantitatively monitored over time using dynamic light scattering followed by a factorial experiment design a multi-comparison analyses. The critical coagulation concentration for NaCl is estimated from particle size measurements and found to agree with the predictions of an extended-DLVO theory. These findings have significant implications for the fundamental understanding of colloidal systems and the practical application of utilization of colloidal EC nanoparticles in multiphase transport through porous media or for stabilizing emulsions and foams.

Chapter 5

Ethyl Cellulose Nanoparticle Adsorption at Fluid Interfaces

5.1   Introduction

EC nanoparticles have been shown to be an effective surface active agent, lowering significantly the surface or interfacial tension after adsorbing at the air-water or oil-water interface [16, 82, 197]. In the absence of salt, dynamic surface tension (DST) data reflect the irreversible adsorption and self-assembly of EC nanoparticles at air-water interface in agreement with theory [16]. Pendant drop tensiometry (see Section 3.1.2) is used here to assess the effect of salt on the adsorption kinetics of EC nanoparticles at air-water interface. A battery of dynamic interfacial tension (IFT) measurements at different levels of EC nanoparticle concentration and ionic strength are also conducted on the interface of water with various alkanes including iso-octane (iso-C8), n-decane (n-C10), n-dodecane (n-C12), and n-hexadecane (n-C16). All experimental data are statistically analyzed to quantify the adsorption parameters. These data and analyses lead to the following conclusions.

Effective screening of electrostatic repulsion results in nanoparticle aggregation for salt concentrations above the CCC, as discussed in detail in Chapter 4, but has no significant effect on the adsorption energy, steady-state surface or interfacial tension, and ultimate interface coverage. The latter is found to be close to the maximal limit (i.e., 91%) for both the air-water and alkane-water interfaces, as would be expected for tight hexagonal coverage of the interface. Nanoparticle adsorption at the air-water interface from unstable suspensions is apparently slowed down during its late stages as a result of increased blocking and/or depletion of the adsorbing species, which in all cases appear to be single nanoparticles and

not nanoparticle aggregates. It is however found that, unlike the air-water interface, the presence of salt, at a concentration below the CCC, enhances EC nanoparticle flux to the alkane-water interfaces. Faster kinetics have two possible explanations. One is reduced blocking resulting from weaker repulsive interactions among adsorbed EC nanoparticles. The other one is increase of the adsorption constant due to further reduction of an already small barrier to adsorption. On the contrary, above the CCC alkane-water interfaces behave similar to the for air-water interface and a decay in the adsorption flux is consistently observed for both types of interfaces. This is rationalized in terms of an increase in surface blocking resulting from the attachment of nanoparticles to nanoparticles already adsorbed at the interface. In order to further substantiate these hypotheses, the interactions among colloidal EC nanoparticles adsorbed at the alkane-water interfaces are studied by theoretical computations using extended-DLVO theory. Theoretical predictions of the ultimate coverage of the interface by nanoparticles compare favorably with estimates from experiments. These findings improve our understanding of the effect of ionic strength on the adsorption of EC nanoparticles at the air-water and alkane-interfaces understanding that is essential for generating aqueous foams and Pickering emulsions stabilized by EC nanoparticles.

The results presented in this chapter have been published in the following papers:

N. Bizmark and M. A. Ioannidis. Effects of ionic strength on the colloidal stability and interfacial assembly of hydrophobic ethyl cellulose nanoparticles. *Langmuir*, 31(34): 9282-9289, 2015.
N. Bizmark and M. A. Ioannidis. Ethyl cellulose nanoparticles at the alkane-water interface and the making of Pickering emulsion. *Submitted to Langmuir*.

5.2 Irreversible adsorption of EC nanoparticles at alkane-water interfaces

A series of IFT measurements for different alkane-water interfaces at different EC nanoparticle concentrations are shown in Figure 5.1: Figure 5.1(a), (b), (c), and (d) show the effect of EC nanoparticle concentration on dynamic IFT of iso-C8-water, n-C10-water, n-C12-water, and n-C16-water interfaces, respectively. In the absence of nanoparticles, time-independent interfacial tensions of 51.4±0.8 mN m^{-1}, 52.8±0.4 mN m^{-1}, 53.4±0.4 mN m^{-1}, and 54.4±0.5 mN m^{-1} were measured at 298 K for purified iso-C8, n-C10, n-C12, and n-C16, respectively, in excellent agreement with literature values [35, 57, 194]. In the
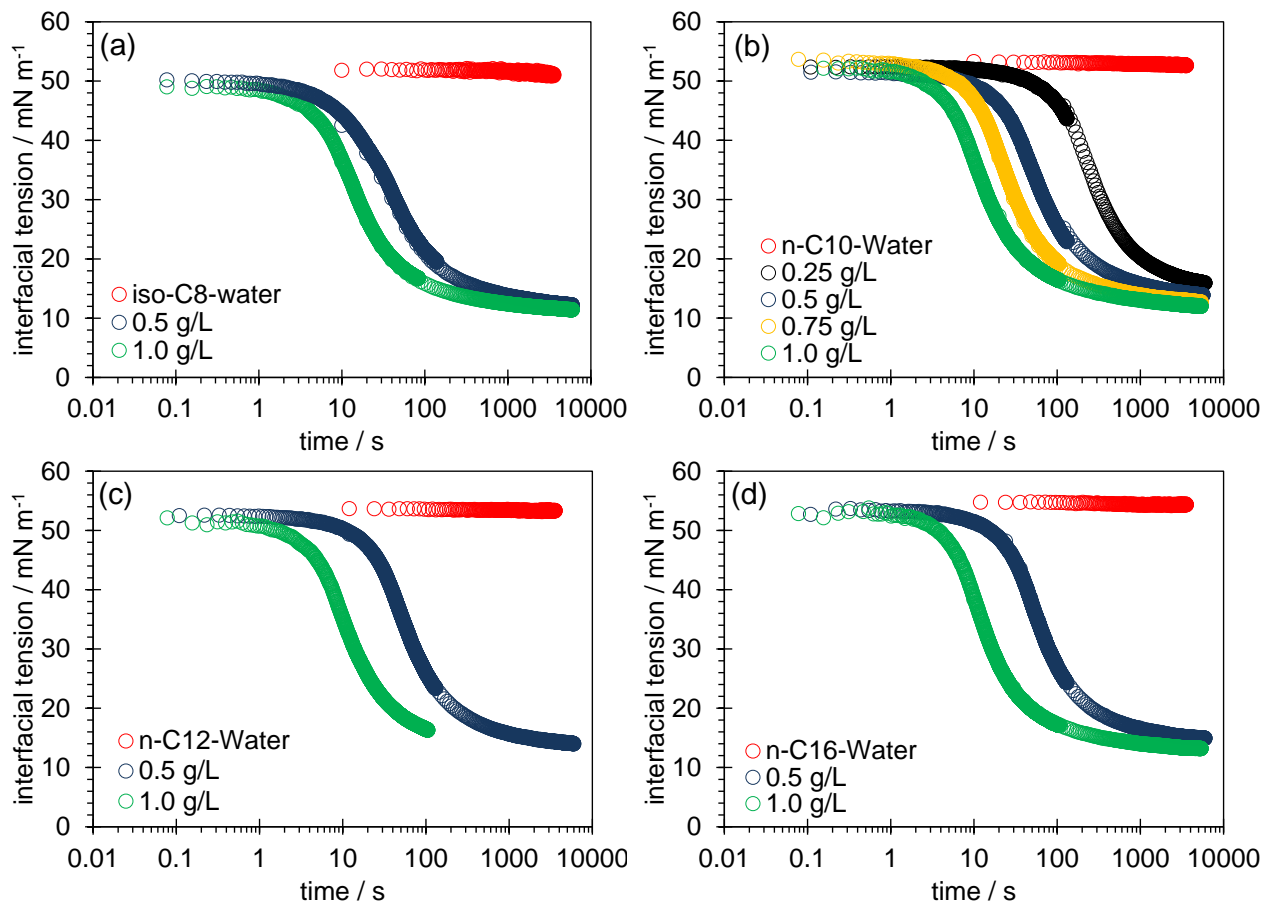
Figure 5.1: Interfacial tension (IFT) measurements of (a) iso-octane- (iso-C8-), (b) n-decane- (n-C10-), (c) n-dodecane- (n-C12-), and (d) n-hexadecane- (n-C16-) water interfaces on a log scale plot at various nanoparticle concentrations (all salt-free).

Table 5.1: Steady state IFT and adsorption energy ($|\Delta E|$) computed from independent approaches using Eq. 2.13 and Eq. 2.16 all in the absence of salt.

interface	$|\Delta E|$ [k_BT] (from Eq. 2.13)	$|\Delta E|$ [k_BT] (from slope of Eq. 2.16)	γ_∞ [mN m^{-1}] (from intercept of Eq. 2.19)
iso-C8-water	$(7\pm1)\times10^4$	$(8\pm3)\times10^4$	11 ± 1
n-C10-water	$(7\pm1)\times10^4$	$(6\pm2)\times10^4$	12 ± 1
n-C12-water	$(7\pm1)\times10^4$	$(7\pm2)\times10^4$	12.70 ± 0.02
n-C16-water	$(7\pm1)\times10^4$	$(7\pm3)\times10^4$	13 ± 1

presence of nanoparticles, the steady-state interfacial tensions (γ_∞) for these alkane-water systems are obtained from the intercept of extrapolations of late-time IFT measurements against $\sqrt{1/t}$ which are listed in Table 5.1. For n-C10, in particular, the IFT drops from 52.8 ± 0.4 mN m^{-1} for a pristine n-C10-water interface, to a steady-state value of 12 ± 1 mN m^{-1} given sufficient time. The adsorption energy ($|\Delta E|$) for the given alkane-water system at each concentration for EC nanoparticles is computed by analyzing the early stages of adsorption using Eq. 2.16 (see Table 5.3). A factorial statistical analysis on these values shows that EC nanoparticle concentration has no significant effects on $|\Delta E|$ (see Table B.3 in Appendix B). Therefore, values for adsorption energy calculated from dynamic IFT data are averaged for each alkane-water system and reported in Table 5.1. These results compare very well to the values obtained from an alternative approach which makes use of Eq. 2.13. Moreover, in agreement with these findings, $|\Delta E|$ is calculated to be $(7 \pm 2) \times 10^4$ k_BT by Eq. 2.12 from knowledge of contact angle. A contact angle of $89\pm3°$ and $81\pm3°$ was obtained following the direct and reverse dispensing approach, respectively (see Section 3.1.3 for details of these measurements), from which an average value of $85\pm3°$ is obtained. Pair-comparisons of $|\Delta E|$ estimates from different approaches show no significant difference at the 95% confidence level. In all cases considered, the adsorption energy is several orders of magnitude larger than thermal fluctuations ($\sim k_BT$) confirming that, as for the air-water interface [16], the adsorption of EC nanoparticles at the alkane-water interfaces studied is irreversible.

5.3   Effects of ionic strength on the adsorption kinetics

The effects of ionic strength at a constant EC nanoparticle concentration of 0.2 g L^{-1}, 0.5 g L^{-1}, and 0.8 g L^{-1} on the DST of air-water interface are shown in Figures 5.2(a), (b),

and (c), respectively. For comparison, Figure 5.2(d) shows the effect of EC nanoparticle concentration at a constant ionic strength (0.05 M) on the DST. In each case, the surface tension decreases from a value of 72.3±0.23 mN m^{-1}, corresponding to the surface tension of the pristine air-water interface [177], to a steady-state value of 39.8±0.44 mN m^{-1} (obtained from the intercept of Eq. 2.19), regardless of nanoparticle concentration or ionic strength.
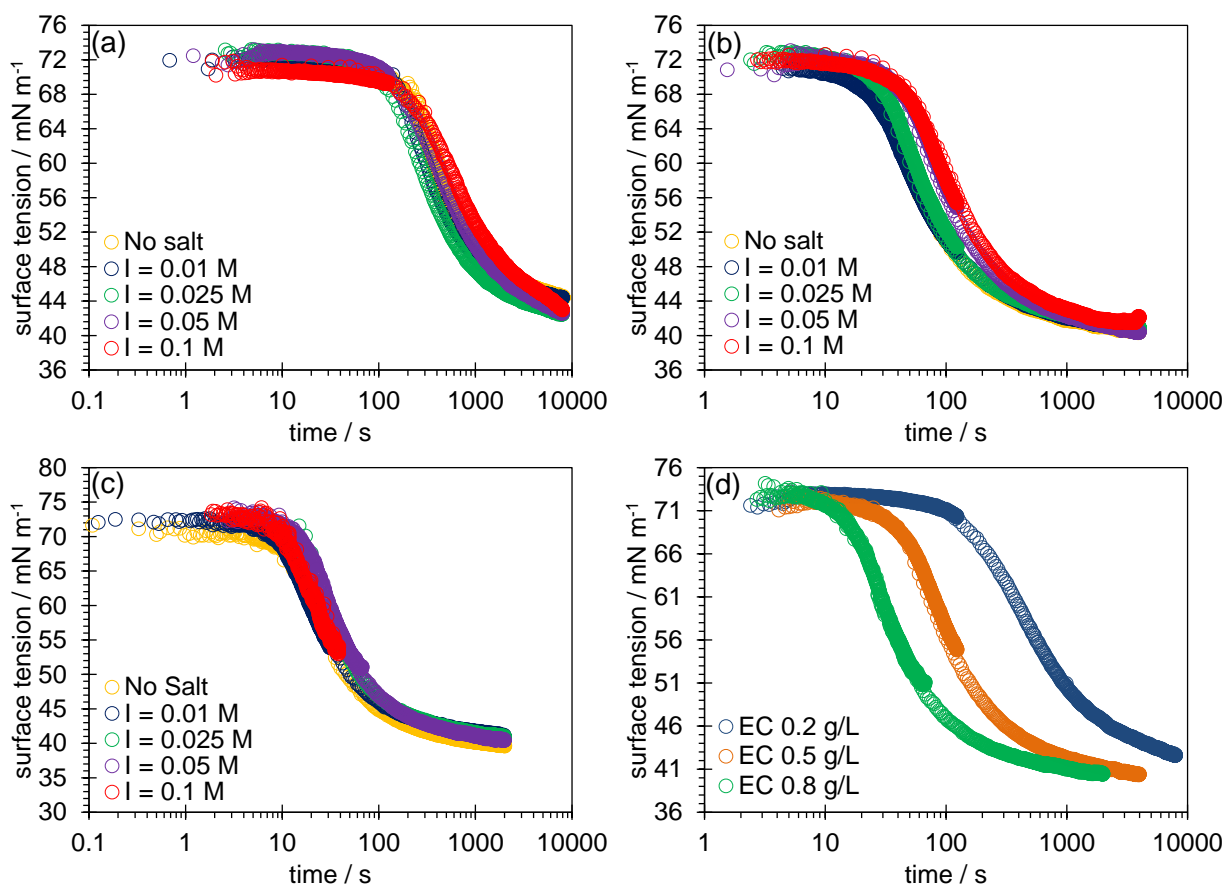
Figure 5.2: Dynamic surface tension (DST) measurements of colloidal suspensions of EC nanoparticles at constant concentration of EC nanoparticle of (a) 0.2 g L^{-1}, (b) 0.5 g L^{-1}, and (c) 0.8 g L^{-1} and various ionic. (d) DST measurements of colloidal suspensions of EC nanoparticles at a constant ionic strength (0.05 M). Reprinted with permission from [15], Copyright© 2015 American Chemical Society.

$|\Delta E|$ is computed at each level of EC nanoparticle concentration and ionic strength by

fitting the early-time DST data to Eq. 2.16, as explained earlier. The results are plotted in Figure 5.3. In this approach, it is assumed that the particle size and bulk concentration remained constant during the early-stages of adsorption (< 60 s), irrespective of EC concentration and ionic strength (see Section C.2 in Appendix C where the coagulation rate is compared with the adsorption rate). These results are quantitatively in agreement with the expectations from Eq. 2.12 where no significant effect of ionic strength on contact angle is observed from contact angle measurements at different ionic strengths (Table B.2 in Appendix B). The data shown in Figure 5.3 are analyzed in terms of a 3×5 factorial design and associated ANOVA table (see Table B.4 in Appendix B) assuming that a linear regression model is adequate. Each level of EC nanoparticle concentration is considered as
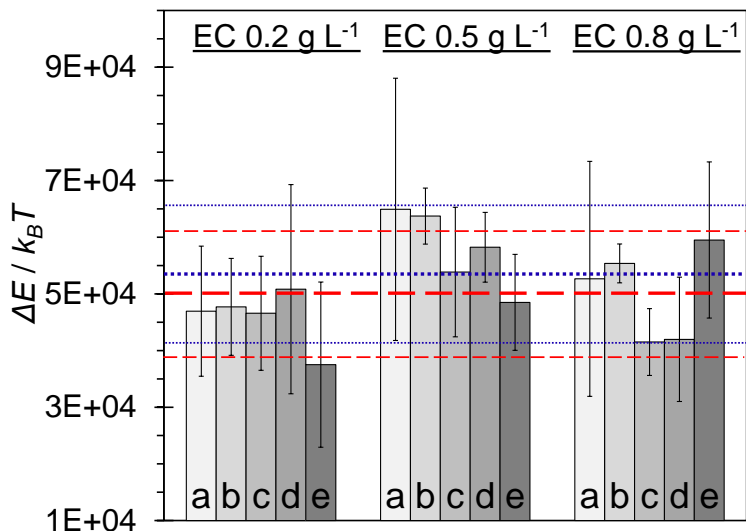
Figure 5.3: $|\Delta E|$ calculated from DST measurements at three levels of EC nanoparticle concentrations and at ionic strengths of (a) 0 M, (b) 0.01 M, (c) 0.025 M, (d) 0.05 M, and (e) 0.1 M. The dashed and dotted lines represent $|\Delta E|$ calculated from Eq. 2.12 and Eq. 2.13, respectively, with 95% confidence interval. Reprinted with permission from [15], Copyright© 2015 American Chemical Society.

a block in the factorial design and, with 95% confidence, it is shown that ionic strength has no significant effect on the adsorption energy values. For further quantitative analysis, the difference in $|\Delta E|$ between any two levels of ionic strength is found to be significant with 95% confidence if it exceeds $1.41 \times 10^4 k_B T$ (i.e., the least significant difference, LSD; see Table B.4 in Appendix B). Comparing the $|\Delta E|$ pairs reported in Figure 5.3 within each block (i.e., at each level of EC concentration), one finds that only 4 out of 30 possible pair

Table 5.2: γ_∞ (top value)[†] and the slope of late-time DST, $(d\gamma/dt^{-0.5})|_{t\to\infty}$, (bottom value)[‡] computed from Eq. 2.19 for different levels of EC nanoparticle concentration and ionic strength. Reprinted with permission from [15], Copyright© 2015 American Chemical Society.

ionic strength [M]	EC nanoparticle concentration [g L^{-1}]		
	0.2	0.5	0.8
0	41.44±1.15	38.93±1.1	38.31±0.25
	262±51	93±12	60±7
0.01	41.46±1.55	39.00±0.19	39.90±0.10
	246±68	97±12	56±21
0.025	39.78±1.40	39.57±1.24	39.50±1.38
	238±52	88±16	65±21
0.05	38.66±1.55	38.39±2.22	38.85±3.62
	354±192	125±67	70±6
0.1	38.21±1.95	38.57±1.92	−
	456±168	142±43	−

[†] with the unit of mN m^{-1}
[‡] with the unit of mN m^{-1} s$^{0.5}$

comparisons exceed the LSD. This shows again that the presence of salt has no significant effect on the adsorption energy for EC nanoparticles at the air-water interface. Early-time dynamics of surface tension reduction are entirely consistent with adsorption of single EC nanoparticles with an average radius of 43.96±4.92 nm for any amount of salt.

The effect of ionic strength on the later stages of EC nanoparticle adsorption at the air-water interface is also investigated using Eq. 2.19. The intercept, representing steady-state surface tension (γ_∞), and the slope of linear plots of surface tension against $t^{-0.5}$ at each level of EC nanoparticle concentration and ionic strength are computed and listed in Table 5.2. With 95% confidence, one finds no difference in the steady-state surface tension obtained at different levels of EC nanoparticle concentration or ionic strength, such that the estimates of γ_∞ may be pooled into an overall average of 39.8±0.44 mN m^{-1}. With this value for γ_∞, $|\Delta E|$ may be estimated also from Eq. 2.13 to be $(5.36\pm1.2)\times10^4 k_B T$, which compares very well with the previous estimates of γ_∞ reported in Figure 5.3.

Turning our attention to the rate of approach to steady state, one finds that irrespective of EC nanoparticle concentration there is no variation in the slope $(d\gamma/dt^{-0.5})|_{t\to\infty}$ (see Table B.5 and Figure B.1 in Appendix B) with ionic strength for values of the latter below

65

the CCC. This means that the rate constant for adsorption (k_a) of nanoparticles from stable colloidal suspensions is independent of the amount of salt. In the context of the model put forward [16], k_a is determined exclusively by the interaction of particles with the pristine interface and is not influenced by blocking of the interface by the already adsorbed particles − the latter being accounted for in terms of a blocking function. That k_a is the same, means that the adsorption is barrierless also in the presence of salt at concentrations below the CCC and, therefore, one expects $k_a \cong \sqrt{D/\pi t}\big|_{t=\tau}$ [16], where τ is of the order of a few seconds. This expectation is indeed verified since $k_a \sim O(10^{-6})$ m s^{-1} [16].

Similar to the air-water interface, analysis of the late stage of EC nanoparticle adsorption at alkane-water interfaces using Eq. 2.19, shows that in the absence of salt a linear trend ($R^2 = 0.99$) between $\left(d\gamma/dt^{-0.5}\right)\big|_{t\to\infty}$ (listed in Table 5.3) and inverse EC nanoparticle concentration. This means that the adsorption constant (k_a), computed from Eq. 2.18, is essentially the same at all the levels of EC nanoparticle concentration with an average value of $(4 \pm 3) \times 10^{-6}$ m s^{-1}. With this value for k_a, one estimates the barrier against adsorption (Φ_b) from $k_a \cong \frac{D}{r}\sqrt{\frac{\Phi_b}{\pi k_B T}}\exp\left(-\frac{\Phi_b}{k_B T}\right)$ to be less than $5k_B T$ (i.e., of the order of thermal fluctuations) reflecting an essentially barrierless adsorption of EC nanoparticles at the alkane-water interfaces [14, 16]. The given relationship between k_a and Φ_b is obtained assuming a parabolic energy distribution [173]. Early-time analysis of IFT measurements, shown in Figure 5.4 for iso-C8-water and n-C10-water, provides estimates of $|\Delta E|$ at different ionic strength which are reported in Table 5.3. These estimates reveal no significant impact of the ionic strength on the adsorption energy (see Table B.3 in Appendix B).

The conclusion is reached that, similar to the air-water interface [16], the adsorption of EC nanoparticles at the alkane-water interfaces is not controlled by the diffusion of nanoparticles from the bulk to interface at the late stages of adsorption, but instead, is kinetically limited by surface blocking, that is by a steric barrier due to the presence of already adsorbed nanoparticles. This slowing down of the adsorption process is however reduced (i.e., a larger adsorption flux is observed) when salt is added to the EC nanoparticle suspension. This is surmised from the decrease in $\left(d\gamma/dt^{-0.5}\right)\big|_{t\to\infty}$. For salt concentrations below 0.05 M, the critical coagulation concentration (CCC), one finds *ca.* 30% reduction in $\left(d\gamma/dt^{-0.5}\right)\big|_{t\to\infty}$ from its value in the absence of salt. Given that the adsorption flux is depended on the adsorption constant and blocking function, two possibly concurrent scenarios may explain the observed increase of the adsorption flux. In one scenario, the addition of salt reduces the small barrier to adsorption of EC nanoparticles causing a modest increase of the adsorption constant. In this scenario, the value of $(10 \pm 5) \times 10^{-6}$ m s^{-1} is computed for k_a following the approach explained earlier (see Section 2.3.3 and Eqs.

Table 5.3: $|\Delta E|$ (top value) computed from dynamic IFT data analysis using Eq. 2.16 and slope[‡] of late-time IFT data (bottom value), $\left(d\gamma/dt^{-0.5}\right)|_{t\to\infty}$, obtained from Eq. 2.19 for alkane-water interfaces.

ionic strength [M]	EC nanoparticle concentration [g L^{-1}]	iso-C8-water	n-C10-water	n-C12-water	n-C16-water
	0.25	–	6±1	–	–
			226±14		
	0.5	8±3	6±1	7±2	6.6±0.7
		85±21	98±12	97±1	85±8
0	0.75	–	6±2	–	–
			63±6		
	1.0	7±1	7±2	–	7±3
		51±5	57±10		47±21
0.01		10±2	8±3	–	–
		62±11	83±5		
0.025		9±2	7±3	–	–
		54±4	56.5±0.5		
0.05	0.5	10±4	8±3	–	–
		54±5	107±7		
0.1		8.9±0.5	6±2	–	–
		61±2	84±11		
0.2		8±1	–	–	–
		54±12			

† with the unit of $\times 10^{-4} k_B T$

‡ with the unit of mN m^{-1} s$^{0.5}$

Alternatively, irrespective of ionic strength and EC nanoparticle concentration, $|\Delta E|$ is found to be $(7 \pm 1) \times 10^4 k_B T$ from Eq. 2.13 for all the alkane-water systems studied here.
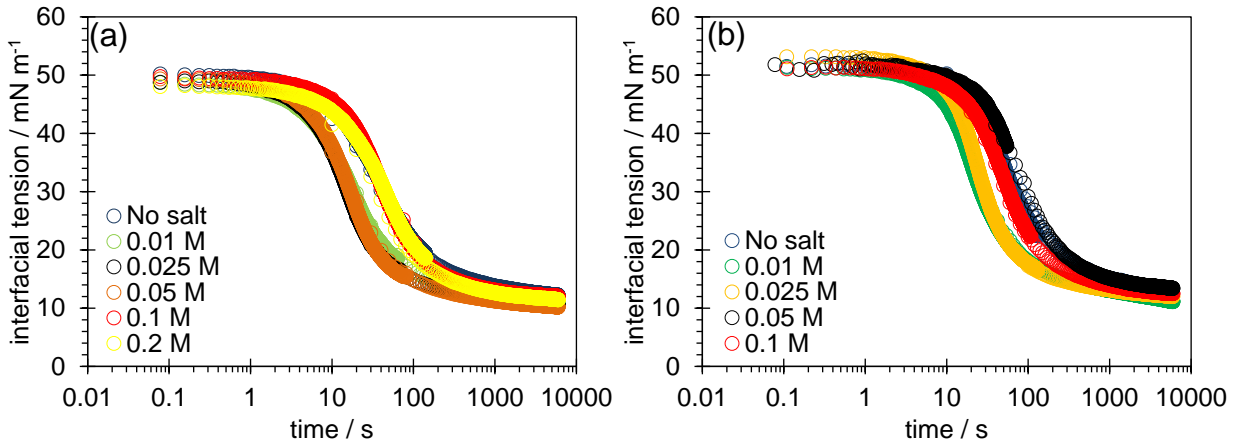
Figure 5.4: IFT measurements at different ionic strength for (a) iso-C8-water and (b) n-C10-water interfaces.

2.18 and 2.19) and assuming the same blocking function. Note that although a larger k_a is estimated, this estimate is not statistically different from the one obtained in the absence of salt (i.e., $(4 \pm 3) \times 10^{-6}$ m s^{-1}). For this greater value of k_a one finds the barrier against adsorption to be practically zero ($< 0.1 k_B T$) reflecting a completely barrierless adsorption of EC nanoparticles at the alkane-water interfaces.

In the other scenario, the blocking function is modified (reduced) by to the addition of salt. Following this scenario, the exponent m in the expression of the blocking function, $B(\Theta) \cong 2.32 \left(1 - \Theta/\Theta_\infty\right)^m$ is permitted to change. Recall that the blocking function, which accounts for the effect of already adsorbed nanoparticles on the nanoparticle adsorption, admits the value of $m = 3$ [2] for hard, non-interacting spheres according to the RSA model. Setting $m = 2.5$ in the presence of salt below the CCC explains the observed reduction of $\left(d\gamma/dt^{-0.5}\right)|_{t \to \infty}$ for the alkane-water interfaces. Note that an increase of the rate of nanoparticle adsorption from suspensions with ionic strengths below the CCC was not observed for the air-water interface − a fact which should be reconciled with the hypotheses described above. In any case, more sensitive measurements and alternative models are needed to completely elucidate the effect of ionic strength on the late-time dynamics of nanoparticle adsorption at different fluid interfaces.

Above the CCC, especially in concentrated suspensions, nanoparticle aggregation competes with attachment at the interface during the intermediate and late stages of adsorption − adding to the complexity of DST data interpretation. Similar to the air-water system, above the CCC, $\left(d\gamma/dt^{-0.5}\right)|_{t \to \infty}$ increases for iso-C8-water and n-C10-water systems (see

Table 5.3), which is due to a reduction in the nanoparticle flux to the interface. Two different scenarios may be considered. In scenario I, both individual nanoparticles and nanoparticle aggregates are assumed to adsorb at the interface, whereas in scenario II only individual nanoparticles adsorb. These possibilities deserve careful examination since it has been suggested that attachment of EC nanoparticle aggregates at the air-water interface is the reason for the superior stability of foams generated with EC nanoparticles [82]. The likelihood of two aforementioned scenarios are assessed in the following section by estimating the interface coverage from experiments as well as from theoretical considerations.

5.4   Interface coverage

As mentioned briefly in the previous section, two scenarios are identified to explain the adsorption and assembly of EC nanoparticles at fluid interfaces. These two scenarios are sketched in Figure 5.5. It is assumed in scenario I that individual nanoparticles as well
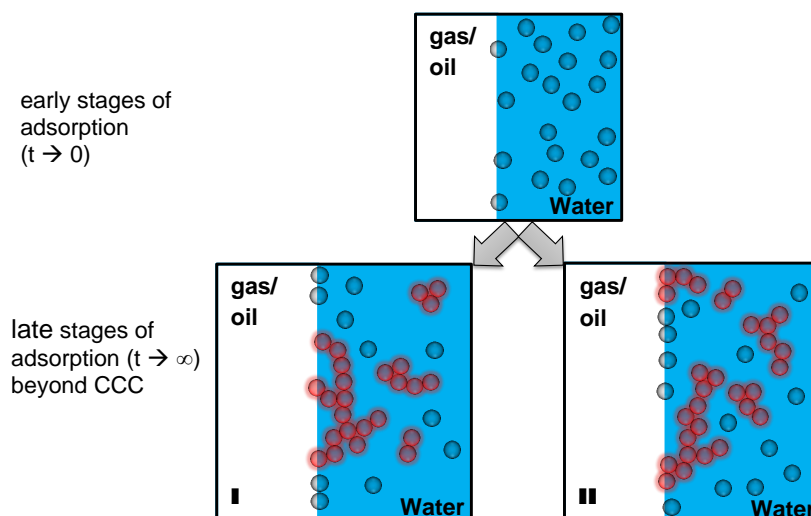
Figure 5.5: Two possible scenarios for the adsorption of EC nanoparticles at an interface (nanoparticle aggregates are shown in red color). Scenario I: nanoparticle aggregates formed in the bulk are adsorbed at the air-water interface alongside single nanoparticles. Scenario II: only single nanoparticles are adsorbed at the air-water interface; nanoparticle aggregates at the interface are formed by the attachment on nanoparticles on already adsorbed ones. Reprinted with permission from [15], Copyright© 2015 American Chemical Society.

as aggregated nanoparticles adsorb at the interface, whereas in scenario II only individual (non-aggregated) nanoparticles adsorb. Because aggregates formed in the DLA regime are not compact, one expects $\Theta_\infty|_{>CCC} < \Theta_\infty|_{<CCC}$ if scenario I is correct (Θ_∞ is the coverage of the interface at steady state). To estimate Θ_∞ in terms of the most readily accessible parameters, $|\Delta E|$ is eliminated between Eq. 2.12 and Eq. 2.13 to obtain

$$\Theta_\infty = \left(\frac{\gamma_0 - \gamma_\infty}{\gamma_0} \right) \frac{1}{(1 \pm \cos\theta)^2} \tag{5.1}$$

where γ_∞, γ_0, and θ are known for each set of experimental conditions (EC concentration and ionic strength). The various estimates of Θ_∞ for air-water interface at different ionic strength are shown in Figure 5.6 alongside error estimates. Reduced particle-particle
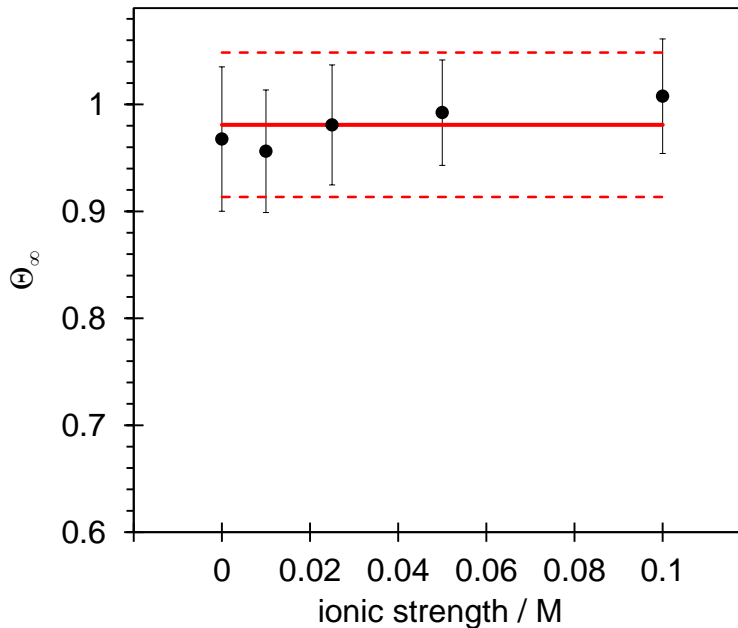
Figure 5.6: Estimates of Θ_∞ at different levels of ionic strength are consistent with hexagonal close packing of EC nanoparticles at the air-water interface. Reprinted with permission from [15], Copyright© 2015 American Chemical Society.

repulsion with increasing ionic strength should, in principle, enable closer packing of the particles at the interface [9] − a thought which will be assessed in detail later in this thesis. Statistical analysis, however, confirms that the different estimates are not significantly different from one another and may, therefore, be pooled into an average $\Theta_\infty = 0.981 \pm 0.067$.

Furthermore, the null hypothesis that $\Theta_\infty = 0.91$, is not rejected at the 95% confidence level. Recall that $\Theta_\infty = 0.91$ corresponds to hexagonal close packing of particles. It is thus concluded that scenario I is not supported by the experimental data, although adsorption of EC nanoparticle aggregates may still happen. In any case, nanoparticle coagulation concurrent with attachment at the interface should be expected to slow down the apparent rate of adsorption by hindering the process during its later stages. A reduction of the nanoparticle flux at the air-water interface, which is given by $j|_{x\to 0^+} = k_a N_b B(\Theta)$ [16], may be expected for the following two reasons. Firstly, EC nanoparticle aggregates act as sinks for single nanoparticles, thereby decreasing the bulk concentration of adsorbing species, N_b [134]. Secondly, as discussed earlier in Section 5.3 for alkane-water interfaces, attachment of single nanoparticles and nanoparticle aggregates onto already adsorbed nanoparticles exacerbates blocking for a given value of surface coverage. The data shown in Table 5.2 do not contradict this expectation, since significantly larger values of $(d\gamma/dt^{-0.5})|_{t\to\infty}$ measured above CCC (see Table S5 in Appendix B) correspond to slowing down of the approach to steady state.

As for the air-water interface, the steady-state coverage of n-C10-water interface is calculated at different ionic strength from experimental data using Eq 5.1 and the results are plotted in Figure 5.7. A tight hexagonal packing of EC nanoparticles at the n-C10-water interface is consistent with the experimentally deduced values of Θ_∞. As mentioned before, the steady-state interface coverage is the result of net interactions between colloidal nanoparticles adsorbed at the interface. According to the extended- Derjaguin, Landau, Verwey, and Overbeek (DLVO) theory, for a given colloidal domain, the net interactions is the summation of attractive and repulsive forces. For the EC colloidal systems studied in this work, these include van der Waals (Φ_{vdW}) and hydrophobic (Φ_H) attraction and electrostatic (Φ_{elec}) and dipole-dipole (Φ_{d-d}) repulsion. Monopolar attractive capillary force has a negligible contribution in this study due to a very small Bond number ($O(10^{-10})$, see Appendix C.1). Contact angle (θ) controls the fraction of nanoparticle at the interface exposed to oil and the fraction exposed to water. Considering interactions only through same phase, the equations reported in Table 2.1 are used to compute some of the aforementioned interactions as a function of contact angle. For the missing equations, Derjaguin approximation for the interactions of EC nanoparticles at the interface is used (see Appendix A for the derivations). Attractive van der Waals and hydrophobic as well as electrostatic repulsive interactions between two EC nanoparticles with a similar radius (r) separated by h (surface-to-surface) are given below (superscripts O and W refer to oil and water, respectively).

$$\Phi_{vdW}^O = -r\theta \frac{H_{121}}{12\pi h} \tag{5.2}$$
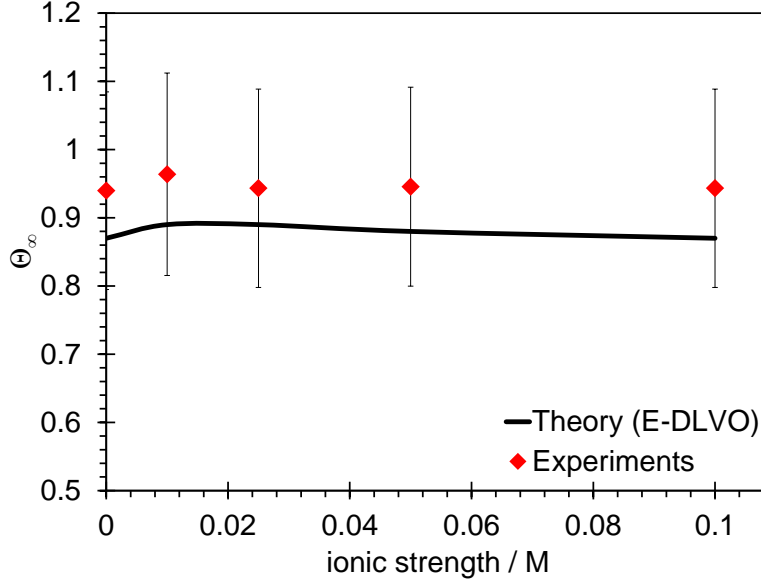
Figure 5.7: Ultimate coverage of n-C10-water interface calculated experimentally and theoretically at different ionic strength.

$$\Phi_{vdW}^{W} = -r(\pi - \theta)\frac{H_{131}}{12\pi h} \tag{5.3}$$

$$\Phi_{H}^{W} = -r(\pi - \theta)\frac{K_{131}}{2\pi h} \tag{5.4}$$

$$\Phi_{elec}^{W} = 4(\pi - \theta)\epsilon_0\epsilon_w r\Psi_{pw}^2\left(1 - \frac{r}{h+2r}\right)\ln\left[1 + \frac{\exp(-\kappa h)}{1 + h/r}\right] \tag{5.5}$$

Detailed calculations of required parameters in equations in Table 2.1 and Eqs. A.9 to A.12, with the assumption of negligible effect for Brownian motion on the EC nanoparticles adsorbed at alkane-water interfaces, are reported in Section C.3 in Appendix C. Table 5.4 summarizes these values that are used for extended-DLVO calculations for the adsorbed EC nanoparticles at the n-C10-decane interface. Surface dipole moment density (σ_d) varies with respect to the average dipole moment of one polar group (p) and surface density of that polar group at the surface of particle exposed to oil (σ) as $\sigma_d = p\sigma$. Due to lack of information on the latter for EC, a conservative estimate of 5 nm^{-2} for σ is made for EC nanoparticles from values reported in literature for other systems [72].

The net interaction energy among EC nanoparticles adsorbed at the n-C10-water interface is computed from $\Phi_{total} = \left(\Phi_{vdW}^{O} + \Phi_{vdW}^{W} + \Phi_{H}^{W}\right) + \left(\Phi_{elec}^{O} + \Phi_{elec}^{W} + \Phi_{d-d}^{O} + \Phi_{d-d}^{W}\right)$, where

Table 5.4: Parameters used in Equations in Table 2.1 and Eqs. A.9 to A.12 for extended-DLVO calculations.

r : nanoparticle radius	44.5 nm
θ : EC nanoparticle contact angle measured through water	85°
H_{121} : Hamaker constant (EC-C10-EC)	10^{-21} J [80]
H_{131} : Hamaker constant (EC-water-EC)	10^{-20} J [6]
K_{131} : hydrophobic constant (EC-water-EC)	8.7×10^{-23} J [16]
A_{po} : surface area of nanoparticle exposed to C10$-A_{po} = 2\pi r^2(1 - \cos\theta)$	1.1×10^{-14} m^2
A_{pw} : surface area of nanoparticle exposed to water$-A_{pw} = 2\pi r^2(1 + \cos\theta)$	1.4×10^{-14} m^2
Ψ_{pw} : particle surface charge (ζ-potential)	-59.07 mV
ε_0 : vacuum permittivity	8.85×10^{-12} C^2 N^{-1} m^{-2}
ε_o : relative dielectric constant of n-C10	2 [186]
ε_w : relative dielectric constant of water	78.5 [110]
σ_{po} : particle surface charge density exposed to oil$-\sigma_{po} = \Psi_{pw}\varepsilon_0\varepsilon_o/r$	-2.32×10^{-5} C m^{-2}
σ_{pw} : particle surface charge density exposed to water	varies with κ
σ_d : surface dipole moment density	2.3×10^{-11} C m^{-1}

the first term in brackets includes the attractive interactions and the second the repulsive ones. At different ionic strengths the interactions are computed and the results are plotted in Figure 5.9. At all levels of ionic strength a net repulsive force is experienced among the adsorbed EC nanoparticles at the interface. As explained earlier, in the presence of net repulsion the EC nanoparticles adsorbed at the interface assume a hexagonal pattern [143]. The peak repulsion is found a few nanometers away from the surface of an EC nanoparticle. Knowing the distances where the peaks are observed on the interaction energy profiles on Figure 5.9, one can estimate the theoretical Θ_∞^{theory} from (assuming hexagonal coverage of the interface)

$$\Theta_\infty^{theory} = \frac{\text{occupied area}}{\text{total hexagonal area}} = \frac{3\pi d^2}{6\sqrt{3}(d + h)^2} \tag{5.6}$$

The theoretical values for ultimate interfacial coverage are shown in Figure 5.7. Figure 5.9 clearly shows a significant reduction in the repulsion among EC nanoparticles at the interface when salt is added to the aqueous phase. It was discussed earlier that the adsorption flux increases with the addition of salt below the CCC (*viz.* smaller $\left(d\gamma/dt^{-0.5}\right)|_{t\to\infty}$) and this was hypothesized to be the result of less efficient blocking. This is indeed consistent with the computations summarized in Figure 5.9, since a reduction in the net repulsion is
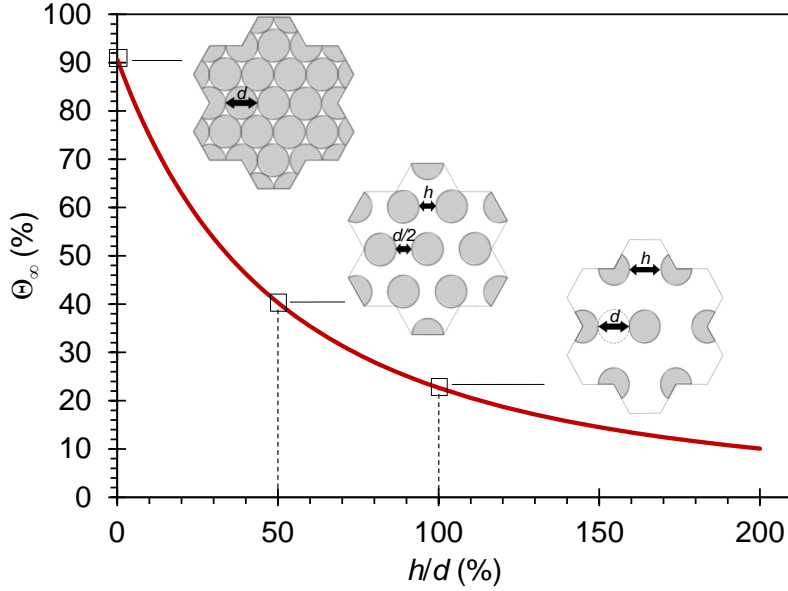
Figure 5.8: Θ_∞^{theory} calculated from Eq. 5.6 and corresponding interface configurations at certain Θ_∞^{theory} values.

expected to lead to more efficient rearrangement of nanoparticles at the interface. Figure 5.9 shows that in the presence of salt, EC nanoparticles at the interface experience weaker repulsion with a shorter effective range. Therefore, during the late stages of the adsorption process, the adsorption flux of nanoparticle adsorption is enhanced in the presence of salt and is maximum at an ionic strength just below CCC. From both experiment and theory, one finds a tight packing of the interface regardless of ionic strength. A slight improvement on the coverage observed in the experiments and expected from theory, is not significant considering the magnitude of experimental error. It must be noted that capillary quadrupolar attraction arising from pinning and distortion of the three-phase contact line [163] is not taken into account in the extended-DLVO computations shown in Figure 5.9. The amplitude of contact line undulation is thought to depend on the extent of contact angle hysteresis. Contact line undulations with amplitude not exceeding 1 nm result in quadrupolar capillary attraction that is not strong enough to cause coagulation of adsorbed nanoparticles, even in the presence of salt (see Figure 5.10(a)). More significant distortions of the contact line, however, would result in net attraction between adsorbed nanoparticles at all distances in the presence of salt (see Figure 5.10(b)). The latter picture is not consistent with the experimental observation of dense coverage of the alkane-water interface
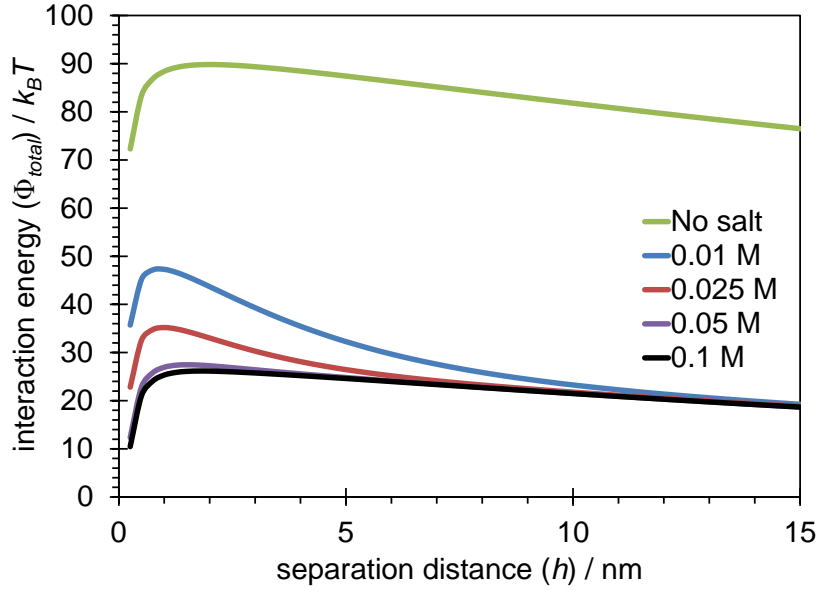
Figure 5.9: Extended-DLVO calculations for adsorbed EC nanoparticles at n-C10-water interface at different ionic strengths.

with nanoparticles. For capillary quadrupolar attraction calculations see Appendix A.

Contrary to the n-C10-water interface, it is shown that salt has no significant effect on $\left(d\gamma/dt^{-0.5}\right)|_{t\to\infty}$ for the air-water interface at any level of ionic strength. In principle, theoretical calculations similar to the ones shown in Figure 5.9 would be conducted for the air-water interface to understand the extent to which repulsion among EC nanoparticles adsorbed at the air-water interface is modified by the addition of salt to the aqueous phase. These calculations, however, are subject to a significant uncertainty in computing the dipole-dipole interaction (Φ_{d-d}^A) through air. The key parameter in calculating Φ_{d-d}^A is the dipole moment (μ) which is a medium dependent parameter [103, 120, 188]. Any changes in μ can have a large effect on Φ_{d-d}^A. Due to the lack of information for μ a reliable estimate for Φ_{d-d}^A could not be made here.
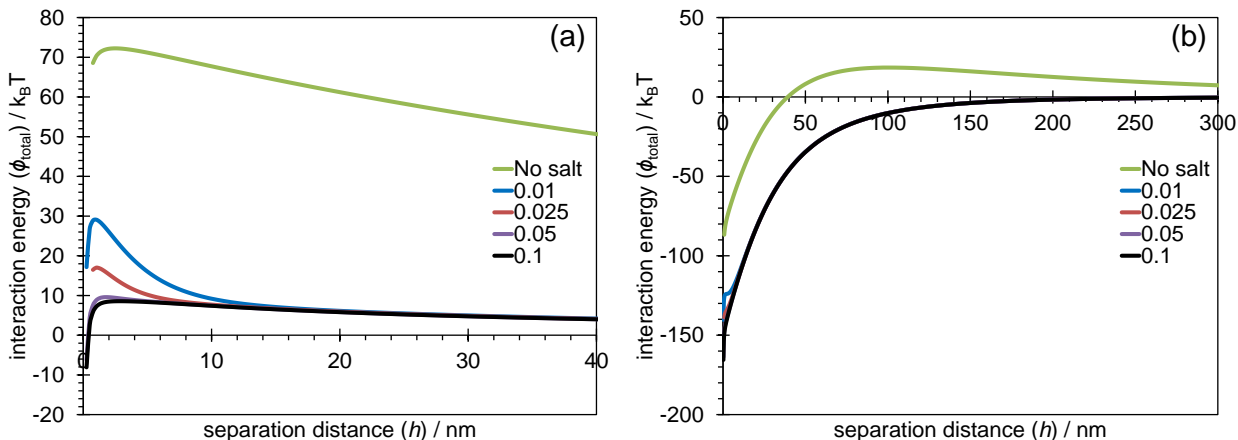
Figure 5.10: Extended-DLVO calculations for adsorbed EC nanoparticles at n-C10-water interface considering quadrupolar capillary attraction with undulations of (a) 1 nm and (b) 3 nm.

5.5 Insights into foam and emulsion stabilization by EC nanoparticles

The discussions in Sections 5.2 to 5.4 shed light on the mechanism by which EC nanoparticles are able to stabilize aqueous foams or Pickering emulsions. In particular, good foamability and extreme foam stability have been found at conditions leading to destabilized suspensions of EC nanoparticles, that is for pH<4 and/or moderate or high ionic strengths (>20 mM) [82]. Contrary to the assertion of Jin et al. [82], adsorption of nanoparticles at the air-water interface is not limited by electrostatic repulsion and takes place at all ionic strengths. Adsorption, however, is a necessary but not sufficient condition for obtaining stable EC nanoparticle foams. Instability of the suspension and nanoparticle aggregation, leading to the formation of bridges resisting the approach of air-water interfaces in thinning lamellae, and ultimately to the formation of intervening porous structures seems to be also needed (see Figure 5.11), as also suggested elsewhere [73]. Particle adsorption, colloidal instability and coagulation, bridge formation and drainage of the continuous liquid phase between approaching interfaces are coupled processes dependent on a number of factors, including particle size and concentration, as well as particle and fluid physicochemical properties. A generally applicable model to predict emulsion or foam stability from the interplay among these processes will require additional research, some of which

is the subject of the next chapter.
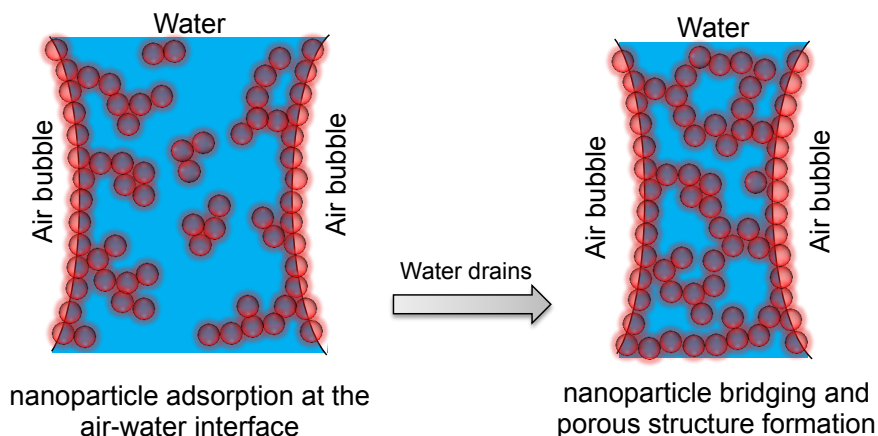
Figure 5.11: The formation of porous structure due to nanoparticle bridging during the course of water drainage from aqueous foams. Reprinted with permission from [15], Copyright© 2015 American Chemical Society.

5.6   Summary

The extended-DLVO theory predicts barrier-less irreversible adsorption of EC nanoparticles at the air-water and alkane-water interfaces at neutral pH and any level of ionic strength in the range of 0 M to 0.1 M. The adsorption energy, contact angle, and steady state surface tension which characterize the assembly of EC nanoparticles at fluid interfaces are shown to be insensitive to the ionic strength. The dynamics of self-assembly of EC nanoparticles at fluid interfaces are dominated by the adsorption of single nanoparticles, even under conditions of nanoparticle aggregation in the bulk. Experimentally (dynamic surface/interfacial measurements) and theoretically (extended-DLVO), it is found that the fluid interfaces are tightly covered by EC nanoparticles at the maximal limit (91%) corresponding to a hexagonal pattern. Adsorption of colloidal EC nanoparticles at the air-water and alkane-water interfaces is a necessary condition to generate and stabilize foams and Pickering emulsions, respectively. Unlike the air-water system, a faster adsorption seems to be happening when the ionic strength is kept below the critical coagulation concentration

for EC nanoparticles in alkane-water systems. These findings have significant implications for the fundamental understanding of colloidal systems and the practical application of design and engineer foams and emulsions using colloidal EC nanoparticles in various environmental conditions.

Chapter 6

Pickering Emulsions Stabilized by Ethyl Cellulose Nanoparticles

6.1   Introduction

Spherical EC nanoparticles have been successfully used to generate aqueous foams with a remarkable stability [82]. In this chapter, EC nanoparticles, which are well characterized in Chapters 4 and 5, are exclusively used to generate Pickering emulsions at different conditions in the absence of molecular surfactants. The effects of ionic strength, EC nanoparticle concentration, and oil-to-water volume ratio are investigated and the results are compared to theoretical predictions. As discussed in Section 2.4, a Pickering emulsion (or foam) could remain stable due to the action of one of the two mechanisms: steric or bridging (see Figure 2.6). The former happens when the interface is covered nearly to its maximal jamming limit whereas the latter is expected to be effective at low coverage of the interface by nanoparticles The results reported in this chapter, taken together with the earlier findings on the colloidal stability of EC nanoparticles and the kinetics of adsorption to the alkane-water or air-water interfaces, provide new insights into the mechanism behind Pickering emulsion or foam stabilization by EC nanoparticles. DLVO theory is used once again to estimate the theoretical limits for the combination of particle size and contact angle at which bridging becomes potentially an effective mechanism to stabilize a Pickering emulsion. These are essential information to engineer and design Pickering emulsions (or foams) to meet the requirements for a successful application. Moreover, high internal phase Pickering emulsions are successfully used as the template to fabricate polymeric porous materials with a potential application in oil-water separation.

The results presented in this chapter have been published in the following paper:

N. Bizmark and M. A. Ioannidis. Ethyl cellulose nanoparticles at the alkane-water interface and the making of Pickering emulsion. *Submitted to Langmuir.*

N. Bizmark and M. A. Ioannidis. Pickering emulsions stabilized by ethyl cellulose nanoparticles: Mechanism of formation and stability control. *Submitted to Journal of Colloid and Interface Science*

6.2 Pickering emulsion generation with EC nanoparticles

6.2.1 Recognizing the emulsifier

Mechanical mixing was used to generate and stabilize Pickering emulsions made with n-C10 and aqueous suspension of EC nanoparticles with a volume fraction of $f_{oil} \equiv V_{oil}/V_{total}$, where $V_{total} = V_{water} + V_{oil}$, at a concentration of 1.0 g L^{-1}, and ionic strength of 0.05 M as shown in Figure 6.1-ii. The emulsion phase rests atop the excess aqueous phase suggesting that it is an oil-in-water (O/W) emulsion, as would be expected [36] from contact angle measurements ($\theta < 90°$, see Chapter 5 and Table 5.4). That oil is the dispersed phase is confirmed by closing an electric circuit traversing through the emulsion. Using such an electric circuit, shown in Figure C.1 in Appendix C, an LED lamp (the indicator) is turned on. This can happen only if water (the only conductive component in the system) is the continuous phase, and hence, the dispersed phase is oil (n-C10). A detailed quantitative analysis on the type of emulsion is conducted by electrical resistivity measurements reported in Section 6.3.1. That the O/W emulsion obtained is stabilized by EC nanoparticles adsorbed at the oil-water interface is verified by attempting to generate an emulsion using four different aqueous phases: (i) deionized water, (ii) aqueous NaCl solution at a concentration of 0.05 M, (iii) EC nanoparticle suspension at 1.0 g L^{-1} with ionic strength of 0.05 M, and (iv) the supernatant solution obtained after coagulation and sedimentation of EC nanoparticles at ionic strength of 0.05 M. As shown in Figure 6.1, a stable emulsion could be successfully generated only in the presence of EC nanoparticles in the aqueous phase.
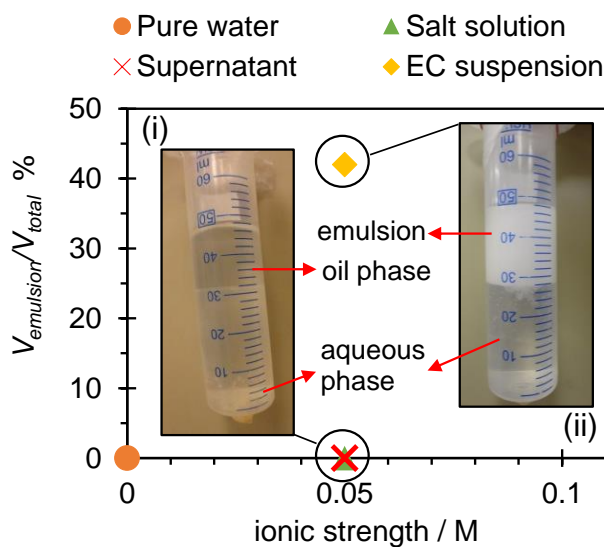
Figure 6.1: Attempts at generating emulsions at $f_{oil} = 0.33$ (i) in the absence and (ii) in the presence of EC nanoparticles. Ionic strength was kept constant at 0.05 M in all the tests except when pure water was used.

6.2.2 Optimum emulsification conditions

Pickering emulsions are generated following the procedure explained in Section 3.2 using a mechanical mixer. In this procedure, mixing time and mixing speed are the parameters that were kept constant during the course of emulsification tests. This was done so as to eliminate any possible effects of the aforementioned mixing parameters on the stability of generated Pickering emulsions. The constant values for mixing time and mixing speed were taken as the smallest experimentally determined values at which the most stable Pickering emulsions were obtained. To this end, at two levels of ionic strength 0.01 M and 0.05 M, a constant $f_{oil} = 0.33$ (i.e., 1-to-2 n-C10-to-water volume ratio) and a mixing speed of 500 rpm, O/W Pickering emulsions were generated by varying mixing time from 30 s to 5 min. As shown in Figure C.2(a) (in Appendix C), at both levels of ionic strength, a more stable Pickering emulsion is obtained if mixing time is increased from 30 s to 3 min, but no significant improvement in emulsion stability was observed beyond 3 min of mixing. Thus, the optimum mixing time is set to be 3 min in all further emulsification tests unless mentioned explicitly. In order to decide on the mixing speed, Pickering emulsions were again generated at the conditions used in previous tests except that mixing speed

was set at two levels − 500 rpm and 1500 rpm. Figure C.2(b) (in Appendix C) compares the volume percentage of Pickering emulsions generated at 500 rpm to those at 1500 rpm. Considering the error associated with the measurements, one finds no significant difference between these two cases for both levels of ionic strength. This suggests that the mixing speed of 500 rpm is adequate to generate a stable emulsion, and thus is selected for all subsequent emulsification tests, unless mentioned otherwise. Under these optimum emulsification conditions, the effects of volume fraction, ionic strength, and EC nanoparticle concentration on the emulsion stability are investigated in the following sections.

6.3   Pickering emulsion characterization

6.3.1   The effects of oil volume fraction

As mentioned very briefly earlier, knowing the contact angle of nanoparticles at an interface, or the so-called particle wettability or hydrophobicity, one can expect to generate either O/W or W/O Pickering emulsions [9, 36]. The contact angle of EC nanoparticles at the n-C10-water interface was found to be $85 \pm 3°$ suggesting the Pickering emulsions generated by EC nanoparticles to be O/W. This expectation was experimentally confirmed when $f_{oil} = 0.33$, see Figure 6.1. A phase inversion from O/W to W/O, however, was observed qualitatively when f_{oil} increased to 0.5, as shown in Figure 6.2(a). This experimental finding is perfectly in line with the theoretical expectation [91] that a phase inversion occurs at $f_{oil} = f_{water} = 0.5$. This behaviour is connected to the effectiveness of dispersing one phase into the other during the course of emulsification. When $f_{oil} < f_{water}$, oil is more effectively dispersed in the aqueous phase resulting in an O/W emulsion but when $f_{oil} > f_{water}$, oil becomes the continuous phase and a W/O emulsion will is favored. For different Pickering emulsions, phase inversion has been experimentally found to happen at a wide range of f_{oil} from 0.2 to 0.65 [12].

The phase inversion is quantitatively confirmed by electrical resistivity measurements following the procedure explained in Section 3.2.1. As discussed earlier, the electrical resistivity of an emulsion is similar to that of the continuous phase. To obtain a baseline, the electrical resistivity of n-C10 and aqueous phase (at the same ionic strength that the emulsion was generated) was measured in the absence of EC nanoparticles. At two different levels of f_{oil} (0.33 and 0.67), the electrical resistivity of each phase is measured and compared to that of the baseline, see Figure 6.2(b). A significant shift in electrical resistivity of Pickering emulsion generated at $f_{oil} = 0.33$ is found from that for $f_{oil} = 0.67$. In agreement with earlier observations, the former suggests that continuous phase to be
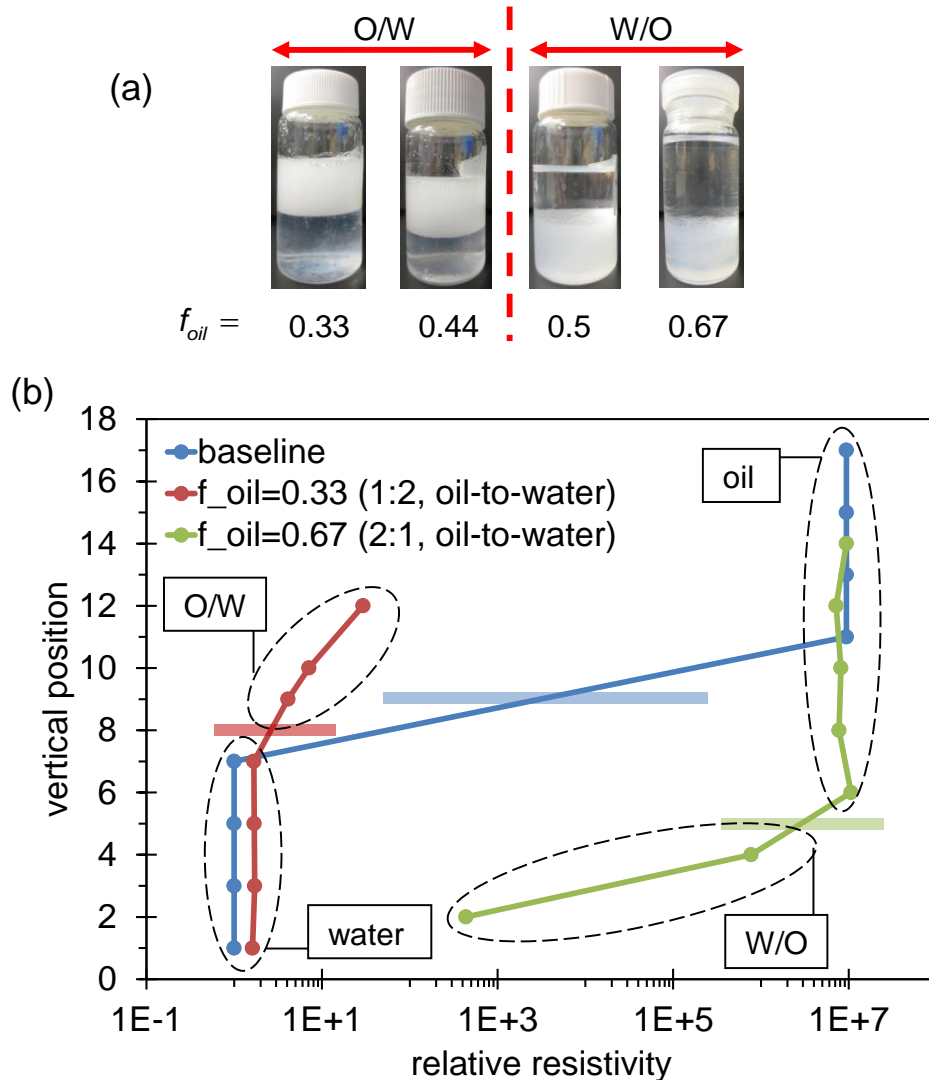
Figure 6.2: (a) Pickering emulsions generated by EC nanoparticles at different oil (n-C10) volume fractions (f_{oil}). A phase inversion is observed when f_{oil} is increased to 0.5. (b) Electrical resistivity measurements for the Pickering emulsions generated at $f_{oil} = 0.33$ or $f_{oil} = 0.67$. The resistivity measurement procedure is explained in Section 3.2.1, see Figure 3.4. The readings are normalized by dividing them by the readings for water and the shaded horizontal bars represent the n-C10-water interface in each case.

water (an O/W emulsion), whereas the latter shows a W/O emulsion where the electrical resistivity is large and closer to that for n-C10.

Changing the volume ratio not only influences the type of Pickering emulsion and drop mean size, but also affects the stability of the generated emulsion. Figure 6.3 shows the volume percentage for Pickering emulsions ($f_{emulsion} = V_{emulsion}/V_{total}$) obtained at various f_{oil} after a day. On this graph, one finds that when $f_{oil} < 0.5$ the entire oil is emulsified
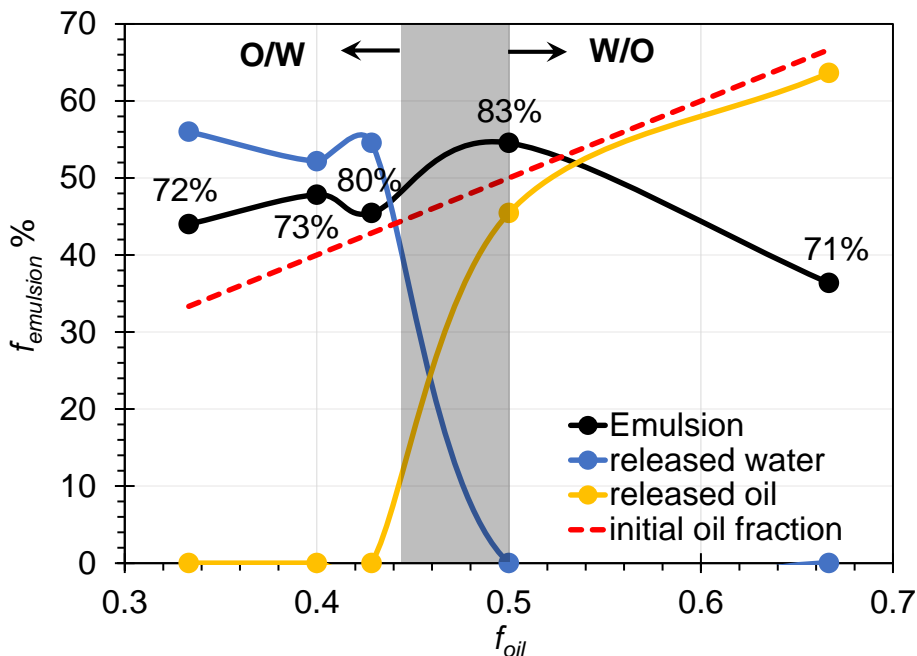
Figure 6.3: Volume percentage obtained for Pickering emulsions ($f_{emulsion}$) obtained at various f_{oil} after a day. Released water or oil refers to the clear water or oil obtained from O/W or W/O emulsions, respectively. Labelled percentages represent estimates of volume fraction for the internal phase in the corresponding generated emulsion.

and no oil is released after a day. The O/W Pickering emulsions were enriched in oil as f_{oil} increased and at $f_{oil} \geq 0.4$, where the dispersed phase occupied at least 74% of the volume of emulsion, high internal phase Pickering emulsions (HIPPEs) were formed. HIPPEs will be used as a template to fabricate porous materials as explained in Section 6.5. However, as shown in in Figure 6.3, for $f_{oil} \geq 0.5$, where phase inversion occurs, the generated W/O emulsions were not as stable as the O/W ones. In this case, only a limited amount of oil was emulsified and the excess oil was released proportional to its initial value.

The O/W emulsions generated with EC nanoparticles at $f_{oil} < 0.5$ can be categorized as Bancroft-type emulsions [58] since the emulsifier (i.e., EC nanoparticles) is dispersed initially in the continuous phase (water). A simple EC mass balance for such Bancroft emulsions can be used to determine the mean volume-surface diameter of the oil drops (D_{32}) as follows [58]

$$D_{32}\big|_{f_{oil}<0.5} = \frac{8r\rho_p\Theta}{\rho_0}\frac{f_{oil}}{1-f_{oil}} \tag{6.1}$$

where ρ_p is the density of EC (i.e., 1.14 g mL^{-1} at 25°C, provided by the manufacturer), ρ_0 is the mass concentration of EC nanoparticles in the bulk (before emulsification), and Θ is the interfacial coverage. It is shown in Section 5.4 that EC nanoparticles fully cover the n-C10-water interface, thus $\Theta = \Theta_\infty = 0.91$. For $f_{oil} \geq 0.5$, the stabilized W/O emulsions can be categorized as anti-Bancroft emulsions since the emulsifier (EC nanoparticles) were initially suspended in the dispersed phase (water). For this type of emulsion, a mass balance for EC nanoparticles is given below [58]

$$D_{32}\big|_{f_{oil}\geq0.5} = \frac{8r\rho_p\Theta}{\rho_0} \tag{6.2}$$

In W/O emulsions (anti-Bancroft), since the emulsifier (EC nanoparticles) is not present in the continuous phase (oil), the size of stabilized drops is independent to the oil fraction as reflected in Eq. 6.2. Hence, for any $f_{oil} \geq 0.5$, the same drop mean size should be obtained at any given EC nanoparticle mass concentration and radius. From knowledge of the relevant parameters: $r = 44$ nm, $\rho_p = 1.14$ g mL^{-1}, $\rho_0 = 1.0$ g L^{-1}, and by varying f_{oil}, theoretical values for D_{32} are calculated for the mean diameter of dispersed phase and plotted in Figure 6.4. The theoretical values compare very well with the experimental results from analysis of microscopic images of the generated emulsions. This confirms intuitively once again that the drops should be covered to their maximum jamming limit (see Section 5.4).
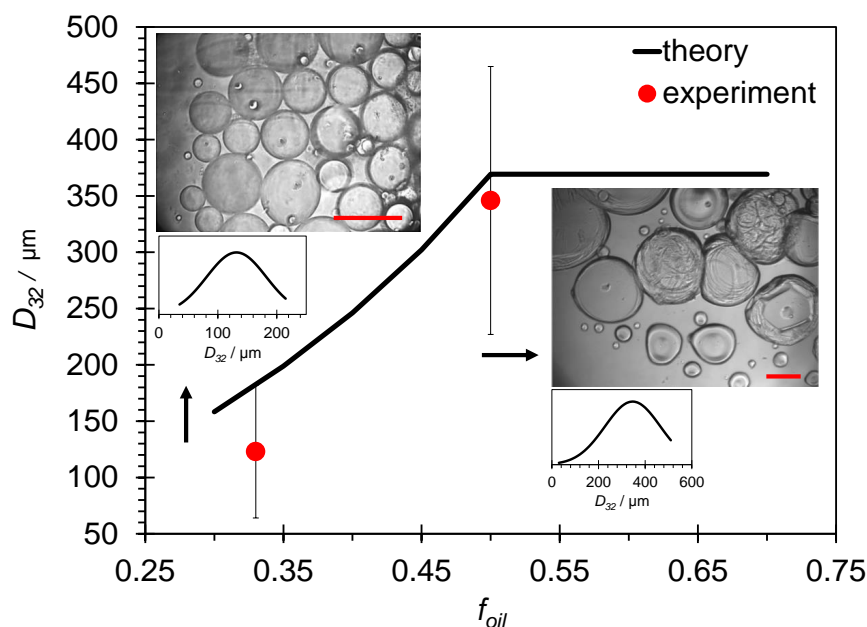
Figure 6.4: Theoretical mean volume-surface diameter (D_{32}) of drops of dispersed phase as a function of f_{oil}. The experimental values for D_{32} are shown for oil and water drops at $f_{oil} = 0.33$ and $f_{oil} = 0.5$, respectively. The scale bar on the microscope images is 200 μm.

6.3.2 The effects of ionic strength

Recalling Section 2.4, Brigg suggested that the addition of a weak flocculating agent is necessary for successful emulsification, but a powerful flocculating agent does not favor Pickering emulsion generation. In the case of colloidal EC nanoparticles, Brigg's statement can be translated as follows: adjusting ionic strength (i.e., flocculating agent) at or below CCC should provide the conditions (i.e., weak flocculating agent) required for generating the most stable Pickering emulsions. Such stable Pickering emulsions with EC nanoparticles are shown and characterized in Section 6.3.1 when the ionic strength was set to be at 0.05 M (i.e., CCC). In connection with the information on the effect of ionic strength on the adsorption kinetics of EC nanoparticles at different alkane-water interfaces and interface coverage, discussed in detail in Chapter 5, Pickering emulsions generated with EC nanoparticles at various ionic strengths are characterized in this section.

Figure 6.5 shows the effect of ionic strength on the EC nanoparticle-stabilized Pickering emulsions generated with an initial value of 0.33 for volume fraction of n-C10 ($f_{oil} = 0.33$).

Like the adsorption kinetics and oil-water interface coverage (see Sections 5.3 and 5.4), no
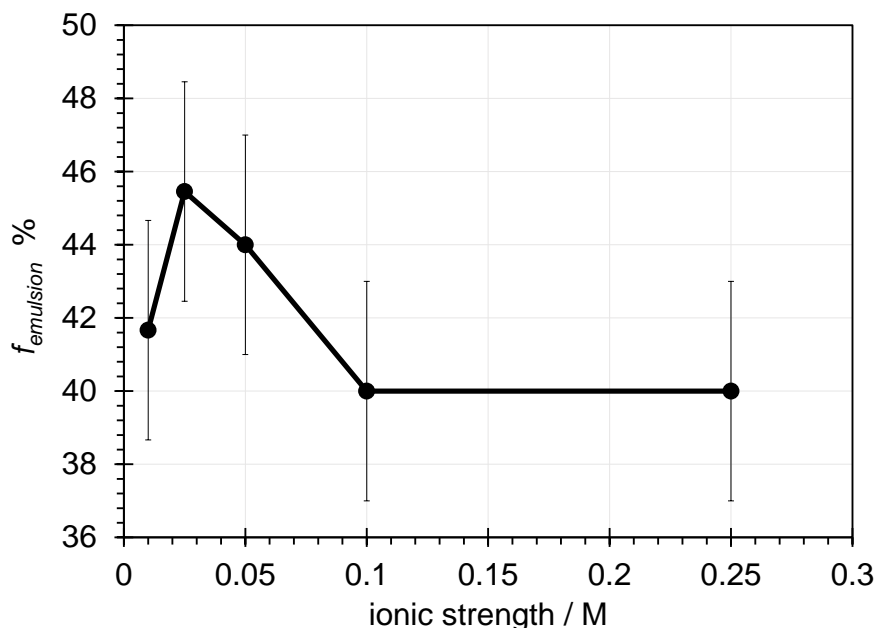
Figure 6.5: Volume percentage obtained for Pickering emulsions ($f_{emulsion}$) generated at $f_{oil} = 0.33$ for n-C10 and at various ionic strength after a day.

significant difference among $f_{emulsion}$, shown in Figure 6.5, is observed when ionic strength changes from 0.01 M to 0.1 M. This is also quantitatively supported by finding no significant difference for D_{32} calculated at three different levels of the ionic strength shown in Figure 6.6. These values are in excellent agreement with theoretical results: $D_{32} = 180$ μm obtained from Eq. 6.1. Nonetheless, the trend for $f_{emulsion}$ suggests that the largest volumes for Pickering emulsion could be obtained when the ionic strength is between 0.025 M and 0.05 (i.e., $\leq$CCC). In agreement with Brigg's hypothesis, at an ionic strength much greater than the CCC (e.g., 0.1 M − a powerful flocculating agent), a less stable Pickering emulsion is obtained as shown in Figure 6.6 where some oil release and accumulation on the top of the emulsion is evident (creaming leading to separation). The inferior stability of emulsions generated at ionic strength exceeding the CCC may be attributed to nanoparticle coagulation in the bulk of the suspension interfering with nanoparticle adsorption at the oil-water interface. In a vigorously stirred oil-water mixture above the CCC, the rate of coagulation might significantly exceed the rate of nanoparticle adsorption at the oil-water interface. Thus, although in systems at rest (e.g., pendant drops) full coverage is achieved
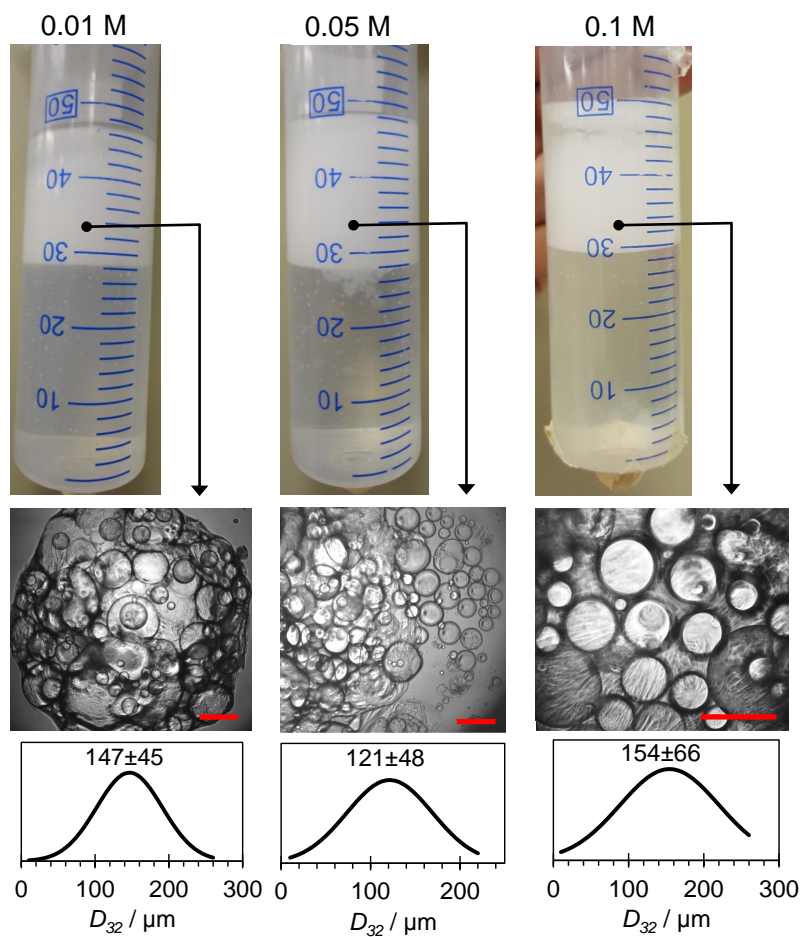
Figure 6.6: Pickering emulsions generated with EC nanoparticles at a concentration of 1 g L^{-1}, $f_{oil} = 0.33$ and three differnt ionic strengths. The scale bar on the microscope images is 200 μm.

(see Figure 5.7), this may not be the case during emulsification. It is also possible that, at a large enough ionic strength, nanoparticles adsorbed at the interface participate in a coagulation process resulting in breaking of the uniform packing of nanoparticles at the interface during drop collisions and the release of oil(see Figure 6.6 for ionic strength of 0.1 M). For the cases at or below the CCC, this phenomenon was not observed due to no or very slow coagulation − giving EC nanoparticles enough time to arrange themselves nicely at the interface in a spatial 3D network. Beyond the CCC, formation of such uniform 3D framework is less likely to happen − a feature which is assessed in detail in Section 6.5 where Pickering emulsions generated with EC nanoparticles are used to fabricate a polymeric porous material. The CCC is hence taken as the optimum ionic strength for EC nanoparticle-stabilized emulsions.

6.3.3   The effects of nanoparticle concentration

As expected from a mass balance on EC nanoparticles for Bancroft or anti-Bancroft emulsions, the initial EC nanoparticle concentration is another important parameter influencing the mean drop size and therefore, the properties of Pickering emulsions. At two levels of EC nanoparticle concentrations (1.0 g L^{-1} and 10 g L^{-1}), O/W Pickering emulsions (Bancroft-type) were generated while ionic strength and f_{oil} were kept constant at 0.05 M and 0.33, respectively. Under these conditions, the values of $D_{32} = 180$ μm and $D_{32} = 18$ μm are obtained from Eq. 6.1 for EC nanoparticle concentrations of 1.0 g L^{-1} and 10 g L^{-1}, respectively. Experimentally, the values of 121±48 μm (shown in Figure 6.6) and 58±21 μm (shown in Figure 6.7(a)) are obtained for concentrations of 1.0 g L^{-1} and 10 g L^{-1}, respectively, in fair agreement with the theoretical values. The theoretical mean drop size reflected in Eq. 6.1 is subject to the assumption that enough energy is available during emulsification to disperse the oil phase in drops of size just enough to accommodate all nanoparticles in suspension. Further work is needed to ascertain if this is the reason a mean droplet size of 58±21 μm instead of 18 μm (predicted by Eq. 6.1) was observed in emulsions generated from 10 g L^{-1} EC nanoparticle suspension.

In addition to the mean drop size (D_{32}), nanoparticle concentration also affects the volume of generated Pickering emulsion ($f_{emulsion}$). In order to assess this effect, Pickering emulsions were generated using the mechanical mixer (see Section 3.2) with a mixing time of 30s at ionic strength of 0.05 M, $f_{oil} = 0.33$, and three different EC nanoparticle concentration: 0.5 g L^{-1}, 1.0 g L^{-1}, and 2.0 g L^{-1}. $f_{emulsion}$ obtained for each set of experiments is shown in Figure 6.7(b). With the given input mechanical energy, oil is dispersed in water in a form of drops with a specific size of r^* [58]. At the concentration of 0.5 g L^{-1} for EC nanoparticles, there is not enough nanoparticles in the bulk to fully cover

89
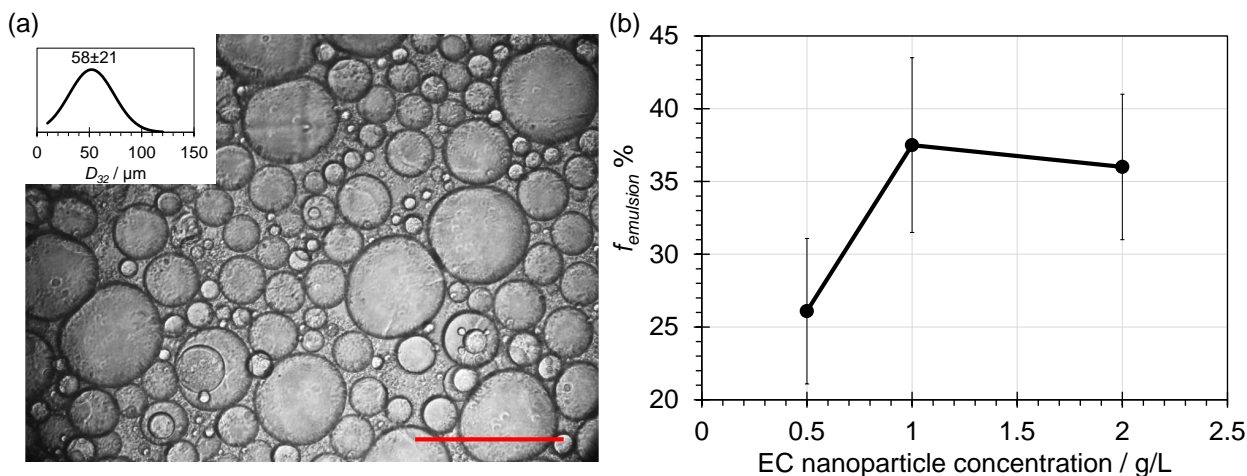
Figure 6.7: (a) Microscope image and drop size distribution of O/W Pickering emulsion generated with 10 g L^{-1} EC nanoparticles. The scale bar is 200 μm. (b) Percentage volume of generated Pickering emulsion ($f_{emulsion}$) at various EC nanoparticle concentration obtained after a day.

the oil drops in the size of r^* and therefore, EC nanoparticles are not effective in hindering oil drop coalescence. Notwithstanding, fully covered oil drops with a size of larger than r^* will be obtained at steady state, which makes less of the oil to be emulsified and thus, a smaller $f_{emulsion}$ was obtained, as shown in Figure 6.7(b). When enough EC nanoparticle are present at concentrations of 1.0 g L^{-1} and 2.0 g L^{-1}, oil drops with the size of r^* could be fully covered and same $f_{emulsion}$ was obtained. As previously discussed, the presence of a sufficient number of nanoparticles results in the formation of a 3D spatial framework that also improves the stability of Pickering emulsion. As explained later in this section, such a framework enables EC nanoparticle-stabilized emulsions to serve as templates for the fabrication of a porous material.

6.4   Mechanism of emulsion stability

Two possible mechanisms for stabilization of Pickering emulsions were discussed in Section 2.4 and illustrated in Figure 2.6. In steric stabilization, the oil-water interface is expected to be covered close to its jamming limit (i.e., 91%). The coverage of the n-C10-water interface by EC nanoparticles is shown in Figure 5.7 to be on average $95 \pm 14\%$ over a range of ionic strength from 0 to 0.1 M. Therefore, steric stabilization is assumed to be

the operative mechanism in the stabilization of Pickering emulsions by EC nanoparticles. Such high interface coverage (Θ_∞) may not however be necessary for steric stabilization be effective. Steric stabilization could be effective if the irreversibly adsorbed particles at a fluid interface do not provide enough space for the attachment of a particle already adsorbed at an approaching fluid interface. This provides enough barrier (of steric type) to prevent the coalescence of two fluid interfaces *via* steric stabilization. Looking at Figure 5.8, one finds that the required space to place a new particle at a fluid interface will not be available unless Θ_∞ becomes smaller than 23%. Below this critical value for Θ_∞, stabilization by bridge formation may be possible if the bridging particles are dispersed in the continuous phase. Even though bridge formation is suggested in some studies where the fluid interface is covered slightly more than 23% [116], experimental observations of bridge formation indicate that fluid interfaces are not covered more than 13 % [73, 164]. In particular, water drops in a W/O emulsion were covered at 10% by 3 μm silica nanoparticles [73]. Bridge formation provides a critical distance of $D_{cri} = 2r\cos\theta$ between two interfaces (as discussed in Section 2.4) [91]. This critical distance is shown in Figure 6.8(a) over a range of 10 nm to 250 nm for nanoparticle radius (r) and contact angles (θ) below 90° ($\theta = 90°$ is the theoretical limit for bridging particles to be effective). D_{cri} should provide sufficient separation for repulsion between the two fluid interfaces bridged by the nanoparticle to prevail over attraction. At a typical D_{cri} for nanoparticles (<50 nm), extended-DLVO computations for two approaching oil drops (n-C10), shown in Figure 6.8(b), predict a strong attraction. In order to compute the hydrophobic constant for two oil (n-C10) drops interacting across water (K_{232}), the combining rule suggested by Yoon *et al.* [192] was followed. With the knowledge of K_{131} (i.e., 8.7×10^{-23} J, reported in Table 5.4) and K_{132} (i.e., 7.6×10^{-20} J), K_{232} is computed from $K_{232} = K_{132}^2 / K_{131}$ using the geometric mean. Extended-DLVO computations indicate that nanometer-sized particles cannot effectively stabilize emulsions solely *via* bridge formation. It is hypothesized here that an attractive force must exist among the bridged nanoparticles to keep them tightly close to each other and to make a dense bridge. This attractive force is expected to arise during the thinning of the bridge which the latter is the consequence of attraction between two oil drops. Thinning of the bridge results in different contact angle at each side of bridged particle if one assumes that the contact line is pinned at the surface of bridged particles. The contact angle difference is expected to be the origin of a capillary-type attraction among the bridged particles. The discussed hypothesis needs further experimental and theoretical studies for justification.
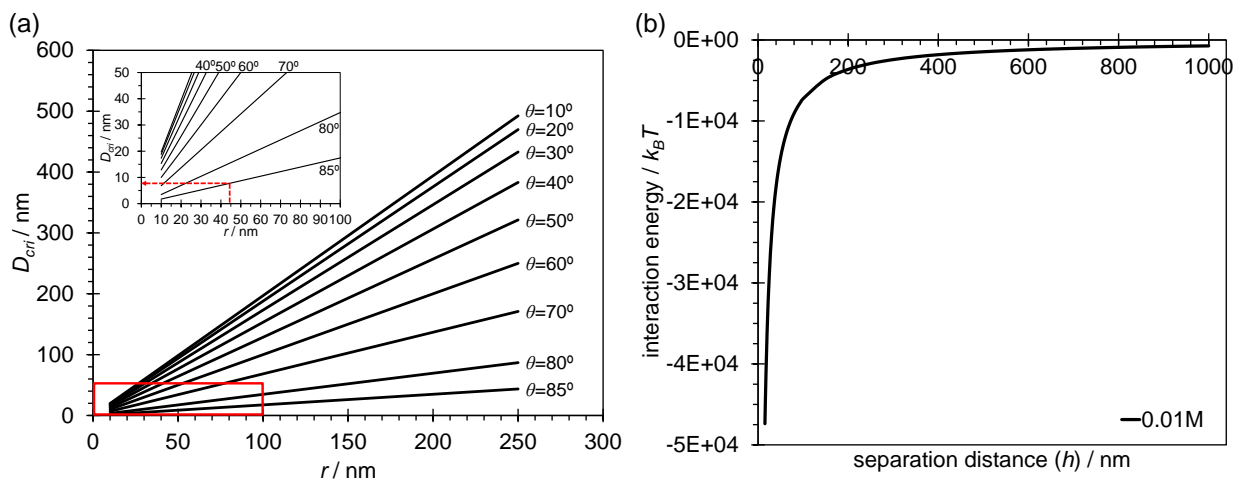
Figure 6.8: (a) Critical distance between two fluid interfaces separated by a nanoparticle with different sizes and wettabilities. The inset in (a) is a magnification of selected region and shows the situation applicable to EC nanoparticles at n-C10-water interface. (b) Extended-DLVO calculations for two n-C10 drops interacting in water.

6.5 High internal phase Pickering emulsions templated porous material fabrication

Emulsions with at least 70% [107] by volume of the dispersed phase (or 74% according to some [20, 21]) are categorized as high internal phase emulsions (HIPEs). Uniform (monodispersed) spherical drops are expected to be obtained in HIPEs containing a dispersed phase up to 74% by volume. Beyond this critical volume fraction, the dispersed phase could be a mixture of polydispersed spherical/non-spherical (polyhedral) cells [20]. As discussed earlier, phase inversion can occur in an emulsion when the volume fraction of dispersed phase increases. In order to prevent the phase inversion and successfully generate an HIPE, typically a proper surfactant (or mixture of surfactants and polymers) that is completely insoluble in the dispersed phase of the emulsion must be chosen [20]. It is discussed in detail in previous chapters that Pickering emulsions are much more stable than those stabilized by surfactants. This applies to HIPEs as well. Therefore, generation of high internal phase Pickering emulsions (HIPPEs) have been of the focus of recent studies [22, 85, 198]. Like surfactant, colloidal (nano)particles, that are the emulsifiers in Pickering emulsions, must also prevent the phase inversion at high volume fraction of dispersed phase to make the generation of HIPPEs possible. This challenge could be resolved under the following

conditions [85]:

- colloidal (nano)particles must be necessarily well-dispersed in the continuous phase

- colloidal (nano)particles should readily adsorb at the oil-water interface

- colloidal (nano)particles need to act as an effective emulsifier

Common nanoparticles used in stabilizing Pickering emulsions such as silica nanoparticles are very hydrophilic making them generally unfit according to these criteria. Generation of HIPPEs with these nanoparticles has been limited[85]. EC nanoparticles, however, meet all of the aforementioned criteria for generation of an HIPPE. It was shown in Section 6.3.2 that by tuning the ionic strength, quite stable O/W HIPPEs containing $(75\pm4)\%$ by volume of oil were successfully obtained. Such highly dense emulsions have been used elsewhere as a template to fabricate advanced functional materials used in various applications from semiconductors [115] to food engineering [37]. Fabrication of a porous polymeric material from EC nanoparticle-stabilized HIPPEs is reported below.

6.5.1   Porous materials fabrication and characterization

In order to fabricate porous polymeric materials by templated emulsions, the dispersed drops need to be removed. To this end, Pickering emulsions generated with EC nanoparticles at a concentration of 1 g L^{-1} were dried at a temperature of $\sim 90°C$ for at least two days using a conventional dryer. Figure 6.9(a) shows how typically the dried material looks like. Under different conditions for ionic strength and f_{oil}, EC nanoparticle-stabilized Pickering emulsions result in polymeric materials with different microstructure. SEM images of these materials are shown in Figure 6.9(b) to (g).

The porosity of this material originates from the structure of the dispersed phase, which must be maintained during the course of drying. As discussed in detail in Section 6.3.2, the stability of Pickering emulsions generated with EC nanoparticles decreases if the ionic strength is larger than the CCC. Therefore, beyond the CCC, the dispersed phase does not maintain its structure as well as at or below the CCC and a less porous material is expected to result from such Pickering emulsions. This is reflected in Figure 6.9(e) and (f) where a less porous material is obtained from O/W Pickering emulsions generated at an ionic strength of 0.1 M and 0.25 M, respectively. On the contrary, a fairly porous polymeric material is obtained when the ionic strength is below the CCC (see Figure 6.9(b) to (d)). Stability of the Pickering emulsion is not the only factor controlling the structure
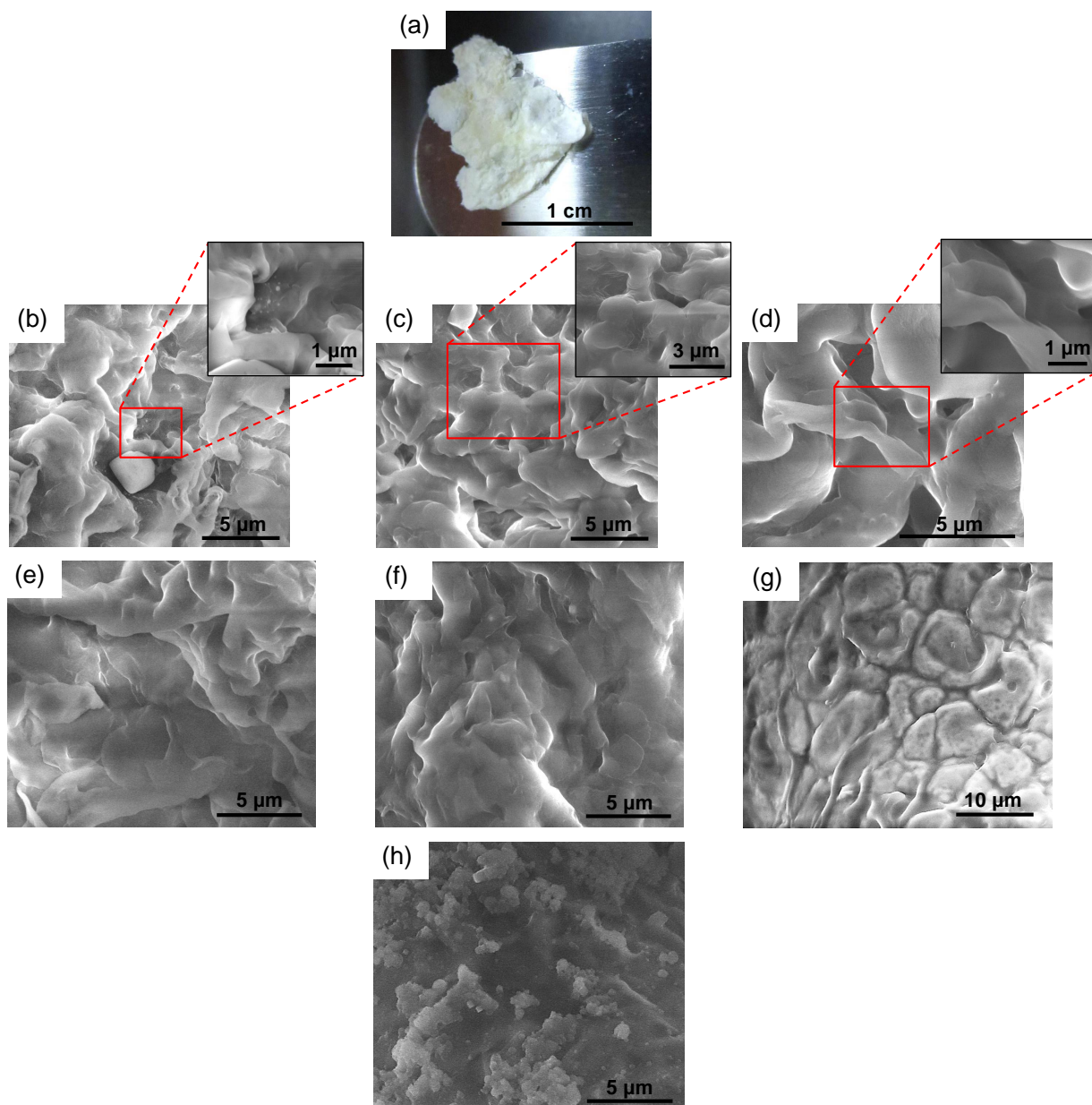
Figure 6.9: (a) Porous polymeric material templated from EC nanoparticle-stabilized Pickering emulsions. (b) to (g) SEM images of porous polymeric materials obtained from dried Pickering emulsions generated at a concentration of 1 g L^{-1} for EC nanoparticles and $f_{oil} = 0.33$ in (b) to (f), $f_{oil} = 0.5$ in (g), and at an ionic strength of (b) 0.01M, (c) 0.025 M, (d) 0.05 M, (e) 0.1 M, (f) 0.25 M, and (g) 0.05 M. (h) SEM image of a material fabricated from a coagulated Pickering emulsion at ionic strength of 0.05 M and at $f_{oil} = 0.33$.

of dispersed phase. If the continuous phase could be kept rigid during the drying, then less deformation in the microstructure of porous materials would be obtained and a more uniform pore size distribution would be expected. In the cases shown in Figure 6.9(b) to (f), f_{oil} was set to be 0.33. At this f_{oil}, the volume fraction of oil in the generated O/W Pickering emulsions was at least 70% − a necessary condition for HIPPEs. SEM imaging with a higher resolution could clarify if EC nanoparticles maintain their spherical structure in the wall of final dried materials shown in Figure 6.9(b) to (f). This, however, is less likely to be the case since the Pickering emulsions were kept in the oven for two days at $\sim 90°$C − a temperature close enough to the glass temperature of EC ($\sim 130°$C) softening EC to create an apparent solid wall.

Figure 6.9(g) shows a dried porous material obtained from a W/O Pickering emulsion generated at $f_{oil} = 0.5$ and at the CCC. A clear difference in the structure of this material is observed from the ones fabricated from O/W Pickering emulsions shown in Figure 6.9(b) to (f). According to the measurements of size distribution for the dispersed phase at different f_{oil} discussed in Section 6.3.1, the large separated dried regions shown in Figure 6.9(g) seem to correspond to the water drops. Such regions were not observed in the cases shown in Figure 6.9(b) to (f) because a much smaller mean size for the dispersed oil was obtained for O/W Pickering emulsions. In Section 5.4 and Figure 5.5, two possible scenarios for the adsorption of EC nanoparticles at a fluid interface at ionic strengths larger than the CCC were discussed. It was shown that only individual nanoparticles adsorb at the interface. A dried material is fabricated from a coagulated Pickering emulsion at ionic strength of 0.05 M and at $f_{oil} = 0.33$ and its SEM image is shown in Figure 6.9(h). Like the cases shown in Figure 6.9(e) and (f), the fabricated material is not porous. From the patches of coagulated EC nanoparticles, it can be concluded, in line with earlier evidence, that the nanoparticle aggregates could not stabilize a Pickering emulsion and only individual nanoparticles are effective in emulsion stabilization.

6.5.2   Oil water separation

The porous polymeric material fabricated from EC nanoparticle-stabilized HIPPEs, characterized in Section 6.5.2, is a hydrophobic/oleophilic material which may be used to separate oil and water. HIPPEs were used as the template since they contain larger volume fraction of dispersed phase (i.e., oil in O/W emulsions) than that for non-HIPPEs − a condition which supports fabrication of a more porous polymeric material. In one proposed approach, shown in Figure 6.10(a), the fabricated material is used to collect oil (coloured in red) spread on water. This is of great practical application in cleaning surface water from oil or organic contaminant spills especially when a fast response is needed when

spill happens. In another approach, shown in Figure 6.10(b), a metallic mesh was treated partially by an HIPPE generated at an EC concentration of 10 g L^{-1}, ionic strength of 0.05 M, and $f_{oil} = 0.33$. The mesh was then dried following the same procedure explained earlier in Section 6.5.1. It is shown on Figure 6.10(b) that drops of water or n-C10 do not spread on the untreated section of the mesh. On the treated section, water drop still does not spread but the n-C10 spreads very fast in a matter of seconds (similar to that on a film of EC coated a glass slide). Such a property is also of potential practical use in fabricating advanced functional membranes for oil/water separation. In addition to these features, the unique properties of EC (e.g., non-toxic, food-grade, etc.) make the fabricated porous polymeric material from EC nanoparticle-stabilized HIPPEs a strong candidate to develop environmentally friendly approaches to tackle some a number of environmental challenges.

6.6   Summary

Pickering emulsions are successfully generated exclusively with EC nanoparticles. The optimum conditions of oil volume fraction, ionic strength, and EC nanoparticle concentration at which the most stable emulsion is obtained were determined through a series of drop size distribution and emulsion stability tests. It was found that ionic strength has no significant effect on the mean size for the dispersed phase, but plays a key role in emulsification and emulsion stability. It is also shown in agreement with theory, that a phase inversion from O/W to W/O happens at or beyond the oil volume fraction of 0.5. The generated O/W emulsions contained $75 \pm 4\%$ oil making them a high internal phase Pickering emulsions. These emulsions were successfully templated to fabricate polymeric porous materials to be potentially used in oil-water separation applications.
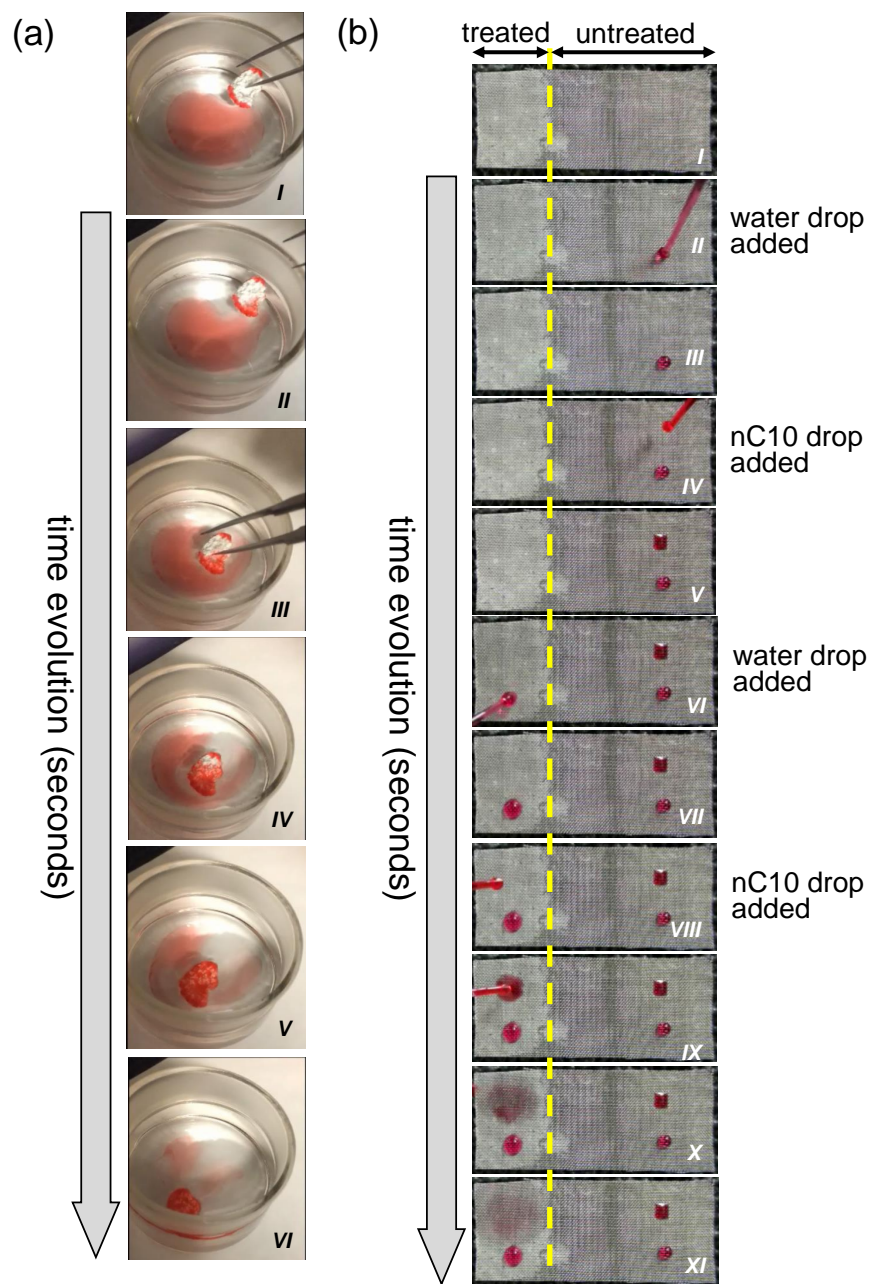
Figure 6.10: (a) Porous polymeric material fabricated from EC nanoparticle-stabilized HIPPEs collects oil (coloured in red) from the surface of water. (b) Responses of a treated/untreated metallic mesh by HIPPE to water and n-C10 drops.

Chapter 7

Ethyl Cellulose Nanoparticle Transport in Porous Media

7.1   Introduction

Previous chapters have examined in detail fundamental aspects of the interaction of EC nanoparticles with fluid interfaces. In these studies the fluid interfaces under consideration were immobile and nanoparticle transport to the interface was by diffusion alone. The introduction of EC nanoparticle suspensions to porous media requires that consideration be given to the coupling of nanoparticle attachment to fluid (and solid) interfaces with convective transport in a network of pores. Of a great variety of multiphase flow scenarios involving nanoparticle suspensions only the most basic are considered here: transport of nanoparticle suspensions in water-saturated porous media and transport of nanoparticles in porous media containing an immobile non-wetting phase. Transparent glass micromodels, thermogravimetric analysis of effluent samples and simple continuum models are used to observe and model nanoparticle transport as a function of ionic strength and Peclet number. It is experimentally demonstrated that co-injection of gas and EC-nanoparticle suspensions results in the generation of foam in situ, a finding that suggests potentially important application of these particles to foam flooding for hydrocarbon recovery.

7.2 EC nanoparticle transport through a saturated porous medium

7.2.1 Micromodel characterization

An important characteristic of the glass micromodel is its pore volume (PV), which must be known for proper interpretation of transport tests. As explained in Section 3.3.1, the shape of pores and throats of glass micromodel used in this study is assumed to be that of oblate spheroids (see Figure 3.5). From knowledge of the number of pores (n_p) and throats (n_t), PV for the micromodel the pore volume can be obtained from the average volume of pores and throats (obtained from the respective distributions) as $PV = n_p V_p + n_t V_t$, where V_p and V_t are the average volumes of oblate spheroids corresponding to pores and throats, respectively. In order to compute the volume of an oblate spheroid ($V = \frac{4}{3}\pi w^2 \delta$, see Figure 3.5), the width (w) and depth (δ) of void body (pore or throat) need to be determined. w for individual pores and throats (i.e., w_p and w_t, respectively) was determined directly by analyzing the images taken from the glass micromodel. Pore size distribution (PSD) for pores and throats was successfully obtained by running an open-source image analysis code [140] using MATLAB$^{\text{®}}$ (see Section 3.3.1 and Appendix D) on at least four images randomly taken from different sections of the micromodel. Figure 7.1(a) and (b) illustrate the determination of w_p and w_t for an image taken from the micromodel and Figure 7.1(c) shows bimodal PSD for the given micromodel with an average value of 144 ± 13 μm and 419 ± 70 μm for w_t and w_p, respectively, which are in an excellent agreement with manual measurements with naked eye on microscope images of pores and throats (Figure 7.1(d)). The distribution of pores and throat widths is assumed normal and the average values are calculated with 95% confidence. Errors associated with the reported values are explained by the non-perfect uniformity of the glass micromodels, as observed with the naked eye, and with the limited resolution of the images. As a result of image analysis, n_p and n_t are estimated to be 14,894 and 29,789, respectively.

δ_p and δ_t for individual pores and throats, respectively, were computed from Eqs. 3.4 to 3.7. To this end, capillary height measurements were made as explained in Section 3.3.1 in triplicate of characteristic drainage and imbibition capillary pressures of the glass micromodel. With a value of 1043 ± 104 Pa obtained for P_c^{im}, δ_p is directly calculated from Eq. 3.4 to be 208 ± 47 μm with the earlier estimates for w_p. δ_t, however, is computed from Eqs. 3.5 to 3.7 following a trial-and-error procedure depicted in Figure C.3 in Appendix C. With knowledge of $P_c^{dr} = 2209 \pm 139$ Pa obtained from capillary height tests, and an initial guess of 100 μm, a final value of 129 ± 5 μm is found for δ_t. Comparing δ_p and δ_t, one
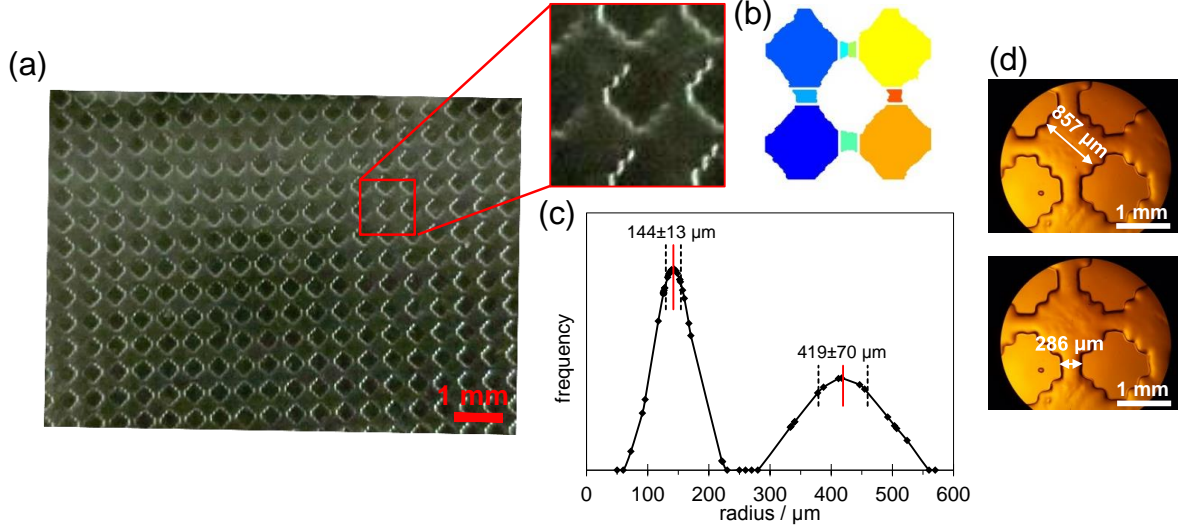
Figure 7.1: (a) The glass micromodel used for transport studies. (b) Image analysis on the section of glass micromodel using the code provided in [140] (see Appendix D). (c) Pore size distribution for the glass micromodel shown in (a). (d) Microscope images of pores and throats.

finds the same magnitude for the depth of pores and throats as expected from fabrication procedure [25, 26]. The assumption of oblate spheroidal shape for pores and throats is reasonable since $w_p > \delta_p$ and $w_t > \delta_t$. Given the values of w_p, w_t, δ_p, and δ_t, V_p and V_t are calculated considering an oblate spheroid and consequently, PV is found to be 2.6 ± 0.5 mL.

7.2.2   Effects of ionic strength

Transport studies were conducted following the procedure explained in Section 3.3.2. In the absence of salt, EC nanoparticle suspension was introduced to the water-saturated ($S_w = 1$) glass micromodel characterized in 7.2.1 at a constant flowrate of 75 μL min^{-1}. A transport test under the same conditions, but using a conservative tracer (NaCl) at an initial concentration of 1.52 mol L^{-1} was also conducted. The samples taken from the effluent were analyzed using TGA to obtain the effluent concentration (see Section 3.3.2) and the results are shown in Figure 7.2(a). This figure shows that after the injection of ~ 1.2 PV the reduced concentration ($N_{b,eff}/N_{b0}$) in the effluent for both EC nanoparticles and NaCl reaches unity. Comparing the BCs for EC nanoparticles and NaCl, one finds that
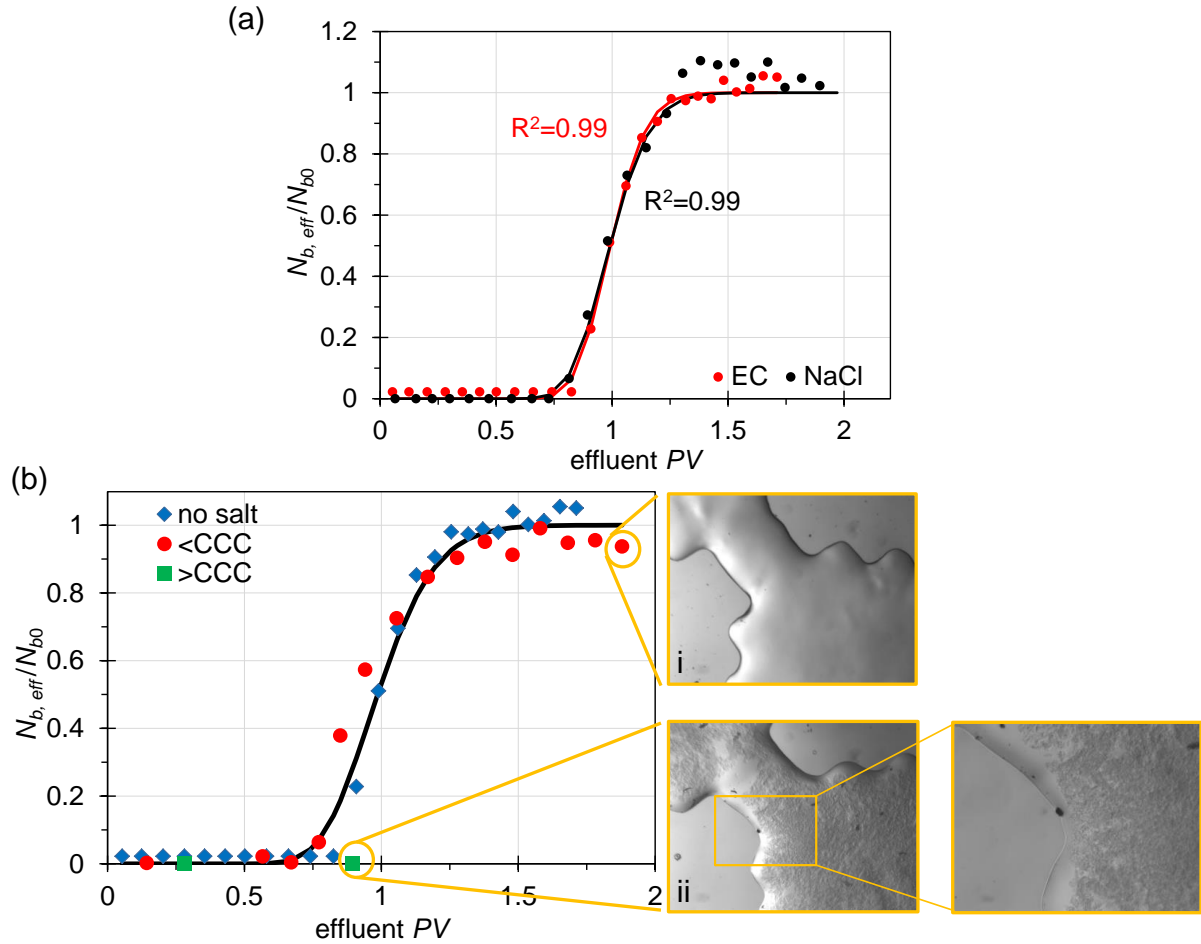
Figure 7.2: (a) Breakthrough curves for the effluent concentration of EC nanoparticles (red) and NaCl (black) transported through a water-saturated glass micromodel. The solid lines are the fitted CDE model (Eq. 7.2). (b) Breakthrough curves for the concentration of EC nanoparticles at three levels of ionic strength: no salt, 0.01 M (<CCC), and 0.1 (>CCC). (b)-i and (b)-ii are the microscope images of a pore and a throat of the micromodel obtained at ionic strength below and above the CCC, respectively. The solid line is the CDE model (Eq. 7.2).

EC nanoparticles are transported as a conservative tracer. This is expected since a strong repulsion exists among EC nanoparticles (see Chapter 4) and between EC nanoparticles and glass surface (both surfaces with negative charges). Hence one expects no coagulation or attachment to the pore walls.

Eq. 2.15 is used to predict BC for the effluent concentration of EC nanoparticles and NaCl. Since no retardation is observed in the experimental data (Figure 7.2(a)) or expected on theoretical grounds, the two terms R_s and R_i have no contribution in the CDE model. Eq. 2.15 is thus simplified to the following at $S_w = 1$

$$\frac{\partial N_b}{\partial t} = D_h \frac{\partial^2 N_b}{\partial x^2} - v_p \frac{\partial N_b}{\partial x}$$ (7.1)

Eq. 7.1 is written in terms of dimensionless parameters $\overline{x} \equiv x/L$, $\overline{N_b} \equiv N_b/N_{b0}$, and $\overline{t} \equiv D_h t/L^2$ as follows

$$\frac{\partial \overline{N_b}}{\partial \overline{t}} = \frac{\partial^2 \overline{N_b}}{\partial \overline{x}^2} - Pe \frac{\partial \overline{N_b}}{\partial \overline{x}}$$ (7.2)

where Pe is the Peclet number defined as $Pe \equiv v_p L/D_h$. The best fit at which the sum of squared errors of predictions is minimized is obtained by changing the model parameter using the CXTFIT open-source algorithm [172]. In this algorithm, the model parameter is longitudinal dispersivity, α_L, from which the dispersion coefficient (D_h) is computed via $D_h = \alpha v_p$ assuming negligible effective molecular diffusion [53, 145], an assumption which will be examined further. The values obtained for α_L, D_h, and Pe for EC nanoparticles and NaCl are reported in Table 7.1. One observe no significant difference between the transport parameters for NaCl and those for EC nanoparticles in the absence of salt. The magnitude of Pe reported in Table 7.1 for both NaCl and EC nanoparticles in the absence of salt is squarely within the range where mechanical dispersion dominates [53]. Therefore, the earlier assumption to neglect the effect of molecular diffusion in longitudinal dispersivity is verified. The computed α_L ($O(10^{-3})$ m) and D_h ($O(10^{-7})$ m^2 s^{-1}) for the given micromodel, which has a length of 30.7 cm, is in agreement with reported values in the literature [86, 151].

Transport of EC nanoparticles through the glass micromodel was also conducted at ionic strengths of 0.01 M (below the CCC) and 0.1 M (above the CCC) under the same flow conditions. The BC for these transport tests is shown in Figure 7.2(b). Comparing to the transport of EC nanoparticles when no salt is present, one finds that ionic strength at a level below the CCC has no significant impact on the transport of EC nanoparticles. A pore-scale image of the micromodel (Figure 7.2(b)-i) shows also no sign of EC nanoparticle accumulation within the medium. Above the CCC, however, EC nanoparticles very rapidly

Table 7.1: Model parameters (α_L, D_h, and Pe) computed for 1D transport of NaCl and EC nanoparticles through a glass micromodel at a volume flowrate of 75 μL min^{-1} and various ionic strengths.

transported species	ionic strength (M)	α_L (cm)	D_h (m^2 s^{-1})	Pe
NaCl	1.52	0.3 ± 0.1	$(4 \pm 2) \times 10^{-7}$	104 ± 61
EC nanoparticle	0	0.2 ± 0.1	$(3 \pm 1) \times 10^{-7}$	135 ± 44
EC nanoparticle	0.01	0.4 ± 0.1	$(6 \pm 1) \times 10^{-7}$	70 ± 19
EC nanoparticle	0.1	$-$	$-$	$-$

coagulate within the porous medium as shown in Figure 7.2(b)-ii plugging up pores and throats, effectively destroying permeability. The porous medium is found to completely clog up after the injection of about one pore volume (see Figure 7.2(b)). The transport model parameters, α_L, D_h, and Pe, are again computed using Eq. 7.2 for the EC nanoparticle transport at an ionic strength of 0.01 M. The values for these parameters, reported in Table 7.1, are not significantly different from those obtained for NaCl and EC nanoparticles in the absence of salt condition and are in agreement with the literature.

7.2.3   Effects of velocity

The same glass micromodel was used to study the transport of EC nanoparticles in the absence of salt at two different injected flowrates. The results for the flowrate of 75 μm min^{-1} are shown in Figure 7.2. Figure 7.3 shows the BC of EC nanoparticles injected at a lower of flowrate of 0.015 μm min^{-1}. From the fitted CDE model (Eq. 7.2), $\alpha_L = 0.7 \pm 0.3$ cm, $D_h = (2 \pm 1) \times 10^{-7}$ m^2 s^{-1}, and $Pe = 42 \pm 11$ are obtained. The error associated with the measurements for the flowrate of 15 μm min^{-1} is relatively larger than that for 75 μm min^{-1}. This is possibly due to larger variations in time recording during sampling as well as the sensitivity of weighing procedure in TGA, especially during the transient time $-$ from 0 to 1 for $N_{b,eff}/N_{b0}$ over $\sim$0.4 PV.

At the pore scale, the Pe number is defined as $Pe = v_p L_p/D$, where D is the diffussion coefficient of EC nanoparticles computed from Stokes-Einstein theory (Eq. 2.9) and L_p is a characteristic length for the pores, which here has the approximate value of 487 μm estimated from $L_p \cong w_p + w_t/2$. Comparing D_h $O(10^{-7})$ m^2 s^{-1} obtained here for the transport of EC nanoparticles to the diffusion coefficient of EC nanoparticles $O(10^{-12})$ m^2 s^{-1}, one readily concludes that the transport of EC nanoparticles under the given conditions
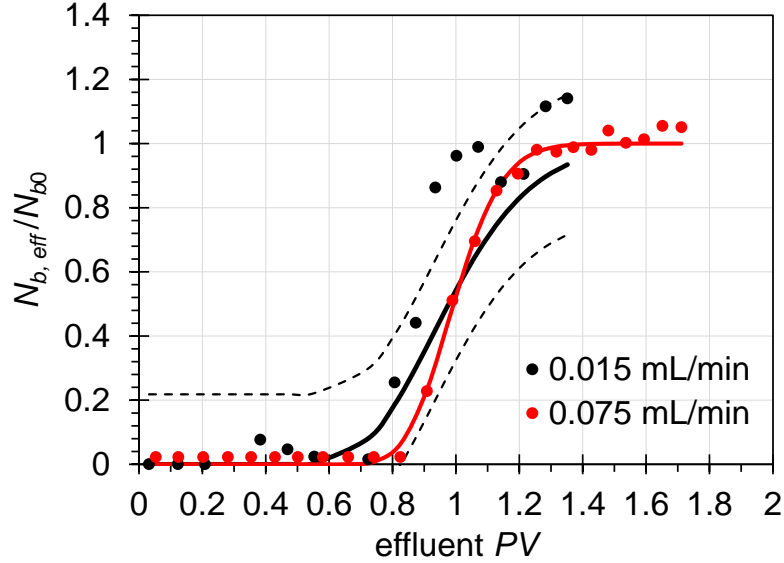
Figure 7.3: Breakthrough curves for the effluent concentration of EC nanoparticles transported in the absence of salt and under a constant flowrate of 0.015 μm min^{-1} (black) and 0.075 μm min^{-1} (red). The solid lines are the CDE model (Eq. 7.2).

is dominated by mechanical dispersion. This compares very well with the literature values for reduced dispersion coefficient as a function of pore Pe number (see Figure 7.4).

7.3 Predictions for EC nanoparticle transport through an unsaturated porous medium

As discussed in Section 2.5.5, the interaction of nanoparticles with bubbles and oil drops in during the injection of nanoparticle suspensions in porous media is expected to lead to the irreversible attachment of EC nanoparticles on air-water or oil-water interfaces. Thus, gas bubbles and oil drops would be expected to act as perfect "sinks" of finite capacity related to the specific surface area of fluid-fluid interfaces and the density of nanoparticle packing at the interface. Considering no attachment on the solid matrix ($R_s = 0$), as discussed in previous section, Eq. 2.15 is used here coupled with Eq. 2.29 to model the transport of EC nanoparticles through an unsaturated porous medium. Following a similar approach to the one shown in Section 7.2.2 Eq. 2.15 and 2.29 are written in terms of dimensionless
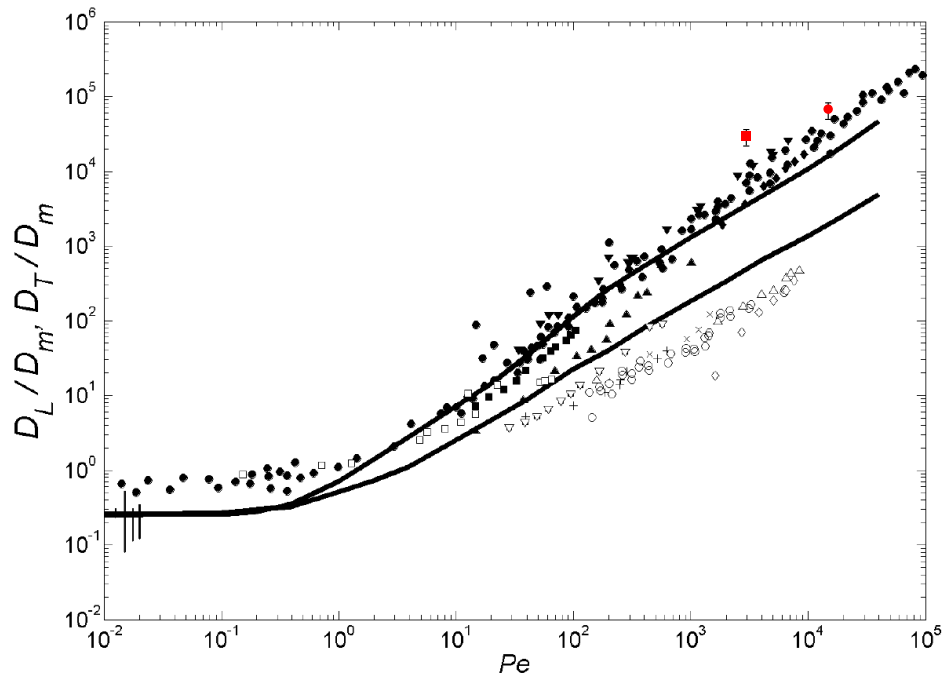
Figure 7.4: Normalized longitudinal, D_L, (upper solid line) and transverse, D_T (lower solid line) dispersion coefficients with molecular diffusion coefficient, D_m, as a function of pore-scale Peclet number from [8]. Reprinted with permission from [8], Copyright© 2006 Society of Petroleum Engineers. The red points are experimental results of this study representing the transport of EC nanoparticles in a glass micromodel in the absence of salt at two injected flow rates: 75 μL min^{-1} (circle) and 15 μL min^{-1} (square).

parameters as follows

$$\frac{\partial \overline{N_b}}{\partial \overline{t}} = \frac{\partial^2 \overline{N_b}}{\partial \overline{x}^2} - Pe\frac{\partial \overline{N_b}}{\partial \overline{x}} - Da_I \overline{N_b} B_i(\Theta_i) \tag{7.3}$$

$$\frac{\partial \Theta_i}{\partial \overline{t}} = \frac{k_i L^2}{D_h} N_{b0} \pi r^2 \overline{N_b} B_i(\Theta_i) \tag{7.4}$$

where $Da_I \equiv k_i L^2 (a_0)_i / D_h$. From DST and IFT data interpretations, it is shown that the order of magnitude of the adsorption constant is $O(10^{-6})$ m s^{-1} (see Chapter 5). To relate the specific surface area of bubble/drop interface to water saturation, we adopt the empirical formula $(a_0)_i = c_1(1 - S_w)^{c_2}$ with c_1 and c_2 [156] to obtain $(a_0)_i = 3040$ m^{-1} for a water saturation of 0.5. Eq.7.3 and Eq. 7.4 are solved using the method of lines (see Appendix D) with the following boundary and initial conditions.

$$x = 0, \text{all} t : N_b = N_{b0} \tag{7.5}$$

$$x = L, \text{all } t : \frac{\partial N_b}{\partial x} = 0 \tag{7.6}$$

$$t = 0, \text{all } x : N_b = 0 \tag{7.7}$$

$$t = 0, \text{all } x : \Theta_i = 0 \tag{7.8}$$

The results for concentration profile of EC nanoparticles and the fluid interface coverage along the porous medium are shown in Figure 7.5(a) and (b), respectively, assuming an initial concentration of 1 g L^{-1} and the RSA blocking function with $\Theta_\infty = 0.91$. It is shown in Figure 7.5(b) that after the injection of about 1.6 PV, fluid interfaces everywhere within the porous medium are covered at the maximal limit (i.e., 0.91). Adsorption of nanoparticles is fast as evidenced by comparing the speed of bulk and interfacial concentration fronts. A Damkohler number of 4264 confirms this conclusion. A long tail at high values of interfacial coverage, however, is due to the effects of surface blocking on the adsorption flux. As shown in Figure 7.6, adsorption at the fluid-fluid interface introduces very significant retardation to nanoparticle transport. Verification against experiments is necessary before these illustratve model predictions are generalized.

7.4 *in situ* foam flooding

Foam flooding can be very effective in the recovery of oil from porous media, as discussed in Section 2.5.4.2. The generation of foam in situ can be an interesting variation of this
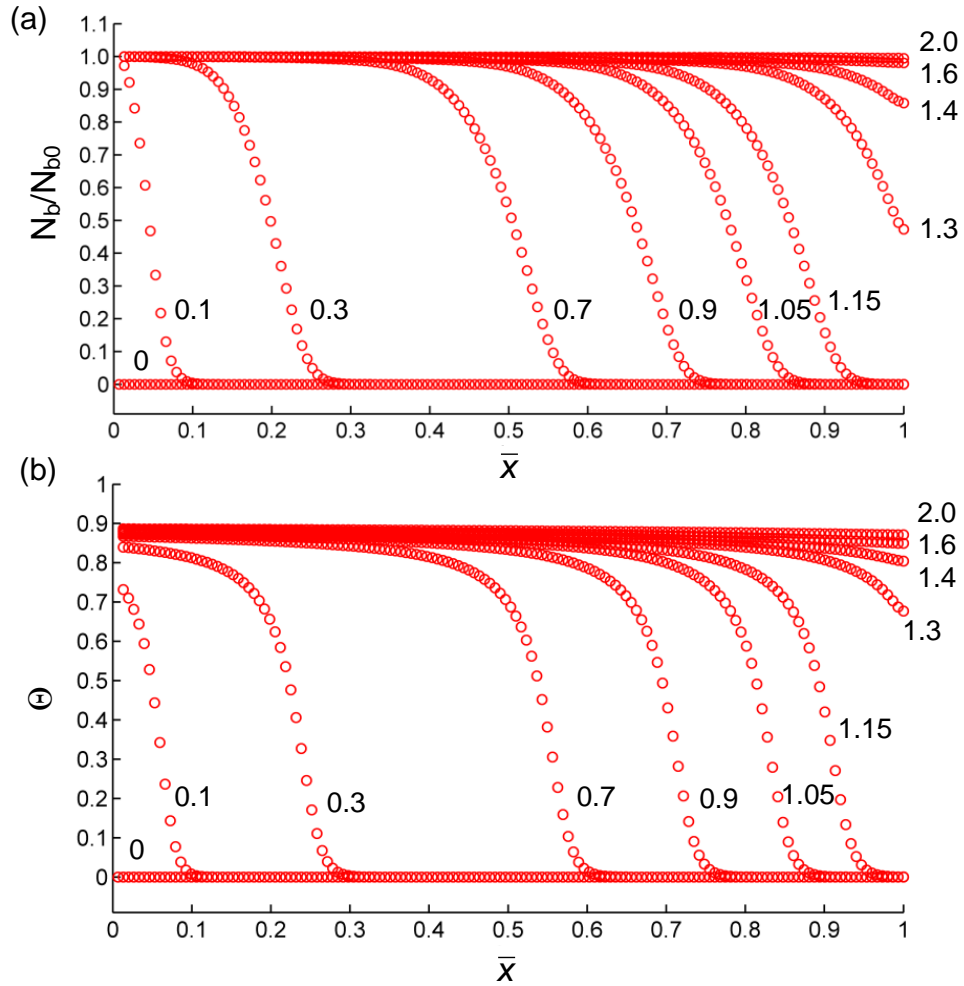
Figure 7.5: (a) Concentration profile for EC nanoparticle transported through a 50 % water-saturated medium at $Pe = 135$ and $Da_I = 4264$. (b) Interface coverage of fluid interface by EC nanoparticles. The numbers in (a) and (b) represent injected pore volume.
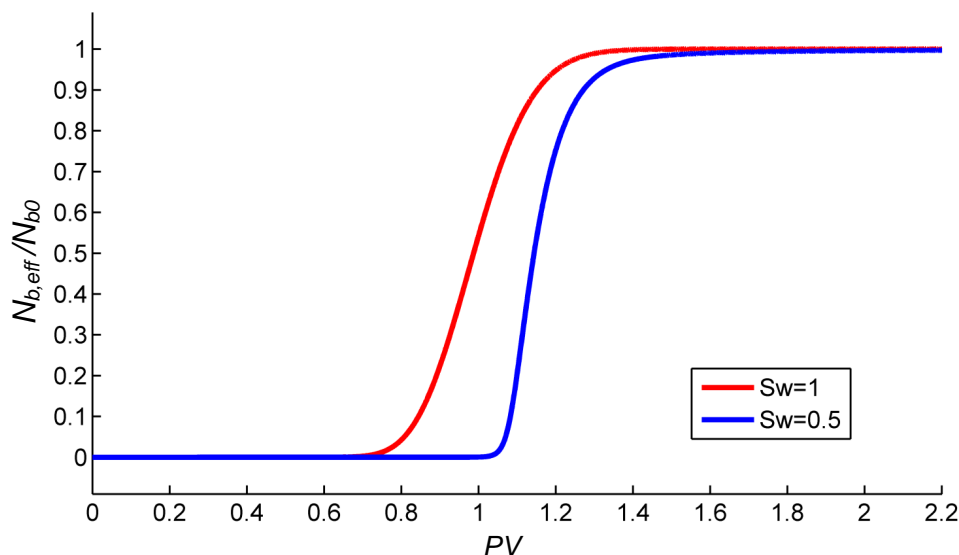
Figure 7.6: Breakthrough curves for the effluent concentration of EC nanoparticles transported through a micromode at $Pe = 135$ and $Da_I = 4264$ with different saturations, $S_w = 1.0$ and $S_w = 0.5$.

technology that overcomes several challenges associated with the injection of ex situ generated foam. Since EC nanoparticles can act as a very strong foam stabilizer [82], foam generation *insitu* during the co-injection of gas (nitrogen) and EC nanoparticle suspension was studied in a glass micromodel. Figure 7.7 shows a glass micromodel with random pattern before and after the co-injection. The ionic strength is adjusted to be below the CCC to prevent nanoparticle coagulation. Stable foams that last for more than a day following the end of injection are shown to be successfully generated inside the porous medium (see Figure 7.7(b)). This demonstration, suggests that an environmentally friendly in situ foam flooding technology using EC nanoparticles instead of surfactants for applications in oil recovery and NAPL displacement may be possible. This will require additional studies of the pore-scale aspects of foam interaction with oil ganglia.

7.5   Summary

This chapter addressed a novel engineering application of EC nanoparticles for a potential application in displacing ganglia from porous media: *in situ* foam flooding. To this end,
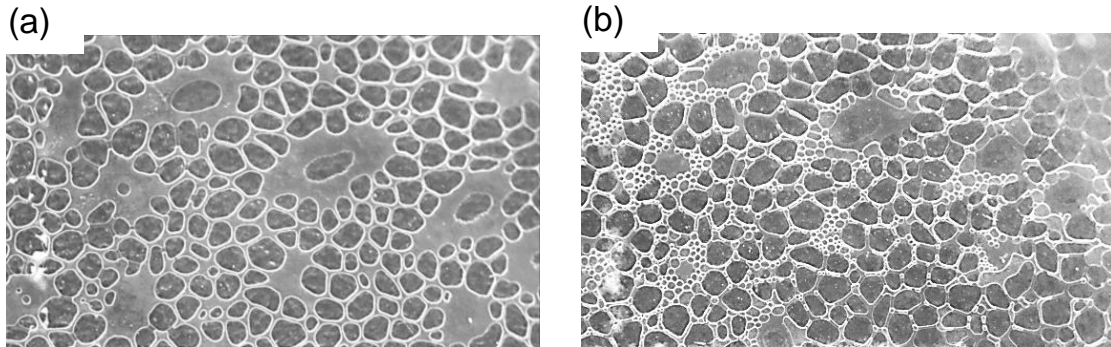
Figure 7.7: A section of glass micromodel with random pattern saturated initially in water at $S_w = 1$ (a) before and (b) after the co-injection of EC nanoparticle suspension (0.05M NaCl) and gas (nitrogen).

transport of EC nanoparticles in the absence of salt was first conducted in a water-saturated permeable medium (a glass micromodel) and found to transport as a conservative tracer (NaCl). This behaviour was also observed for ionic strengths below the CCC. However, above the CCC, coagulation of EC nanoparticles inside the micromodel clogged the pores and throats resulting in no effluent after the injection of $\sim 0.8\ PV$. It is shown that the classic CDE model is adequate to predict the transport parameters, dispersivity and dispersion coefficient, in agreement with literature and an extension of this model to transport of EC nanoparticles in porous media containing immobile non-wetting phase ganglia was provided. Finally, foam generation *in situ* by co-injection of EC nanoparticle suspension and gas is successfully demonstrated.

Chapter 8

Conclusions and Recommendations

8.1   Summary and conclusions

The present thesis sought to inform two novel engineering applications of ethyl cellulose (EC) nanoparticles following a bottom-up approach:

- fabrication of functional materials for oil-water separation

- improvement of *in situ* foam flooding technology to recover oil from porous media

Ethyl cellulose is a non-biodegradable, non-toxic, and food-grade material that is derived directly from cellulose. Hydrophobic EC nanoparticles are synthesized *via* an antisolvent method in electrostatically stabilized in a surfactant-free aqueous medium − properties to make EC nanoparticle suspensions an ideal colloidal model system. To meet the objectives of this work, a multiscale approach is followed to address a number of fundamental and practical questions by conducting experiments combined with theoretical models.

Long-term (*ca.* months) stability of EC nanoparticles suspended in water was attributed to the interactions among EC nanoparticles dominated by the electrostatic repulsion. Electrostatic repulsion is weakened by tuning the ionic strength. From qualitative and quantitative analysis, in agreement with extended-DLVO theoretical computations, it is found that at or beyond an ionic strength of 0.05 M the suspension of EC nanoparticles becomes unstable. Regardless of ionic strength (at a range of 0M to 0.1M), however, a barrier-less irreversible adsorption of EC nanoparticles at the air-water and alkane-water interfaces is found from extended-DLVO computations. Interpretation of dynamic surface/interfacial

tension measurements with a recently developed mechanistic model also shows no variation in adsorption energy, contact angle, and steady state surface (interfacial) tension with respect to ionic strength. It is therefore concluded that the EC nanoparticle adsorption to fluid interfaces is dominated by hydrophobic interactions. Dynamic surface/interfacial measurements together with theoretical expectations from extended-DLVO show that the fluid interfaces examined in this work are tightly covered by EC nanoparticles at the maximal limit of 91% corresponding to a hexagonal pattern at any level of ionic strength. Salt, however, has an effect on the rate of approach to this maximum coverage (late stages of adsorption) which, unlike the early stages of adsorption, is controlled by the rearrangement of EC nanoparticles adsorbed at the interface. Below the CCC, the adsorption flux to the alkane-water interfaces is accelerated because of enhanced rearrangement of adsorbed particles − a feature which is not observed in the case of air-water interface. Above the CCC, interface rearrangement is delayed projected in surface blocking. Therefore, a decay in the adsorption flux is observed for both alkane-water and air-water interfaces. These studies provide the required information to conclude that even under coagulation conditions (>CCC), adsorption of single EC nanoparticles controls the dynamics of adsorption.

Irreversible adsorption of nanoparticles to oil-water and air-water interfaces is a necessary but not sufficient condition for generating stable so-called Pickering emulsions and foams. Pickering emulsions may be stabilized exclusively by EC nanoparticles. Under controlled conditions for oil volume fraction, ionic strength, and EC nanoparticle concentration, oil-in-water (O/W) or water-in-oil (W/O) emulsions are generated which have different stability. High internal phase Pickering emulsions (HIPPE) contained $75 \pm 4\%$ oil are therefore stabilized under the optimum aforementioned conditions. The generated HIPPEs are successfully templated to fabricate polymeric porous materials to be potentially used in oil-water separation applications.

In order to meet the second objective in this work, transport of EC nanoparticles through porous media under different conditions and scenarios is assessed. It is found that EC nanoparticles are transported as a conservative tracer (NaCl) at the ionic strengths below the CCC. Above the CCC, coagulation of EC nanoparticles results in clogging the pores and throats. By co-injection of EC nanoparticle suspension and gas under favorable foaming conditions (i.e., similar to those for emulsions), foam is successfully generated *in situ* invading the porous medium. The latter shows a proof-of-concept on how EC nanoparticles can be used to improve of *in situ* foam flooding technology.

8.2 Recommendations for future works

The following subjects are recommended for future studies:

- Study the mechanical properties (e.g., elasticity, tensile strength, etc.) of the fabricated polymeric porous material in this work is highly recommended. For oil spill cleanup application, for instance, it is of significant importance to know that through how many cycles it can absorb oil and how to squeeze oil out of it. Mechanical properties are also essential for commercialization purposes.

- *in situ* generation of foam by co-injection of EC nanoparticle suspension and gas is successfully demonstrated in this work. It is suggested to conduct an *in situ* foam flooding in an unsaturated glass micromodel (a porous medium) to understand the mechanism of ganglia displacement using foam.

- In practice, a field-scale displacement of ganglia from the subsurface is of practical interest. It is therefore recommended to follow a multiscale approach from core scale to field scale to examine the applicability of EC nanoparticles in mobilizing ganglia from subsurface.

- Conduct direct observations on how nanoparticles of any kind irreversibly adsorb and rearrange at a fluid interface. This assessment together with studies on emulsion stabilization will help to have a better understanding of the mechanism of Pickering emulsion stabilization.

- Measure the force between a hydrophobic surface and a fluid interface: the magnitude, long- or short-distance effectiveness, and development of a reliable model for computation. That is a need to understand how hydrophobic colloidal nanoparticles adsorb at fluid interfaces and what controls its magnitude.

References

[1] *CRC Handbook of Chemistry and Physics.* CRC Press, Taylor & francis Group, LLC, Boca Raton, FL, USA, 2015.

[2] Z. Adamczyk. Kinetics of diffusion-controlled adsorption of colloid particles and proteins. *Journal of Colloid and Interface Science*, 229(2):477 – 489, 2000.

[3] Z. Adamczyk, K. Jaszczółt, A. Michna, B. Siwek, L. Szyk-Warszyńska, and M. Zembala. Irreversible adsorption of particles on heterogeneous surfaces. *Advances in Colloid and Interface Science*, 118(13):25 – 42, 2005.

[4] M. Auset and A. A. Keller. Pore-scale visualization of colloid straining and filtration in saturated porous media using micromodels. *Water Resources Research*, 42(12):1–9, 2006.

[5] R. Aveyard, J. H. Clint, D. Nees, and V. N. Paunov. Compression and structure of monolayers of charged latex particles at air/water and octane/water interfaces. *Langmuir*, 16(4):1969–1979, 2000.

[6] L. Bergström, S. Stemme, T. Dahlfors, H. Arwin, and L. Ödberg. Spectroscopic ellipsometry characterisation and estimation of the Hamaker constant of cellulose. *Cellulose*, 6(1):1–13, 1999.

[7] M. Berka and J. A. Rice. Absolute aggregation rate constants in aggregation of kaolinite measured by simultaneous static and dynamic light scattering. *Langmuir*, 20(15):6152–6157, 2004.

[8] B. Bijeljic and M. J. Blunt. A physically-based description of dispersion in porous media. San Antonio, TX, USA, April 12-16 2006. Society of Petroleum Engineers.

[9] B. P. Binks. Particles as surfactants−similarities and differences. *Current Opinion in Colloid & Interface Science*, 7(12):21 – 41, 2002.

[10] B. P. Binks and T. S. Horozov. Aqueous foams stabilized solely by silica nanoparticles. *Angewandte Chemie International Edition*, 44(24):3722–3725, 2005.

[11] B. P. Binks and S. O. Lumsdon. Stability of oil-in-water emulsions stabilised by silica particles. *Physical Chemistry Chemical Physics*, 1:3007–3016, 1999.

[12] B. P. Binks and S. O. Lumsdon. Influence of particle wettability on the type and stability of surfactant-free emulsions. *Langmuir*, 16(23):8622–8631, 2000.

[13] R. B. Bird, W. E. Stewart, and E. N. Lightfoot. *Transport Phenomena*. John Wiley & Sons, Inc., New York, NY, USA, 1960.

[14] N. Bizmark. Dynamic surface tension as a probe of irreversible adsorption of nanoparticles at fluid-fluid interfaces. Master's thesis, University of Waterloo, 2013.

[15] N. Bizmark and M. A. Ioannidis. Effects of ionic strength on the colloidal stability and interfacial assembly of hydrophobic ethyl cellulose nanoparticles. *Langmuir*, 31(34):9282–9289, 2015.

[16] N. Bizmark, M. A. Ioannidis, and D. E. Henneke. Irreversible adsorption-driven assembly of nanoparticles at fluid interfaces revealed by a dynamic surface tension probe. *Langmuir*, 30(3):710–717, 2014.

[17] A. Böker, J. He, T. Emrick, and T. P. Russell. Self-assembly of nanoparticles at interfaces. *Soft Matter*, 3:1231–1248, 2007.

[18] T. R. Briggs. Emulsions with finely divided solids. *Journal of Industrial & Engineering Chemistry*, 13(11):1008–1010, 1921.

[19] H. J. Butt, B. Cappella, and M. Kappl. Force measurements with the atomic force microscope: Technique, interpretation and applications. *Surface Science Reports*, 59(16):1 – 152, 2005.

[20] N. R. Cameron and D. C. Sherrington. *High internal phase emulsions (HIPEs) − Structure, properties and use in polymer preparation*. Springer Berlin Heidelberg, Berlin, Heidelberg, 1996.

[21] N. R. Cameron, D. C. Sherrington, L. Albiston, and D. P. Gregory. Study of the formation of the open-cellular morphology of poly(styrene/divinylbenzene) polyHIPE materials by cryo-SEM. *Colloid and Polymer Science*, 274(6):592–595, 1996.

[22] I. Capron and B. Cathala. Surfactant-free high internal phase emulsions stabilized by cellulose nanocrystals. *Biomacromolecules*, 14(2):291–296, 2013.

[23] A. Cervantes Martinez, E. Rio, G. Delon, A. Saint-Jalmes, D. Langevin, and B. P. Binks. On the origin of the remarkable stability of aqueous foams stabilised by nanoparticles: Link with microscopic surface properties. *Soft Matter*, 4:1531–1535, 2008.

[24] M. Chappat. Some applications of emulsions. *Colloids and Surfaces A: Physicochemical and Engineering Aspects*, 91:57 – 77, 1994.

[25] I. Chatzis and F. A. L. Dullien. Dynamic immiscible displacement mechanisms in pore doublets: Theory versus experiment. *Journal of Colloid and Interface Science*, 91(1):199 – 222, 1983.

[26] I. Chatzis, N. R. Morrow, and H. T. Lim. Magnitude and detailed structure of residual oil saturation. *Society of Petroleum Engineers*, 23:311–326, 1983.

[27] K. L. Chen and M. Elimelech. Aggregation and deposition kinetics of fullerene (C_{60}) nanoparticles. *Langmuir*, 22(26):10994–11001, 2006.

[28] Y. Cheng, A. C. Samia, J. D. Meyers, I. Panagopoulos, B. Fei, and C. Burda. Highly efficient drug delivery with gold nanoparticle vectors for *in vivo* photodynamic therapy of cancer. *Journal of the American Chemical Society*, 130(32):10643–10647, 2008.

[29] A. Chengara, A. D. Nikolov, D. T. Wasan, A. Trokhymchuk, and D. Henderson. Spreading of nanofluids driven by the structural disjoining pressure gradient. *Journal of Colloid and Interface Science*, 280(1):192 – 201, 2004.

[30] S. H. Conrad, J. L. Wilson, W. R. Mason, and W. J. Peplinski. Visualization of residual organic liquid trapped in aquifers. *Water Resources Research*, 28(2):467–478, 1992.

[31] M. Y. Corapcioglu and H. Choi. Modeling colloid transport in unsaturated porous media and validation with laboratory column data. *Water Resources Research*, 32(12):3437–3449, 1996.

[32] M. M. Crowley, B. Schroeder, A. Fredersdorf, S. Obara, M. Talarico, S. Kucera, and J. W. McGinity. Physicochemical properties and mechanism of drug release from ethyl cellulose matrix tablets prepared by direct compression and hot-melt extrusion. *International Journal of Pharmaceutics*, 269(2):509 – 522, 2004.

[33] K. D. Danov and P. A. Kralchevsky. The standard free energy of surfactant adsorption at air/water and oil/water interfaces: Theoretical vs. empirical approaches. *Colloid Journal*, 74(2):172–185, 2012.

[34] M. Davidovich-Pinhas, S. Barbut, and A. G. Marangoni. Physical structure and thermal behavior of ethylcellulose. *Cellulose*, 21(5):3243–3255, 2014.

[35] A. H. Demond and A. S. Lindner. Estimation of interfacial tension between organic liquids and water. *Environmental Science & Technology*, 27(12):2318–2331, 1993.

[36] M. Destribats, S. Gineste, E. Laurichesse, H. Tanner, F. Leal-Calderon, V. Héroguez, and V. Schmitt. Pickering emulsions: What are the main parameters determining the emulsion type and interfacial properties? *Langmuir*, 30(31):9313–9326, 2014.

[37] E. Dickinson. Emulsion gels: The structuring of soft solids with protein-stabilized oil droplets. *Food Hydrocolloids*, 28(1):224 – 241, 2012.

[38] T.-A.L. Do, J.R. Mitchell, B. Wolf, and J. Vieira. Use of ethylcellulose polymers as stabilizer in fat-based food suspensions examined on the example of model reduced-fat chocolate. *Reactive and Functional Polymers*, 70(10):856 – 862, 2010.

[39] M. Dong, Q. Liu, and A. Li. Displacement mechanisms of enhanced heavy oil recovery by alkaline flooding in a micromodel. *Particuology*, 10(3):298 – 305, 2012.

[40] K. Du, E. Glogowski, T. Emrick, T. P. Russell, and A. D. Dinsmore. Adsorption energy of nano- and microparticles at liquid-liquid interfaces. *Langmuir*, 26(15):12518–12522, 2010.

[41] A. V. Dudchenko, J. Rolf, L. Shi, L. Olivas, W. Duan, and D. Jassby. Coupling underwater superoleophobic membranes with magnetic Pickering emulsions for fouling-free separation of crude oil/water mixtures: An experimental and theoretical study. *ACS Nano*, 9(10):9930–9941, 2015.

[42] A. A. Eftekhari, R. Krastev, and R. Farajzadeh. Foam stabilized by fly ash nanoparticles for enhancing oil recovery. *Industrial & Engineering Chemistry Research*, 54(50):12482–12491, 2015.

[43] R. Enouy, M. Li, M. A. Ioannidis, and A. J. A. Unger. Gas exsolution and flow during supersaturated water injection in porous media: II. column experiments and continuum modeling. *Advances in Water Resources*, 34(1):15 – 25, 2011.

[44] D. A. Espinoza, F. M. Caldelas, K. P. Johnston, S. L. Bryant, and C. Huh. Nanoparticle-stabilized supercritical CO_2 foams for potential mobility control applications. In *SPE Improved Oil Recovery Symposium*, Tulsa, OK, USA, April 24-28 2010. Society of Petroleum Engineers.

[45] D. F. Evans and H. Wennerström. *The Colloidal Domain: Where Physics, Chemistry, Biology, and Technology Meet*. Wiley-VCH, New York, NY, 1999.

[46] R. Farajzadeh, A. Andrianov, R. Krastev, G. J. Hirasaki, and W. R. Rossen. Foam-oil interaction in porous media: Implications for foam assisted enhanced oil recovery. *Advances in Colloid and Interface Science*, 183-184:1 – 13, 2012.

[47] S. Ferdous, M. A. Ioannidis, and D. E. Henneke. Effects of temperature, pH, and ionic strength on the adsorption of nanoparticles at liquid-liquid interfaces. *Journal of Nanoparticle Research*, 14(5):850–861, 2012.

[48] Scientific Fisher. Ethyl cellulose, ethoxyl, content 48%, 300mpass, acros organics, 2017. https://www.fishersci.com/shop/products/ethyl-cellulose-ethoxyl-content-48-300mpass-acros-organics-4/p-3737986.

[49] A. Flaaten, Q. P. Nguyen, G. A. Pope, and J. Zhang. A systematic laboratory approach to low-cost, high-performance chemical flooding. *SPE Reservoir Evaluation & Engineering*, 12:713–723, 2009.

[50] S. Fouilloux, F. Malloggi, J. Daillant, and A. Thill. Aging mechanism in model Pickering emulsion. *Soft Matter*, 12:900–904, 2016.

[51] D. J. French, P. Taylor, J. Fowler, and P. S. Clegg. Making and breaking bridges in a Pickering emulsion. *Journal of Colloid and Interface Science*, 441:30 – 38, 2015.

[52] Y. Fukumori, H. Ichikawa, Y. Yamaoka, E. Akaho, Y. Takeuchi, T. Fukuda, Y. Kanamori, and Y. Osako. Microgranulation and encapsulation of pulverized pharmaceutical powders with ethyl cellulose by the wurster process. *Chemical & Pharmaceutical Bulletin*, 39(7):1806–1812, 1991.

[53] P. Gaganis, E. D. Skouras, M. A. Theodoropoulou, C. D. Tsakiroglou, and V. N. Burganos. On the evaluation of dispersion coefficients from visualization experiments in artificial porous media. *Journal of Hydrology*, 307(1):79 – 91, 2005.

[54] J. T. Geller and J. R. Hunt. Mass transfer from nonaqueous phase organic liquids in water-saturated porous media. *Water Resources Research*, 29(4):833–845, 1993.

[55] P. Ghosh, G. Han, M. De, C. K. Kim, and V. M. Rotello. Gold nanoparticles in delivery applications. *Advanced Drug Delivery Reviews*, 60(11):1307 – 1315, 2008.

[56] N. Giordano and J. T. Cheng. Microfluid mechanics: Progress and opportunities. *Journal of Physics: Condensed Matter*, 13(15):R271–R295, 2001.

[57] A. Goebel and K. Lunkenheimer. Interfacial tension of the water/n-alkane interface. *Langmuir*, 13(2):369–372, 1997.

[58] K. Golemanov, S. Tcholakova, P. A. Kralchevsky, K. P. Ananthapadmanabhan, and A. Lips. Latex-particle-stabilized emulsions of anti-bancroft type. *Langmuir*, 22(11):4968–4977, 2006.

[59] Urs T. Gonzenbach, A. R. Studart, E. Tervoort, and L. J. Gauckler. Ultrastable particle-stabilized foams. *Angewandte Chemie International Edition*, 45(21):3526–3530, 2006.

[60] J. T. Gostick, M. A. Ioannidis, M. W. Fowler, and M. D. Pritzker. Wettability and capillary behavior of fibrous gas diffusion media for polymer electrolyte membrane fuel cells. *Journal of Power Sources*, 194(1):433 – 444, 2009.

[61] D. W. Green and G. P. Willhite. *Enhanced Oil Recovery*. Society of Petroleum Engineering Inc., Richardson, TX, USA, 1998.

[62] D. Grolimund and M. Borkovec. Release and transport of colloidal particles in natural porous media: 1. modeling. *Water Resources Research*, 37(3):559–570, 2001.

[63] L. Hendraningrat, S. Li, and O. Torster. A coreflood investigation of nanofluid enhanced oil recovery. *Journal of Petroleum Science and Engineering*, 111:128 – 138, 2013.

[64] L. Hendraningrat and L. Shidong. A glass micromodel experimental study of hydrophilic nanoparticles retention for EOR project. In *SPE Russian Oil and Gas Exploration and Production Technical Conference and Exhibition*, Moscow, Russia, October 16-18 2012.

[65] J. J. L. Higdon. Multiphase flow in porous media. *Journal of Fluid Mechanics*, 730:1–4, 9 2013.

[66] G. Hirasaki, C. A. Miller, and M. Puerto. Recent advances in surfactant EOR. *SPE Journal*, 16:889–907, 2011.

[67] G. J Hirasaki. Wettability: Fundamentals and surface forces. *SPE Formation Evaluation*, 6(2):217–226, 1991.

[68] R. Hogg, T. W. Healy, and D. W. Fuerstenau. Mutual coagulation of colloidal dispersions. *Transactions of the Faraday Society*, 62:1638–1651, 1966.

[69] H. Holthoff, S. U. Egelhaaf, M. Borkovec, P. Schurtenberger, and H. Sticher. Coagulation rate measurements of colloidal particles by simultaneous static and dynamic light scattering. *Langmuir*, 12(23):5541–5549, 1996.

[70] T. S. Horozov. Foams and foam films stabilised by solid particles. *Current Opinion in Colloid & Interface Science*, 13(3):134 – 140, 2008.

[71] T. S. Horozov, R. Aveyard, B. P. Binks, and J. H. Clint. Structure and stability of silica particle monolayers at horizontal and vertical octane-water interfaces. *Langmuir*, 21(16):7405–7412, 2005.

[72] T. S. Horozov, R. Aveyard, J. H. Clint, and B. P. Binks. Order-disorder transition in monolayers of modified monodisperse silica particles at the octane-water interface. *Langmuir*, 19(7):2822–2829, 2003.

[73] T. S. Horozov and B. P. Binks. Particle-stabilized emulsions: A bilayer or a bridging monolayer? *Angewandte Chemie International Edition*, 45(5):773–776, 2006.

[74] J. Hou, X. Feng, J. Masliyah, and Z. Xu. Understanding interfacial behavior of ethylcellulose at the waterdiluted bitumen interface. *Energy & Fuels*, 26(3):1740–1745, 2012.

[75] J. R. Hunt, N. Sitar, and K. S. Udell. Nonaqueous phase liquid transport and cleanup: 1. analysis of mechanisms. *Water Resources Research*, 24(8):1247–1258, 1988.

[76] T. N. Hunter, R. J. Pugh, G. V. Franks, and G. J. Jameson. The role of particles in stabilising foams and emulsions. *Advances in Colloid and Interface Science*, 137(2):57 – 81, 2008.

[77] M. A. Ioannidis, I. Chatzis, and A. C. Payatakes. A mercury porosimeter for investigating capillary phenomena and microdisplacement mechanisms in capillary networks. *Journal of Colloid and Interface Science*, 143(1):22 – 36, 1991.

[78] L. Isa, E. Amstad, K. Schwenke, E. Del Gado, P. Ilg, M. Kroger, and E. Reimhult. Adsorption of core-shell nanoparticles at liquid-liquid interfaces. *Soft Matter*, 7:7663–7675, 2011.

[79] J. Israelachvili and R. Pashley. The hydrophobic interaction is long range, decaying exponentially with distance. *Nature*, 300:341–342, 1982.

[80] J. N. Israelachvili. *Intermolecular and Surface Forces*. American Press Inc., San Diego, CA, USA, 1992.

[81] P. Jiemvarangkul, W. X. Zhang, and H. L. Lien. Enhanced transport of polyelectrolyte stabilized nanoscale zero-valent iron (nZVI) in porous media. *Chemical Engineering Journal*, 170(23):482 – 491, 2011.

[82] H. Jin, W. Zhou, J. Cao, S. D. Stoyanov, T. B. J. Blijdenstein, P. W. N. de Groot, L. N. Arnaudov, and E. G. Pelan. Super stable foams stabilized by colloidal ethyl cellulose particles. *Soft Matter*, 8:2194–2205, 2012.

[83] P. R. Johnson and M. Elimelech. Dynamics of colloid deposition in porous media: Blocking based on random sequential adsorption. *Langmuir*, 11(3):801–812, 1995.

[84] Y. Jung, Y. H. Son, J. K. Lee, T. X. Phuoc, Y. Soong, and M. K. Chyu. Rheological behavior of clay-nanoparticle hybrid-added bentonite suspensions: Specific role of hybrid additives on the gelation of clay-based fluids. *ACS Applied Materials & Interfaces*, 3(9):3515–3522, 2011.

[85] K. Kim, S. Kim, J. Ryu, J. Jeon, S. G. Jang, H. Kim, D. G. Gweon, W. B. Im, Y. Han, H. Kim, and S. Q. Choi. Processable high internal phase Pickering emulsions using depletion attraction. *Nature Communications*, 8:14305–14312, 2017.

[86] D. Klotz, K.-P. Seiler, H. Moser, and F. Neumaier. Dispersivity and velocity relationship from laboratory and field experiments. *Journal of Hydrology*, 45(3):169 – 184, 1980.

[87] C.-H. Ko, S. Bhattacharjee, and M. Elimelech. Coupled influence of colloidal and hydrodynamic interactions on the RSA dynamic blocking function for particle deposition onto packed spherical collectors. *Journal of Colloid and Interface Science*, 229(2):554 – 567, 2000.

[88] M. Kobayashi, F. Juillerat, P. Galletto, P. Bowen, and M. Borkovec. Aggregation and charging of colloidal silica particles:Effect of particle size. *Langmuir*, 21(13):5761–5769, 2005.

[89] W. Koch. Properties and uses of ethylcellulose. *Industrial & Engineering Chemistry*, 29(6):687–690, 1937.

[90] A. P. Kotula and S. L. Anna. Probing timescales for colloidal particle adsorption using slug bubbles in rectangular microchannels. *Soft Matter*, 8:10759–10772, 2012.

[91] P. A. Kralchevsky, I. B. Ivanov, K. P. Ananthapadmanabhan, and A. Lips. On the thermodynamics of particle-stabilized emulsions:Curvature effects and catastrophic phase inversion. *Langmuir*, 21(1):50–63, 2005.

[92] F. Kuhnen, K. Barmettler, S. Bhattacharjee, M. Elimelech, and R. Kretzschmar. Transport of iron oxide colloids in packed quartz sand media: Monolayer and multilayer deposition. *Journal of Colloid and Interface Science*, 231(1):32 – 41, 2000.

[93] L. W. Lake. *Enhanced Oil Recovery*. Prentice-Hall, Inc., Englewood Cliffs, NJ, USA, 1989.

[94] G. L. Langnes, J. O. Robertson Jr., and G. V. Chilingar. *Secondary Recovery and Carbonate Resevoirs*. American Elsevier Publishing Company, Inc., New York, NY, USA, 1972.

[95] M. Latil. *Enhanced Oil Recovery*. Editions Technip, Paris, France, 1980.

[96] A. D. Law, M. Auriol, D. Smith, T. S. Horozov, and D. M. A. Buzza. Self-assembly of two-dimensional colloidal clusters by tuning the hydrophobicity, composition, and packing geometry. *Physical Review Letter*, 110:138301–138305, 2013.

[97] M. H. Lee, V. Prasad, and D. Lee. Microfluidic fabrication of stable nanoparticle-shelled bubbles. *Langmuir*, 26(4):2227–2230, 2010.

[98] J. J. Lenhart and J. E. Saiers. Transport of silica colloids through unsaturated porous media:Experimental results and model comparisons. *Environmental Science & Technology*, 36(4):769–777, 2002.

[99] R. Lenormand, E. Touboul, and C. Zarcone. Numerical models and experiments on immiscible displacements in porous media. *Journal of Fluid Mechanics*, 189:165–187, 1988.

[100] R. Lenormand, C. Zarcone, and A. Sarr. Mechanisms of the displacement of one fluid by another in a network of capillary ducts. *Journal of Fluid Mechanics*, 135:337–353, 1983.

[101] J. Li, X. Xie, and S. Ghoshal. Correlation equation for predicting the single-collector contact efficiency of colloids in a horizontal flow. *Langmuir*, 31(26):7210–7219, 2015.

[102] K. Li, W. Zhang, Y. Huang, and Y. Chen. Aggregation kinetics of CeO_2 nanoparticles in KCl and $CaCl_2$ solutions: Measurements and modeling. *Journal of Nanoparticle Research*, 13(12):6483–6491, 2011.

[103] Y. Liang, N. Hilal, P. Langston, and V. Starov. Interaction forces between colloidal particles in liquid: Theory and experiment. *Advances in Colloid and Interface Science*, 134-135:151–166, 2007.

[104] V. A. Lifton. Microfluidics: An enabling screening technology for enhanced oil recovery (EOR). *Lab on a Chip*, 16:1777–1796, 2016.

[105] F. Lin, L. He, J. Hou, J. Masliyah, and Z. Xu. Role of ethyl cellulose in bitumen extraction from oil sands ores using an aqueous-nonaqueous hybrid process. *Energy & Fuels*, 30(1):121–129, 2016.

[106] F. Lin, J. Suda, and A. Yeung. A small point regarding DLVO coagulation conditions. *Journal of Colloid and Interface Science*, 430:113 – 115, 2014.

[107] K. J. Lissant. The geometry of high-internal-phase-ratio emulsions. *Journal of Colloid and Interface Science*, 22(5):462 – 468, 1966.

[108] D. Luo, F. Wang, J. Zhu, F. Cao, Y. Liu, X. Li, R. C. Willson, Z. Yang, C.-W. Chu, and Z. Ren. Nanofluid of graphene-based amphiphilic Janus nanosheets for tertiary or enhanced oil recovery: High performance at low concentration. *Proceedings of the National Academy of Sciences*, 113(28):7711–7716, 2016.

[109] H. Lyklema. Pair interactions. In J. Lyklema, editor, *Volume IV: Particulate Colloids*, volume 4 of *Fundamentals of Interface and Colloid Science*, pages 3.1 – 3.190. Academic Press, 2005.

[110] C. G. Malmberg and A. A. Maryott. Dielectric constant of water from 0° to 100°C. *Journal of Research of the National Bureau of Standards*, 56(1):1, 1956.

[111] M. Marquis, V. Alix, I. Capron, S. Cuenot, and A. Zykwinska. Microfluidic encapsulation of Pickering oil microdroplets into alginate microgels for lipophilic compound delivery. *ACS Biomaterials Science & Engineering*, 2(4):535–543, 2016.

[112] F. Martínez-López, M. A. Cabrerizo-Vílchez, and R. Hidalgo-Álvarez. Colloidal interaction at the air-liquid interface. *Journal of Colloid and Interface Science*, 232(2):303 – 310, 2000.

[113] L. N. McCartney and S. Levine. An improvement on derjaguin's expression at small potentials for the double layer interaction energy of two spherical colloidal particles. *Journal of Colloid and Interface Science*, 30(3):345 – 354, 1969.

[114] E. E. Meyer, K. J. Rosenberg, and J. Israelachvili. Recent progress in understanding hydrophobic interactions. *Proceedings of the National Academy of Sciences*, 103(43):15739–15746, 2006.

[115] R. Mezzenga, J. Ruokolainen, G. H. Fredrickson, E. J. Kramer, D. Moses, A. J. Heeger, and O. Ikkala. Templating organic semiconductors via self-assembly of polymer colloids. *Science*, 299:1872–1874, 2003.

[116] B. R. Midmore. Preparation of a novel silica-stabilized oil/water emulsion. *Colloids and Surfaces A: Physicochemical and Engineering Aspects*, 132(2):257 – 265, 1998.

[117] C. Miesch, I. Kosif, E. Lee, J. K. Kim, T. P. Russell, R. C. Hayward, and T. Emrick. Nanoparticle-stabilized double emulsions and compressed droplets. *Angewandte Chemie International Edition*, 51(1):145–149, 2012.

[118] J. Milter. *Improved oil recovery in chalk.* PhD thesis, University of Bergen, 1996.

[119] D. Mo, B. Jia, J. Yu, N. Liu, and R. Lee. Study nanoparticle-stabilized CO_2 foam for oil recovery at different pressure, temperature, and rock samples. In *SPE Improved Oil Recovery Symposium*, Tulsa, OK, USA, April 12-16 2014. Society of Petroleum Engineers.

[120] F. H. Müller. Influence of the solvent on dipole-moments. *Transactions of the Faraday Society*, 30:729–734, 1934.

[121] M. K. Mulligan and J. P. Rothstein. Deformation and breakup of micro- and nanoparticle stabilized droplets in microfluidic extensional flows. *Langmuir*, 27(16):9760–9768, 2011.

[122] B. S. Murray, K. Durga, P. W. N. de Groot, A. Kakoulli, and S. D. Stoyanov. Preparation and characterization of the foam-stabilizing properties of cellulose-ethyl cellulose complexes for use in foods. *Journal of Agricultural and Food Chemistry*, 59(24):13277–13288, 2011.

[123] K. J. Mysels. *Introduction to Colloid Chemistry.* Interscience Publishers, New York, NY, USA, 1959.

[124] B. Neirinck, J. Fransaer, O. VanderBiest, and J. Vleugels. Production of porous materials through consolidation of Pickering emulsions. *Advanced Engineering Materials*, 9(1-2):57–59, 2007.

[125] A. Nelson, D. Wang, K. Koynov, and L. Isa. A multiscale approach to the adsorption of core-shell nanoparticles at fluid interfaces. *Soft Matter*, 11:118–129, 2015.

[126] K. E. Nelson and T. R. Ginn. Colloid filtration theory and the happel sphere-in-cell model revisited with direct numerical simulation of colloids. *Langmuir*, 21(6):2173–2184, 2005.

[127] P. Nguyen, H. Fadaei, and D. Sinton. Pore-scale assessment of nanoparticle-stabilized co_2 foam for enhanced oil recovery. *Energy & Fuels*, 28(10):6221–6227, 2014.

[128] S. Okushima, T. Nisisako, T. Torii, and T. Higuchi. Controlled production of monodisperse double emulsions by two-step droplet breakup in microfluidic devices. *Langmuir*, 20(23):9905–9908, 2004.

[129] G. F. Paciotti, L. Myer, D. Weinreich, D. Goia, N. Pavel, R. E. McLaughlin, and L. Tamarkin. Colloidal gold: A novel nanoparticle vector for tumor directed drug delivery. *Drug Delivery*, 11(3):169–183, 2004.

[130] A. B. Pawar, M. Caggioni, R. Ergun, R. W. Hartel, and P. T. Spicer. Arrested coalescence in Pickering emulsions. *Soft Matter*, 7:7710–7716, 2011.

[131] A. C. Payatakes and M. M. Dias. Immiscible microdisplacement and ganglion dynamics in porous media. *Reviews in Chemical Engineering*, 2:85–174, 1984.

[132] A. C. Payatakes, K. M. Ng, and R. W. Flumerfelt. Oil ganglion dynamics during immiscible displacement: Model formulation. *AIChE Journal*, 26(3):430–443, 1980.

[133] J. Peng, Q. Liu, Z. Xu, and J. Masliyah. Synthesis of interfacially active and magnetically responsive nanoparticles for multiphase separation applications. *Advanced Functional Materials*, 22(8):1732–1740, 2012.

[134] T. Phenrat, F. Fagerlund, T. Illangasekare, G. V. Lowry, and R. D. Tilton. Polymer-modified Fe^0 nanoparticles target entrapped NAPL in two dimensional porous media: Effect of particle concentration, napl saturation, and injection strategy. *Environmental Science & Technology*, 45(14):6102–6109, 2011.

[135] S. U. Pickering. Cxcvi.-emulsions. *Journal of Chemical Society, Transactions*, 91:2001–2021, 1907.

[136] P. Pieranski. Two-dimensional interfacial colloidal crystals. *Physical Review Letters*, 45:569–572, 1980.

[137] C. Pinto Reis, R. J. Neufeld, A. J. Ribeiro, and F. Veiga. Nanoencapsulation i. methods for preparation of drug-loaded polymeric nanoparticles. *Nanomedicine: Nanotechnology, Biology and Medicine*, 2(1):8 – 21, 2006.

[138] S. Podzimek. *Light Scattering, Size Exclusion Chromatography, and Asymmetric Flow Field Flow Fractionation: Powerful Tools for the Characterization of Polymers, Proteins and Nanoparticles.* John Wiley & Sons, Inc., Hoboken, NJ, USA, 2011.

[139] C. Priest, M. D. Reid, and C. P. Whitby. Formation and stability of nanoparticle-stabilised oil-in-water emulsions in a microfluidic chip. *Journal of Colloid and Interface Science*, 363(1):301 – 306, 2011.

[140] A. Rabbani. Pore size distribution of 2D porous media images, 2015. http://www.mathworks.com/matlabcentral/fileexchange/50623-pore-size-distribution-of-2d-porous-media-images.

[141] W. Ramsden. Separation of solids in the surface-layers of solutions and 'suspensions' (observations on surface-membranes, bubbles, emulsions, and mechanical coagulation). – preliminary account. *Proceedings of the Royal Society of London*, 72:156–164, 1903.

[142] T. Raychoudhury, G. Naja, and S. Ghoshal. Assessment of transport of two polyelectrolyte-stabilized zero-valent iron nanoparticles in porous media. *Journal of Contaminant Hydrology*, 118(34):143 – 151, 2010.

[143] M. Retsch, Z. Zhou, S. Rivera, M. Kappl, X. S. Zhao, U. Jonas, and Q. Li. Fabrication of large-area, transferable colloidal monolayers utilizing self-assembly at the air/water interface. *Macromolecular Chemistry and Physics*, 210(3-4):230–241, 2009.

[144] L. Ridel, M.-A. Bolzinger, N. Gilon-Delepine, P.-Y. Dugas, and Y. Chevalier. Pickering emulsions stabilized by charged nanoparticles. *Soft Matter*, 12:7564–7576, 2016.

[145] M. Sahimi, B. D. Hughes, L. E. Scriven, and H. T. Davis. Dispersion in flow through porous media − I. One-phase flow. *Chemical Engineering Science*, 41(8):2103 – 2122, 1986.

[146] N. B. Saleh, L. D. Pfefferle, and M. Elimelech. Aggregation kinetics of multiwalled carbon nanotubes in aquatic systems: Measurements and environmental implications. *Environmental Science & Technology*, 42(21):7963–7969, 2008.

[147] J. S. Sander, L. Isa, P. A. Ruhs, P. Fischer, and A. R. Studart. Stabilization mechanism of double emulsions made by microfluidics. *Soft Matter*, 8:11471–11477, 2012.

[148] A. Schafer, H. Harms, and A. J. B. Zehnder. Bacterial accumulation at the air-water interface. *Environmental Science & Technology*, 32(23):3704–3712, 1998.

[149] L. L. Schramm. *Emulsions, Foams, and Suspensions: Fundamentals and Applications*. Wiley-VCH, Weinheim, Germany, 2005.

[150] M. Schudel, S. H. Behrens, H. Holthoff, R. Kretzschmar, and M. Borkovec. Absolute aggregation rate constants of hematite particles in aqueous suspensions: A comparison of two different surface morphologies. *Journal of Colloid and Interface Science*, 196(2):241 – 253, 1997.

[151] D. Schulze-Makuch. Longitudinal dispersivity data and implications for scaling behavior. *Ground Water*, 43(3):443–456, 2005.

[152] D. Segets, R. Marczak, S. Schäfer, C. Paula, J. F. Gnichwitz, A. Hirsch, and W. Peukert. Experimental and theoretical studies of the colloidal stability of nanoparticles – a general interpretation based on stability maps. *ACS Nano*, 5(6):4658–4669, 2011.

[153] J. S. Selker, C. K. Keller, and J. T. McCord. *Vadose Zone Processes*. CRC Press LLC, USA, 1999.

[154] D. O. Shah, editor. *Surface Phenomena in Enhanced Oil Recovery*. Plenum Press, New York, NY, USA, 1981.

[155] H. ShamsiJazeyi, C. A. Miller, M. S. Wong, J. M. Tour, and R. Verduzco. Polymer-coated nanoparticles for enhanced oil recovery. *Journal of Applied Polymer Science*, 131:40576–40588, 2014.

[156] R. Sharmin, M. A. Ioannidis, and R. L. Legge. Effect of nonionic surfactant partitioning on the dissolution kinetics of residual perchloroethylene in a model porous medium. *Journal of Contaminant Hydrology*, 82(12):145 – 164, 2006.

[157] X. Shen, L. Zhao, Y. Ding, B. Liu, H. Zeng, L. Zhong, and X. Li. Foam, a promising vehicle to deliver nanoparticles for vadose zone remediation. *Journal of Hazardous Materials*, 186(23):1773 – 1780, 2011.

[158] Sigma-Aldrich. Ethyl cellulose, 2017. http://www.sigmaaldrich.com/catalog/search?term=9004-57-3&interface=CAS%20No.&N=0+&mode=partialmax&lang=en&region=CA&focus=product.

[159] R. Singh and K. K. Mohanty. Foams stabilized by in-situ surface-activated nanoparticles in bulk and porous media. *SPE Journal*, 21(1):121–130, 2016.

[160] R. Singh and K. K. Mohanty. Foam flow in a layered, heterogeneous porous medium: A visualization study. *Fuel*, 197:58 – 69, 2017.

[161] I. M. Smallwood. n-heptance. In Ian M. Smallwood, editor, *Handbook of Organic Solvent Properties*, pages 11 – 13. Butterworth-Heinemann, Oxford, 1996.

[162] I. M. Smallwood. Water. In Ian M. Smallwood, editor, *Handbook of Organic Solvent Properties*, pages 301 – 303. Butterworth-Heinemann, Oxford, 1996.

[163] D. Stamou, C. Duschl, and D. Johannsmann. Long-range attraction between colloidal spheres at the air-water interface: The consequence of an irregular meniscus. *Physical Review E*, 62:5263–5272, 2000.

[164] E. J. Stancik, M. Kouhkan, and G. G. Fuller. Coalescence of particle-laden fluid interfaces. *Langmuir*, 20(1):90–94, 2004.

[165] A. Stocco, T. Mokhtari, G. Haseloff, A. Erbe, and R. Sigel. Evanescent-wave dynamic light scattering at an oil-water interface: Diffusion of interface-adsorbed colloids. *Physical Review E*, 83:011601–0116011, 2011.

[166] R. J. Stokes and D. F. Evans. *Fundamentals of Interfacial Engineering*. Wiley-VCH Inc., New York, NY, 1997.

[167] Q. Sun, Z. Li, S. Li, L. Jiang, J. Wang, and P. Wang. Utilization of surfactant-stabilized foam for enhanced oil recovery by adding nanoparticles. *Energy & Fuels*, 28(4):2384–2394, 2014.

[168] Q. Sun, N. Zhang, Z. Li, and Y. Wang. Nanoparticle-stabilized foam for effective displacement in porous media and enhanced oil recovery. *Energy Technology*, 4(9):1053–1063, 2016.

[169] T. F. Tadros. *Emulsion Formation, Stability, and Rheology*. Wiley-VCH Verlag GmbH & Co. KGaA, 2013.

[170] D. E. Tambe and M. M. Sharma. Factors controlling the stability of colloid-stabilized emulsions. *Journal of Colloid and Interface Science*, 157(1):244 – 253, 1993.

[171] D. E. Tambe and M. M. Sharma. The effect of colloidal particles on fluid-fluid interfacial properties and emulsion stability. *Advances in Colloid and Interface Science*, 52:1 – 63, 1994.

[172] N. Toride, F. J. Leij, and M. T. V. Genuchten. *The CXTFIT Code for Estimating Transport Parameters from Laboratory or Field Tracer Experiments, Version 2.0.* U.S. Salinity Laboratory, USDA: Riverside, CA, USA, 1995.

[173] J. Tóth, editor. *Adsorption: Theory, Modeling, and Analysis.* Marcel Dekker, 2002.

[174] N. Tufenkji and M. Elimelech. Correlation equation for predicting single-collector efficiency in physicochemical filtration in saturated porous media. *Environmental Science & Technology*, 38(2):529–536, 2004.

[175] N. Tufenkji, J. A. Redman, and M. Elimelech. Interpreting deposition patterns of microbial particles in laboratory-scale column experiments. *Environmental Science & Technology*, 37(3):616–623, 2003.

[176] Z. Urbán-Morlán, S. E. Mendoza-Elvira, R. S. Hernández-Cerón, S. Alcalá-Alcalá, H. Ramírez-Mendoza, A. Ciprián-Carrasco, E. Piñón Segundo, and D. Quintanar-Guerrero. Preparation of ethyl cellulose nanoparticles by solvent-displacement using the conventional method and a recirculation system. *Journal of the Mexican Chemical Society*, 59:173 – 180, 2015.

[177] N. B. Vargaftik, B. N. Volkov, and L. D. Voljak. International tables of the surface tension of water. *Journal of Physical and Chemical Reference Data*, 12(3):817–820, 1983.

[178] C. Vauthier and K. Bouchemal. Methods for the preparation and manufacture of polymeric nanoparticles. *Pharmaceutical Research*, 26(5):1025–1058, 2009.

[179] E. D. Vecchia, M. Luna, and R. Sethi. Transport in porous media of highly concentrated iron micro- and nanoparticles in the presence of xanthan gum. *Environmental Science & Technology*, 43(23):8942–8947, 2009.

[180] E. Vignati, R. Piazza, and T. P. Lockhart. Pickering emulsions: interfacial tension, colloidal layer morphology, and trapped-particle motion. *Langmuir*, 19(17):6650–6656, 2003.

[181] P. Wachsmann and A. Lamprecht. Ethylcellulose nanoparticles with bimodal size distribution as precursors for the production of very small nanoparticles. *Drug Development and Industrial Pharmacy*, 41(7):1165–1171, 2015.

[182] J. Wan, T. K. Tokunaga, C. F. Tsang, and G. S. Bodvarsson. Improved glass micromodel methods for studies of flow and transport in fractured porous media. *Water Resources Research*, 32(7):1955–1964, 1996.

[183] Q. Wang, J. H. Lee, S. W. Jeong, A. Jang, S. Lee, and H. Choi. Mobilization and deposition of iron nano and sub-micrometer particles in porous media: A glass micromodel study. *Journal of Hazardous Materials*, 192(3):1466 – 1475, 2011.

[184] S. Whitaker. Flow in porous media I: A theoretical derivation of Darcy's law. *Transport in Porous Media*, 1(1):3–25, 1986.

[185] L. R. White. On the Deryaguin approximation for the interaction of macrobodies. *Journal of Colloid and Interface Science*, 95(1):286 – 288, 1983.

[186] Ch. Wohlfarth. *Dielectric constant of decane*, pages 469–470. Springer Berlin Heidelberg, Berlin, Heidelberg, Germany, 2008.

[187] K. Wojciechowski. Surface activity of saponin from quillaja bark at the air/water and oil/water interfaces. *Colloids and Surfaces B: Biointerfaces*, 108:95 – 102, 2013.

[188] M. W. Wong, M. J. Frisch, and K. B. Wiberg. Solvent effects. 1. the mediation of electrostatic effects by solvents. *Journal of the American Chemical Society*, 113(13):4776–4782, 1991.

[189] Z. Xue, K. Panthi, Y. Fei, K. P. Johnston, and K. K. Mohanty. CO_2-soluble ionic surfactants and CO_2 foams for high-temperature and high-salinity sandstone reservoirs. *Energy & Fuels*, 29(9):5750–5760, 2015.

[190] H. Yang, Y. Xie, D. Han, W. Mao, W. Cai, and X. Guo. A facile route to synthesize porous ethyl cellulose spheres loaded with superparamagnetic iron oxide nanoparticles. *Colloid and Polymer Science*, 293(7):1915–1922, 2015.

[191] K.-M. Yao, M. T. Habibian, and C. R. O'Melia. Water and waste water filtration. concepts and applications. *Environmental Science & Technology*, 5(11):1105–1112, 1971.

[192] R. H. Yoon, D. H. Flinn, and Y. I. Rabinovich. Hydrophobic interactions between dissimilar surfaces. *Journal of Colloid and Interface Science*, 185(2):363 – 370, 1997.

[193] M. Zanini and L. Isa. Particle contact angles at fluid interfaces: Pushing the boundary beyond hard uniform spherical colloids. *Journal of Physics: Condensed Matter*, 28(31):313002–313026, 2016.

[194] S. Zeppieri, J. Rodríguez, and A. L. López de Ramos. Interfacial tension of alkane + water systems. *Journal of Chemical & Engineering Data*, 46(5):1086–1088, 2001.

[195] H. Zhang, A. Nikolov, and D. Wasan. Enhanced oil recovery (EOR) using nanoparticle dispersions: Underlying mechanism and imbibition experiments. *Energy & Fuels*, 28(5):3002–3009, 2014.

[196] Q. Zhang, N. K. Karadimitriou, S. M. Hassanizadeh, P. J. Kleingeld, and A. Imhof. Study of colloids transport during two-phase flow using a novel polydimethylsiloxane micro-model. *Journal of Colloid and Interface Science*, 401:141 – 147, 2013.

[197] Y. Zhang, A. Shitta, J. C. Meredith, and S. H. Behrens. Bubble meets droplet: Particle-assisted reconfiguration of wetting morphologies in colloidal multiphase systems. *Small*, 12(24):3309–3319, 2016.

[198] S. Zou, Y. Yang, H. Liu, and C. Wang. Synergistic stabilization and tunable structures of Pickering high internal phase emulsions by nanoparticles and surfactants. *Colloids and Surfaces A: Physicochemical and Engineering Aspects*, 436:1 – 9, 2013.

APPENDICES

Appendix A

DLVO Derivations

Derjaguin approximation for nanoparticles at fluid interfaces

Derjaguin approximation is written [112] for nanoparticles adsorbed at a fluid interface shown schematically in Figure A.1, to find out the interaction energy between two spherical particles ($\Phi^{sphere-sphere}$).
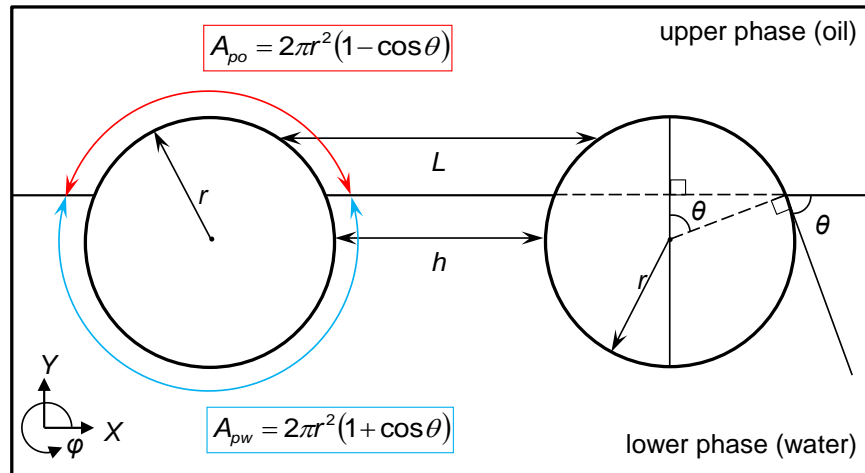

Figure A.1: Two EC nanoparticles interacting at oil-water interface.

$$\Phi^{sphere-sphere}(h) = \iint_S F^{flat-flat}(L)dS \qquad (A.1)$$

$F^{flat-flat}$ represents interaction forces between two parallel, infinite, flat surfaces. In a Cartesian geometry, Derjaguin approximation can be written as follows [185]

$$\Phi^{sphere-sphere}(h) = \iint F^{flat-flat}(L)dXdY \tag{A.2}$$

where $L = h + \frac{\lambda_1}{2}X^2 + \frac{\lambda_2}{2}Y^2$ (λ_1 and λ_2 are constants) [185] and the domain for both of X and Y is $(-\infty, +\infty)$. For nanoparticles interacting at the interface, $Y-$coordinate is splitted into two regions: lower phase (from $-\infty$ to the interface) and upper phase (from interface to $+\infty$). Eq. A.2 is then written as follows

$$\Phi^{sphere-sphere}(h) =$$

$$\int_{-\infty}^{+\infty} dX \left[\int_{-\infty}^{r\cos\theta} F^{flat-flat}\left(h+\frac{\lambda_1}{2}X^2+\frac{\lambda_2}{2}Y^2\right)dY + \int_{r\cos\theta}^{+\infty} F'^{flat-flat}\left(h+\frac{\lambda_1}{2}X^2+\frac{\lambda_2}{2}Y^2\right)dY \right] \tag{A.3}$$

The first and second term in the bracket in Eq. A.3 represent the interactions in the lower phase (water) and in the upper phase (oil), respectively. By defining two new variables $u^2 \equiv \frac{\lambda_1}{2}X^2$ and $v^2 \equiv \frac{\lambda_2}{2}Y^2$, Eq. A.3 is written as follows

$$\Phi^{sphere-sphere}(h) =$$

$$\frac{2}{\sqrt{\lambda_1\lambda_2}} \int_{-\infty}^{+\infty} du \left[\int_{-\infty}^{r\sqrt{\lambda_2/2}\cos\theta} F^{flat-flat}\left(h+u^2+v^2\right)dv + \int_{r\sqrt{\lambda_2/2}\cos\theta}^{+\infty} F'^{flat-flat}\left(h+u^2+v^2\right)dv \right] \tag{A.4}$$

Transferring Eq. A.4 to a polar coordinate system ($u = \xi\cos\varphi$, $v = \xi\sin\varphi$, and $dudv = \xi d\xi d\varphi$), we obtain

$$\Phi^{sphere-sphere}(h) =$$

$$\frac{2}{\sqrt{\lambda_1\lambda_2}} \left[\int_{\pi/2-\theta}^{\pi/2+\theta} d\varphi \int_{0}^{+\infty} F'^{flat-flat}\left(h + \xi^2\right)\xi d\xi + \int_{\pi/2+\theta}^{5\pi/2-\theta} d\varphi \int_{0}^{+\infty} F^{flat-flat}\left(h + \xi^2\right)\xi d\xi \right] \tag{A.5}$$

In Eq. A.5, the first and second term in the bracket represent the interactions in the upper phase (oil) and in the lower phase (water), respectively. Eq. A.5 simplifies to

$$\Phi^{sphere-sphere}(h) =$$

$$\frac{2}{\sqrt{\lambda_1\lambda_2}} \left[2\theta \int_{0}^{+\infty} F'^{flat-flat}\left(h + \xi^2\right)\xi d\xi + 2(\pi - \theta) \int_{0}^{+\infty} F^{flat-flat}\left(h + \xi^2\right)\xi d\xi \right] \tag{A.6}$$

133

For a given separation distance (h), we define $l \equiv h + \xi^2 \Rightarrow dl = 2\xi d\xi$, thus

$$\Phi^{sphere-sphere}(h) = \frac{2}{\sqrt{\lambda_1 \lambda_2}} \left[\theta \int_h^{+\infty} F'^{flat-flat}(l)dl + (\pi - \theta) \int_h^{+\infty} F^{flat-flat}(l)dl \right] \quad (A.7)$$

For the interaction of two identical nanoparticles with a radius of r we have $\lambda_1 \lambda_2 = 4/r^2$ [185]. Therefore, Derjaguin approximation for particles interacting at an interface is obtained from

$$\Phi^{sphere-sphere}(h) = r \left[\theta \int_h^{+\infty} F'^{flat-flat}(l)dl + (\pi - \theta) \int_h^{+\infty} F^{flat-flat}(l)dl \right] \quad (A.8)$$

Allowing $F^{flat-flat}$ and $F'^{flat-flat}$ to be $F^{W\,flat-flat}$ and $F^{O\,flat-flat}$, respectively, we obtain the following equations for van der Waals, hydrophobic, and electrostatic interactions in water or oil. Interaction forces between two parallel, infinite, flat surfaces can be found elsewhere [45, 68, 113, 192].

$$\Phi^O_{vdW} = -r\theta \frac{H_{121}}{12\pi h} \quad (A.9)$$

$$\Phi^W_{vdW} = -r(\pi - \theta) \frac{H_{131}}{12\pi h} \quad (A.10)$$

$$\Phi^W_{hydro} = -r(\pi - \theta) \frac{K_{131}}{2\pi h} \quad (A.11)$$

$$\Phi^W_{elec} = 4(\pi - \theta)\epsilon_0 \epsilon_w r \Psi_{pw}^2 \left(1 - \frac{r}{h+2r} \right) \ln \left[1 + \frac{\exp(-\kappa h)}{1 + h/r} \right] \quad (A.12)$$

Quadrupolar capillary attraction for nanoparticles at fluid interfaces

The quadrupolar capillary interaction is computed as explained by Kralchevsky et al. [91, 163]. For two adsorbed nanoparticles of the same radius with the same amplitude of contact line undulation (H_2), the total quadrupolar capillary attraction $(\Delta\Phi_{Qcap}(h))$ is [91]

$$\Delta\Phi_{Qcap}(h) = \Phi_{Qcap}(h) - \Phi_{Qcap}(\infty) \quad (A.13)$$

where $\Phi_{Qcap}(h)$ and $\Phi_{Qcap}(\infty)$ are the surface energies associated with the meniscus distortion (i.e., undulation of the contact line) at a separation distance of h and a large separation distance $(h \to \infty)$, respectively. For the most favorable mutual orientation (i.e., $\Delta\varphi = 0$ in [91]) of the adsorbed nanoparticles, one has [91]

$$\Phi_{Qcap}(h) = \pi\gamma_0 H_2^2 (2S(\omega) - G(\omega)) \quad (A.14)$$

where $S(\omega)$ and $G(\omega)$ are found from [91]

$$S(\omega) = \frac{(1-\omega)^2}{2} \sum_{n=1}^{\infty} n[n-1-(n+1)\omega]^2 \omega^{n-2} \left(1 + \frac{2\omega^{2n}}{1-\omega^{2n}} \right) \qquad (A.15)$$

$$G(\omega) = (1-\omega)^2 \sum_{n=1}^{\infty} n[n-1-(n+1)\omega]^2 \left(\frac{2\omega^{2n-2}}{1-\omega^{2n}} \right) \qquad (A.16)$$

$$\omega \equiv \frac{1}{\left[1 + h/2r_c + \sqrt{(1+h/2r_c)^2 - 1} \right]^2} \qquad (A.17)$$

In Eq. A.17, the average radius of the contact line (r_c) is taken equal to the nanoparticle radius (r), an approximation which is valid for EC nanoparticles with a contact angle close to $90°$ [163]. $\Phi_{Qcap}(\infty)$ in Eq. A.13 is calculated from [91]

$$\Phi_{Qcap}(\infty) = 2\pi\gamma_0 H_2^2 \qquad (A.18)$$

$H_2 \cong 1$ nm and $H_2 \cong 3$ nm correspond to contact angle hysteresis of about $3°$ and $8°$, respectively, for the given EC nanoparticles adsorbed at n-C10-water interface.

Appendix B

Statistical Analyses

Statistical analysis of ζ-potential, contact angle, $|\Delta E|$ for different interfaces at different levels of ionic strength and/or EC nanoparticle concentration is reported in this appendix. It is assumed that each set of measurements has the same variance and the conclusions are based on 95% confidence interpretation.

Hypothesis test:(for pair comparisons)

Null hypothesis (H_0): No difference between the measured values at each level of ionic strength

Alternative hypothesis (H_1): There is a difference between the measured values at each level of ionic strength

Conclusion: If $t_{obs.} < T_{crt.}$, no significant difference between the measured values is observed, and thus, fail to reject the null hypothesis. If $t_{obs.} > T_{crt.}$, reject the null hypothesis and thus, a significant difference between the measured values is observed.

Table B.1: ζ-potential of EC nanoparticle suspensions at different levels of ionic strength.

ionic strength [M]	average ζ-potential [mV]	standard deviation	# of measurements
0	-59.07	1.67	6
0.01	-40.37	2.11	23
0.025	-30.49	2.52	13
0.05	-18.10	0.91	12
0.07	-16.13	1.51	17
0.1	-15.00	1.11	23

$\Downarrow$

compared pair	$t_{obs.}$	$T_{crt.}$ (from t-distribution table)
0 M vs. 0.01 M	20.03	2.05
0.01 M vs. 0.025 M	12.58	2.03
0.025 M vs. 0.05 M	16.09	2.07
0.05 M vs. 0.07 M	4.03	2.05
0.07 M vs. 0.1 M	2.75	2.02

Table B.2: contact angle measurements on EC coated substrate at different levels of ionic strength.

ionic strength [M]	average contact angle [degree]	standard deviation	# of measurements
0	71.09	0.52	5
0.025	71.47	0.77	5
0.1	71.47	0.39	5

$\Downarrow$

compared pair	$t_{obs.}$	$T_{crt.}$ (from t-distribution table)
0 M vs. 0.025 M	0.91	2.31
0 M vs. 0.1 M	1.30	2.31
0.025 M vs. 0.1 M	0	2.31

Table B.3: Factorial statistical analysis on $|\Delta E|$ computed from Eq. 2.16 (reported in Table 5.3) for n-C10-water system at different levels of ionic strength and EC nanoparticle concentration.

ionic strength [M]	EC nanoparticle concentration [g L^{-1}]	$|\Delta E| \times 10^{-4}$ [$k_B T$]	standard deviation ($\times 10^{-4}$)	# of measurements
	0.25	5.60	0.426	3
0	0.5	5.57	0.428	3
	0.75	6.30	0.940	3
	1.0	7.20	0.770	3

EC nanoparticle concentration [g L^{-1}]	ionic strength [M]	$|\Delta E| \times 10^{-4}$ [$k_B T$]	standard deviation ($\times 10^{-4}$)	# of measurements
	0	5.57	0.428	3
	0.01	8.06	1.340	3
0.5	0.025	7.23	1.230	3
	0.05	8.59	1.340	3
	0.1	5.60	0.927	3

$$\Downarrow$$

	compared pair	$t_{obs.}$	$T_{crt.}$ (from t-distribution table)
	0.25 g L^{-1} vs. 0.5 g L^{-1}	0.09	2.78
ionic	0.25 g L^{-1} vs. 0.75 g L^{-1}	1.17	2.78
strength	0.25 g L^{-1} vs. 1.0 g L^{-1}	3.15	2.78
0 M	0.5 g L^{-1} vs. 0.75 g L^{-1}	1.22	2.78
	0.5 g L^{-1} vs. 1.0 g L^{-1}	3.20	2.78
	0.75 g L^{-1} vs. 1.0 g L^{-1}	1.28	2.78
	0 M vs. 0.01 M	3.07	2.78
	0 M vs. 0.025 M	2.21	2.78
	0 M vs. 0.05 M	3.72	2.78
EC	0 M vs. 0.1 M	0.05	2.78
nanoparticle	0.01 M vs. 0.025M	0.79	2.78
concentration	0.01 M vs. 0.05M	0.48	2.78
0.5 g L^{-1}	0.01 M vs. 0.1M	2.61	2.78
	0.025 M vs. 0.05 M	1.29	2.78
	0.025 M vs. 0.1 M	1.83	2.78
	0.05 M vs. 0.1 M	3.18	2.78

Table B.4: ANOVA table of computed adsorption energy ($|\Delta E|$) at different ionic strength. The analysis is conducted at 95% confidence level for a 3×5 factorial design.

source	sum of square	degree of freedom	mean square	standard error	$t_{df(=30),0.025}$	LSD
EC nanoparticle concentration	1.09×10^9	2	5.47×10^8			
ionic strength	5.01×10^8	4	1.25×10^8			
interaction	1.15×10^9	8	1.44×10^8			
treatment	2.74×10^9	14	—			
error	1.44×10^9	30	4.78×10^7	6.92×10^3	2.04	1.41×10^4
total	4.18×10^9	44	9.50×10^7			

Table B.5: Statistics (mean and standard deviation) of the late-time DST slope $((d\gamma/dt^{-0.5})|_{t\to\infty})$ reported in Table 5.2. Reprinted with permission from [15], Copyright© 2015 American Chemical Society.

EC nanoparticle concentration [g L^{-1}]	ionic strength [M]	$(d\gamma/dt^{-0.5})|_{t\to\infty}$ [N m^{-1} s$^{0.5}$]	standard deviation	label
	0	0.2620	0.020494	1
	0.01	0.2459	0.027313	2
0.2	0.025	0.2382	0.051476	3
	0.05	0.3544	0.191579	4
	0.1	0.4568	0.067102	5
	0	0.093	0.01	I
	0.01	0.0971	0.012046	II
0.5	0.025	0.0883	0.015646	III
	0.05	0.125	0.067268	IV
	0.1	0.1424	0.017218	V
	0	0.0604	0.002718	i
	0.01	0.0560	0.008466	ii
0.8	0.025	0.0647	0.008562	iii
	0.05	0.0699	0.000636	iv

All possible comparisions are shown in the following figure. t_{obs} is calculated from $(|\bar{x}_1 - \bar{x}_2|)/\sqrt{(s_1^2/n_1 + s_2^2/n_2)}$, where $\bar{x}$, s, and n are the mean value, standard deviation, and the number of replicates, respectively and subscripts 1 and 2 show two different series. $T_{critical}$ is found from t-table at a 95% confidence level. The black, red, and blue bars should be compared to the $T_{critical}$ indicated by the black, red, and blue lines, respectively.
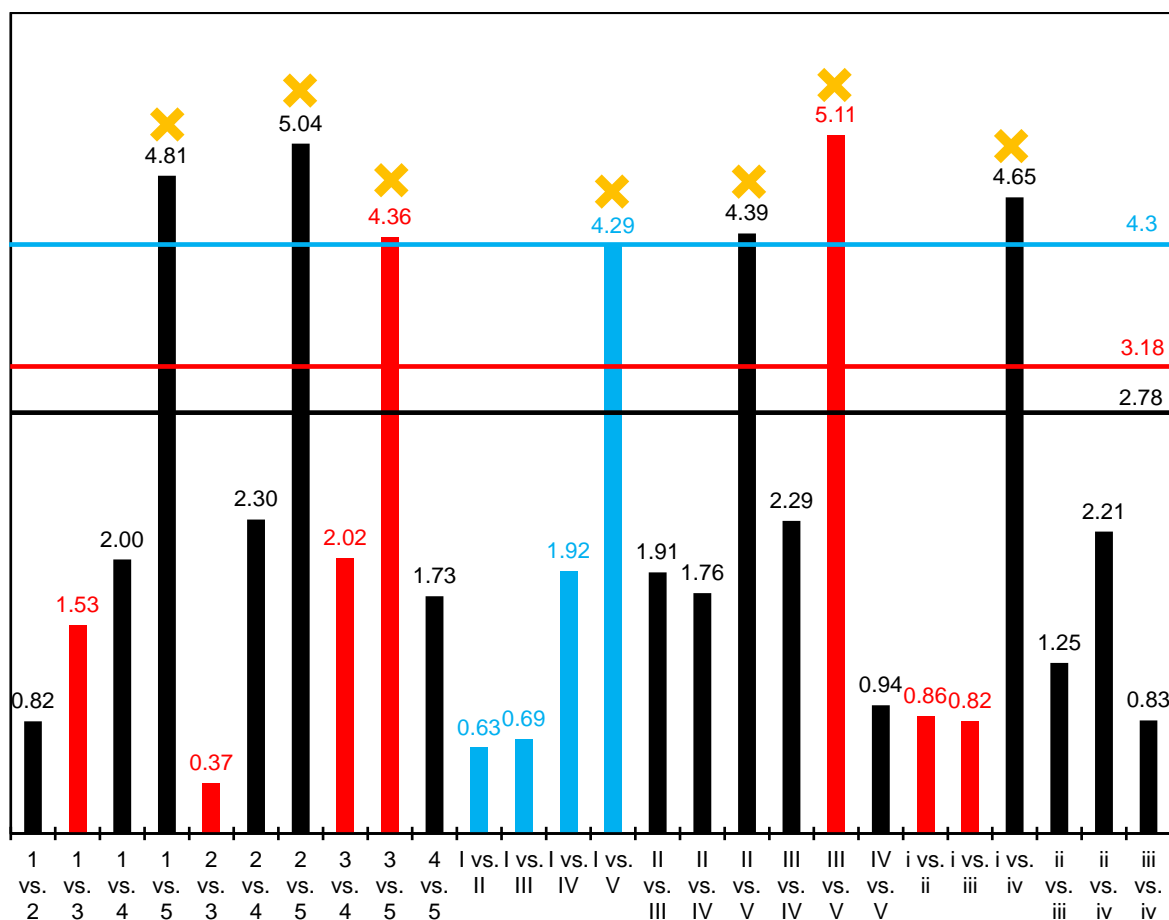

Figure B.1: Pair comparisions (t_{obs}) between $((d\gamma/dt^{-0.5})|_{t\rightarrow\infty})$ reported in Table 5.2. Reprinted with permission from [15], Copyright© 2015 American Chemical Society.

140

Appendix C

Parameter calculations

C.1 Capillary interaction consideration

Here, Bond number is calculated for a particle with a radius of r adsorbed at n-decane-water interface to find out the significance of capillary attractive force.

$$Bo = \frac{\Delta \rho g r^2}{\gamma} \tag{C.1}$$

where $\Delta \rho$ is the density difference between the sub-phase (water) and super-phase (n-decane), γ is the interfacial tension for pristine n-decane-water, and g is the nominal gravitational acceleration (i.e., 9.81 m s^{-2}). For n-decane-water system we have

$$Bo = \frac{(998 - 730)\text{kg/m}^3 \times 9.81\text{m/s}^2 \times (44.5 \times 10^{-9})^2\text{m}^2}{52 \times 10^{-3}\text{N/m}} = 10^{-10} \tag{C.2}$$

The calculated Bond number is small enough to neglect the effect of capillary attractive force between EC nanoparticles adsorbed at n-decane-water interface [112].

C.2 Coagulation rate vs. adsorption rate

Two dynamic processes are competing in the suspensions of EC nanoparticles of ionic strength at or beyond CCC: coagulation in the bulk and adsorption-driven interfacial assembly. It is shown [7, 69] that the initial coagulation rate is

$$\dot{R}_{coag}\big|_{t \to 0} = -k_{coag}^{fav} N_b^2 V \tag{C.3}$$

141

where k_{coag}^{fav} is the coagulation constant estimated from Smoluchowski rate constant (i.e., $k_{coag}^{fav} \cong k_s = 8k_B T/3\mu$, where μ is the viscosity of water) [7, 69], N_b is the EC nanoparticle concentration, and V is the bulk volume. The initial rate of adsorption at early-time is expressed as follows

$$\dot{R}_{ad}\big|_{t\to 0} = -k_a N_b^2 S \qquad (C.4)$$

where k_a is the adsorption constant and S is the area of fluid interface. For the pendant drop tensiometry experiments,V is the volume (10 μL) and S is the surface area of the pendant droplet, respectively. Assuming spherical droplets one obtains

$$\frac{\dot{R}_{coag}\big|_{t\to 0}}{\dot{R}_{ad}\big|_{t\to 0}} = \frac{k_{coag}^{fav} N_b R}{3k_a} \qquad (C.5)$$

where R is the radius of the pendant droplet. Considering the values reported in this study ($k_{coag}^{fav} \sim O(10^{-17})$m^3 s^{-1}, $k_a \sim O(10{-}1)$m s^{-1}, $N_b \sim O(10^{-17})$particle m^{-3}, and $R \sim O(10^{-3})$m), one obtains $\dot{R}_{coag}\big|_{t\to 0}/\dot{R}_{ad}\big|_{t\to 0} \cong O(10^3)$ for EC nanoparticle suspensions above the CCC. Although the rate of coagulation is initially $\sim$1000 times faster than the rate of adsorption, the bulk concentration changes only by $\sim$0.001% during the early stages (< 60 s) of the process. This supports the assumption that the bulk concentration remains constant during the early stages of adsorption regardless of EC nanoparticle concentration and ionic strength.

C.3 DLVO model parameters

Hamaker constant

Hamaker constant for two EC nanoparticles interacting in oil (H_{121}) is computed indirectly. In general, for two bodies (1 and 3) which interact in a medium (2), the following relationship for Hamaker constant (H_{123}) is written [80]

$$H_{123} = \left(\sqrt{H_{22}} - \sqrt{H_{11}}\right)\left(\sqrt{H_{22}} - \sqrt{H_{33}}\right) \qquad (C.6)$$

When the interacting bodies are similar, Eq. C.6 simplifies to $H_{121} = \left(\sqrt{H_{22}} - \sqrt{H_{11}}\right)^2$. In this work, H_{11} and H_{22} are the Hamaker constants for the interactions in vacuum for cellulose and n-decane, respectively, which are found to be 6×10^{-20} J [6] and estimated to be 4.6×10^{-20} J [80]. Therefore, H_{121} is found to be 10^{-20} J.

Debye length (κ^{-1})

The inverse Debye length (κ) is computed from the following equation for each ionic strength [45, 80]

$$\kappa = \sqrt{\frac{\sum_i (z_i e)^2 C_i^*}{\varepsilon_0 \varepsilon_w k_B T}} \tag{C.7}$$

where e is the elementary charge (1.602×10^{-19}C), z is the valance charge of ions (one for NaCl), and C_i^* is the number concentration of ions (in m^{-3}) which varies with ionic strength.

Particle surface charge density exposed to water (σ_{pw})

Particle surface charge density exposed to water, σ_{pw}, at a given particle surface charge (ζ-potential) is a function of inverse Debye length and ionic concentration as follows [71]

$$\sigma_{pw} = -\frac{4 e C_i^*}{\kappa} \sinh\left(\frac{e \Psi_{pw}}{2 k_B T}\right) \tag{C.8}$$

Surface dipole moment density (σ_d)

The last parameter listed in Table 5.4 is surface dipole moment density (σ_d) which is the effective parameter for dipole-dipole interactions through oil. σ_d is the product of surface density of polar groups at the particle-oil interface (σ) and average dipole moment of one polar group (p) [71]. By considering the molecular structure of EC (see Section 2.1.1), two polar groups (with the same fraction, 0.5) exposing to oil phase: hydroxyl and ethyl ether (diethyl ether). Therefore, a value of 4.6×10^{-30}Cm is calculated for p from [72]

$$p = \mu_{hydroxyl} \alpha_{hydroxyl} + \mu_{ethyl\ ether} \alpha_{ethyl\ ether} \tag{C.9}$$

where α is the fraction for each dipole and μ is the dipole moment which is 5.5×10^{-30}Cm and 3.7×10^{-30}Cm for hydroxyl and ethyl ether, respectively [1].
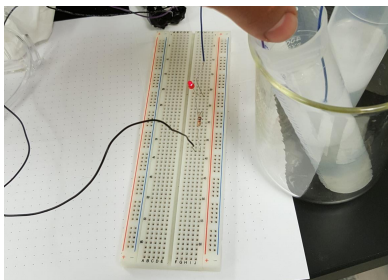
C.4 Pickering emulsion verification

Figure C.1: Conduction of electric current through the emulsion. An on LED lamp indicates the circuit to be closed, meaning that the generated emulsion at $f_{oil} = 0.33$ is oil-in-water.

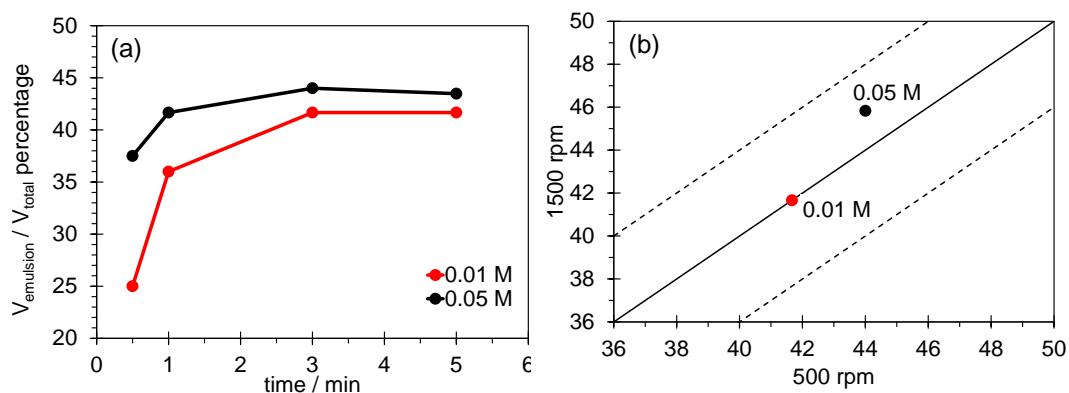## C.5 Optimum mixing conditions for Pickering emulsion generation

Figure C.2: (a) The effects of mixing time on the generated Pickering emulsion at 1 g L^{-1} EC nanoparticle concentration, two levels of ionic strength, $f = 0.33$, and mixing speed of 500 rpm. The emulsion volume percentage ($V_{oil}/V_{total} \times 100$) was recorded one day after the emulsion generated. (b) The effects of mixing speed volume percentage of Pickering emulsions generated at the conditions similar to (a) with a mixing time of 3 min.
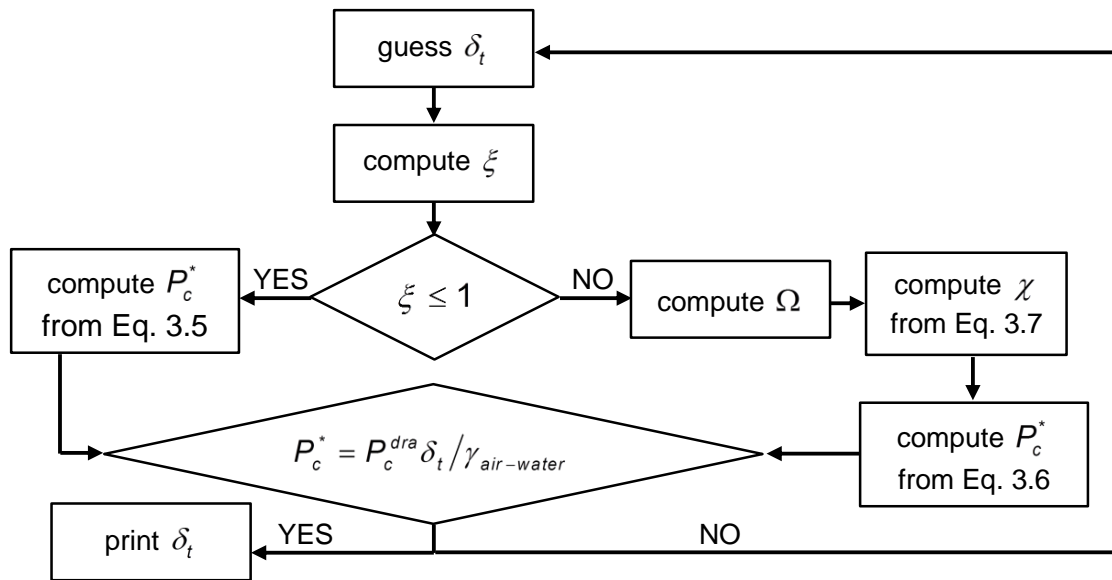
C.6 Micromodel parameters

Figure C.3: The flowchart to compute δ_t using Eqs. 3.5 to Eq. 3.7.

Appendix D

MATLAB Codes

D.1 PSD

The following code (written in MATLAB®) is taken from [140] to compute the pore size distribution (PSD) of a glass micromodel.

```
clc;
clear;
close all;

% INPUTS
A = imread('Input.png');
Resolution = 5;        %micron/pixel
Number_of_categories = 20;

% CALCULATIONS
A = im2bw(A, graythresh(A));
Conn = 8;
[s1, s2] = size(A);
A = bwmorph(A, 'majority', 10);
Poro = sum(sum(~ A))/(s1 * s2);
D = −bwdist(A, 'cityblock');
B = medfilt2(D, [33]);
B = watershed(B, Conn);
```

```
Pr = zeros(s1, s2);
for I = 1 : s1
for J = 1 : s2
if A(I, J) == 0&&B(I, J) ∼= 0
Pr(I, J) = 1;
end
end
end
Pr = bwareaopen(Pr, 9, Conn);
[Pr_L, Pr_n] = bwlabel(Pr, Conn);
V = zeros(Pr_n, 1);
for I = 1 : s1
for J = 1 : s2
if Pr_L(I, J) ∼= 0
V(Pr_L(I, J)) = V(Pr_L(I, J)) + 1;
end
end
end
R = Resolution. * (V./pi).^.5;        %Pore radius
```

%OUTPUTS
Average_pore_radius_micron=mean(R)
Standard_deviation_of_pore_radius_micron=std(R)
figure('units','normalized','outerposition',[0 0 1 1])
subplot(1,2,1)
imshow(label2rgb(Pr_L))
imwrite(label2rgb(Pr_L),'Output.png')
subplot(1,2,2)
Rel_Frequencies=hist(R,[1:round(max(R)/Number_of_categories):round(max(R))])...
./sum(sum(hist(R,[1:round(max(R)/Number_of_categories):round(max(R))])));
bar([1:round(max(R)/Number_of_categories):round(max(R))],Rel_Frequencies);
xlabel('Pore radius (micron)');
ylabel('Relative Frequency');
axis([1 max(R) 0 max(Rel_Frequencies)]);
axis square;
annotation('textbox',[.2 .85 .1 .1], 'String', ['Average pore radius=...
'num2str(Average_pore_radius_micron) 'micron'])

D.2 CDE

Eq. 7.3 is discretized (for N+1 nodes) as follows
for internal nodes: 2 to N

$$d\overline{N_b}(i) = \frac{\overline{N_b}(i+1) - 2\overline{N_b}(i) + \overline{N_b}(i-1)}{h^2} - Pe\frac{\overline{N_b}(i+1) - \overline{N_b}(i-1)}{2h} - Da_I\overline{N_b}(i)2.32\left(1 - \frac{\Theta(i)}{0.91}\right)^3;$$

(D.1)

for boundary nodes (boundary conditions): 0 and N+1
$$\overline{N_b}(0) = 1$$

$$d\overline{N_b}(N+1) = 2\frac{\overline{N_b}(N) - \overline{N_b}(N+1)}{h^2} - 2.32Da_I\overline{N_b}(N+1)\left(1 - \frac{\Theta(N+1)}{0.91}\right)^3$$

(D.2)

Eq. 7.4 is discretized as follows to be solved together with discretized CDE.

$$d\Theta(i) = 2.32\frac{k_i L^2 N_{b0}\pi r^2}{D_h}\overline{N_b}(i)\left(1 - \frac{\Theta(i)}{0.91}\right)^3;$$

(D.3)

The following function is written in MATLAB to solve Eqs.7.3 and 7.4 *via* a method of line approach.

$$function dydt = N_{MOL}(t, y, N)$$

% Defining the Parameters

$r = 44 * 10^{-9};$ %nanoparticle size, m
$Dh = 3.36 * 10^{-7};$ % m^2/s
$L = 30.7 * 10^{-2};$ % m
$vp = 1.48 * 10^{-4};$ % m/s
$ki = 5 * 10^{-6};$ % m/s
$Nb0 = 2.5 * 10^{18};$ %initial concentration, particle/m^3
$Sw = 0.5;$ %water saturation
$c1 = 8600;$ %1/m
$c2 = 1.5;$
$a0 = c1 * (1 - Sw)^{c2};$ %1/m

$Pe = vp * L/Dh$;
$DaI = ki * L^2 * a0/Dh$;

$dydt = ones(2 * N + 2, 1)$;
$Nb(1, 1) = 1$; %BC of Nb
$y(1, 1) = 1$;

$h = 1/N$;

$Nb(1 : N + 1, 1) = y(1 : N + 1, 1)$;
$theta(1 : N + 1, 1) = y(N + 2 : 2 * N + 2, 1)$;

for i=2:N
$dNb(i, 1) = (Nb(i + 1) - 2 * Nb(i) + Nb(i - 1))/h^2 - Pe * (Nb(i + 1) - Nb(i - 1))/(2 * h) - DaI * Nb(i) * 2.32 * (1 - theta(i)/0.91)^3$;
$dtheta(i, 1) = ki * L^2 * Nb0 * pi * r^2 * Nb(i) * 2.32 * (1 - theta(i)/0.91)^3/Dh$;
end

$dNb(N+1, 1) = 2*(Nb(N) - Nb(N+1))/h^2 - DaI * Nb(N+1) * 2.32 * (1 - theta(N+1)/0.91)^3$;
%BC
$dtheta(N + 1, 1) = ki * L^2 * Nb0 * pi * r^2 * Nb(N + 1) * 2.32 * (1 - theta(N + 1)/0.91)^3/Dh$;

$dydt(1 : 2 * N + 2, 1) = [dNb; dtheta]$;

To solve the function, the ODE45 is used as follows

clear
clc

format long

$Dh = 3.36 * 10^{-7}$;   % m^2/s
$L = 30.7 * 10^{-2}$;   % m
$vp = 1.48 * 10^{-4}$;   % m/s

$tspan = [0.02]$;
$N = 150$;
$y0(1 : N + 1) = zeros(N + 1, 1)$; % Nb at initial condition

$y0(N + 2 : 2 * N + 2) = zeros(N + 1, 1); \%$ theta at initial condition

$[t, y] = ode45(@(t, y)N_{MOL}(t, y, N), tspan, y0);$
$PV = vp * t * L/Dh;$

figure(1)
hold on
$Nbj = y(:, N + 1);$
$plot(PV, Nbj,' b')$